UNIVERSITY OF BRISTOL

DOCTORAL THESIS

Tritium Storage & Processing for Fusion Energy

Author:
Gareth GRIFFITHS

Supervisor:
Dr. Ross SPRINGELL
Rachel LAWLESS, UKAEA

A thesis submitted in fulfilment of the requirements
for the degree of Doctor of Philosophy in the
Interface Analysis Centre, School of Physics

based upon research performed in conjunction with


UK Atomic Energy Authority

November 1, 2023

Declaration of Authorship

I, Gareth GRIFFITHS, declare that this thesis titled, "Tritium Storage & Processing for Fusion Energy" and the work presented in it are my own. I confirm that:

- This work was done wholly or mainly while in candidature for a research degree at this University.
- Where any part of this thesis has previously been submitted for a degree or any other qualification at this University or any other institution, this has been clearly stated.
- Where I have consulted the published work of others, this is always clearly attributed.
- Where I have quoted from the work of others, the source is always given. With the exception of such quotations, this thesis is entirely my own work.
- I have acknowledged all main sources of help.
- Where the thesis is based on work done by myself jointly with others, I have made clear exactly what was done by others and what I have contributed myself.

Signed: _____

Date: November 1, 2023

Covid-19 Statement

The Covid-19 pandemic, and its associated lockdowns, have had a significant impact on the amount of lab-based research that could be performed during this work.

On 23rd March 2020 The UK went into the first nationwide lockdown and the University of Bristol Physics dept. was closed down. I was first granted reinstated lab access on 21st January 2021. These 10 months of not being able to access the labs were followed by many more months of limited and restricted access, both during and outside of the further two subsequent lockdowns.

The period of prohibited lab access, followed by a period of limited lab access, are not the full extent of the impact that the covid-19 pandemic had on the ability to conduct lab-based research during this work. Outside of the time periods of the three national lockdowns progress was inhibited by multiple periods of (covid related) illness and self-isolation by me and also other people whose role it is to facilitate research (i.e. supervisors, lab technicians, academics, administrative & managerial staff etc.).

The long periods of lying dormant and unused, and in some cases switched off, seemed to have a detrimental effect on some of the technical equipment and machinery in the labs, there were many instances of equipment breaking down or not working properly during this period.

UNIVERSITY OF BRISTOL

Abstract

Faculty of Science

School of Physics

Doctor of Philosophy

Tritium Storage & Processing for Fusion Energy

by Gareth GRIFFITHS

The aim of this thesis, and the research conducted in support of it, is to investigate and optimise current methods used in fusion energy to store and separate tritium: uranium hydride and palladium hydride, respectively.

Results of an investigation of powderising uranium metal using hydride formation-decomposition cycles are presented. The new insights gained from this were: the uranium metal reached its maximum powderisation on the 4th cycle; and that the bulk of the powderisation happened during the first cycle.

An investigation into performing a heat treatment regime on depleted uranium was conducted. The investigation found that the heat treatment regime bought about a shortening of the bulk reaction stage of the UH_3 reaction, and the formation of a new compound (a monoxide phase), but only when carbon was present in the system.

The optimum H_2 gas pressure for forming palladium hydride at room temperature was found to be in the range P = 1200 - 1500 mbar; and the fastest H_2 desorption rate, of the temperature range investigated, was observed at 250°C.

Acknowledgements

I would like to acknowledge and thank the following people for their help, guidance, advice, tolerance and friendship during this work:

Dr. Ross Springell and **Professor Tom Scott** as my supervisors at the Interface Analysis Centre, University of Bristol;

Rachel Lawless as my supervisor at Culham Centre for Fusion Energy;

My B22 comrades, **Dr. Haris Paraskevoulakos** and **Dr. Antonios Banos** for their input during corrosion experiments (and all the long conversations that made being trapped in a radioactive dungeon for years more tolerable);

Dr. Chris Jones for help with x-ray tomography;

Dr. Jacek Wasik, **Dr. Lottie Harding** and **Dr. Jarrod Lewis** for help with x-ray diffraction;

Dr. James Hargreaves for help with technical drawing and design;

My oldest friends in the world **Matthew Ault**, for help with writing computer code, & **Daniel Ruth**, for help with viva preparation and final read-through of this thesis;

Dr. Keith Hallam for helping me with proper use of commas and degree symbols;

Dr. Macarena Leal Olloqui and **Dr. Witek Szeremeta** for moral support and for listening to me complain;

James O'Neil and **Dr. Graham Hawkes** for giving me the time and space to write this thesis;

All of the friends I made along the way for making it such an enriching experience;

Finally, and most importantly, **Jenny Drake** for being endlessly encouraging, supportive and tolerant during this time and for continuously giving me a reason and motivation to keep going with it.

Contents

List of Figures

List of Tables

List of Abbreviations

CCFE	**C**ulham **C**entre for **F**usion **E**nergy
JET	**J**oint **E**uropean **T**orus
ITER	**I**nternational **T**hermonuclear **E**xperimental **R**eactor
FCC	**F**ace **C**entred **C**ubic
BCC	**B**ody **C**entred **C**ubic
HCP	**H**exagonal **C**lose **P**acked
QCD	**Q**uantum **C**hromo**D**ynamics
RGA	**R**esidual **G**as **A**nalyser
SPL	**S**urface **P**assivation **L**ayer
XRD	**X**-**R**ay **D**iffraction
XRT	**X**- **R**ay **T**omography
XRF	**X**- **R**ay **F**luorescence
TGA	**T**hermo **G**ravimetric **A**nalysis
FWHM	**F**ull **W**idth **H**alf **M**aximum
TCAP	**T**hermal **C**ycling **A**bsorption **P**rocess
PFR	**P**lug **F**low **R**everser
SRNL	**S**avannah **R**iver **N**ational **L**aboratory
MCF	**M**agnetic **C**onfinement **F**usion
ICF	**I**nertial **C**onfinement **F**usion
UKAEA	**UK A**tomic **E**nergy **A**uthority

Physical Constants

Speed of Light	$c = 2.997\,924\,58 \times 10^{8}\,\mathrm{m\,s^{-1}}$
Plank's Constant	$h = 6.626\,070\,040 \times 10^{-34}\,\mathrm{J\,s}$
Coulomb's constant	$k = 8.987\,55 \times 10^{9}\,\frac{\mathrm{Jm}}{\mathrm{C^2}}$
	$k = 5.6096 \times 10^{28}\,\frac{\mathrm{eVm}}{\mathrm{C}}$
Fine-Structure Constant	$\alpha = 7.297\,352\,566\,4 \times 10^{-3}$
Rydberg Constant	$R_\infty = 10\,973\,731.568\,508\,\mathrm{m^{-1}}$
Bohr Radius	$a_0 = 0.529\,177\,210\,67 \times 10^{-10}\,\mathrm{m}$
Thomson Cross Section	$\sigma_0 = 0.665\,245\,871\,58 \times 10^{-28}\,\mathrm{m^2}$
Electron Volt	$eV = 1.602\,176\,620\,898 \times 10^{-19}\,\mathrm{J}$
Mass of Proton	$m_p = 1.672\,621\,898 \times 10^{-27}\,\mathrm{kg}$
Mass of Neutron	$m_n = 1.674\,927\,471 \times 10^{-27}\,\mathrm{kg}$
Mass of Electron	$m_e = 9.109\,383\,56 \times 10^{-31}\,\mathrm{kg}$
Atomic Mass Unit	$amu = 931.494\,MeV$

All values taken from Physical Measurement Laboratory

List of Symbols

r	radius	m
m	mass	kg
Z	proton number	dimensionless
A	nucleon number	dimensionless
U	potential energy	J
g	coupling constant	dimensionless
μ	mass of pion	kg
Q	enthalpy of reaction	J
a, b, c	lattice constants	$\cdot 10^{-12}$ m
P	pressure	mbar
T	temperature	°C
t	time	s
θ	angle	°
λ	wavelength	$\cdot 10^{-9}$ m = nm
		$\cdot 10^{-10}$ m = Å

This PhD Thesis is dedicated to my Mum. Someone who has worked, fought, and sacrificed much more than I ever could to get me here. The strongest and most diligent person I have ever known. An absolute model of resilience and strength in the face of adversity.

Mum, I couldn't have got here without you. Thank you for everything you have done for me and sacrificed for me
...and for all of us.

Chapter 1

Introduction

1.1 Hydrogen Isotope Storage for Fusion Energy

Because of its high capacity for accommodating and holding hydrogen isotopes in its lattice structure, depleted uranium has become the preferred choice of the fusion industry for storing tritium. Depleted uranium (DU) stores tritium in the form of uranium tritide: $[^{238}U][^{3}H]_3$.

1.1.1 Uranium Use at UKAEA

UKAEA has been using hydrogen isotopes in tokamak reactors since the start of operations of the Joint European Torus (JET) in 1983 [1] at the Culham Centre for Fusion Energy (CCFE), which went on to become the first facility in the world to achieve successful use of tritium in a tokamak in 1991 [1]. The method of storing these hydrogen isotopes used at CCFE (since 1995 [2]) is in the form of a metal-hydride on storage beds of depleted uranium. Almost 30 years of storing hydrogen isotopes, as well as numerous research collaborations with various academic institutions, has equipped UKAEA with an expertise in DU bed storage and an extensive track record of peer-reviewed international level journal publications on the subject [3]. The technologies and capabilities of UKAEA in this subject area are some of the most mature and well developed in the world.

1.1.2 Metal Hydrides as a Hydrogen Storage Method

Storing hydrogen as a metal hydride is a form of solid-state storage. Metal-hydrides are formed when a metal is exposed to gaseous hydrogen under particular temperature and pressure conditions (differing depending on the metal). When a metal (M) is exposed to hydrogen (H) then the hydrogen permeates through the lattice structure of the metal and, given the required temperature and pressure conditions for that particular metal are achieved, the hydrogen chemically bonds with the metal:

$$M + \frac{x}{2}H_2 \rightleftharpoons MH_x \tag{1.1}$$

(where x = number of hydrogen atoms per metal atom)

This forms a dense, stable metallic structure, holding the hydrogen inside the metal. The process can be reversed by heating to (or above) the required temperature to decompose the metal-hydride (again, dependant on the metal being used).

As can be seen from figure 1.1, in general metal-hydrides as a hydrogen storage method came out as some of the lowest energy storage cost (kWh/kg H_2) when compared to some other storage methods. Magnesium hydride (MgH_2) requires 0.7 kWh/kg H_2, intermetallic hydrides require 0.8 kWh/kg H_2, lithium-boron-magnesium alloy hydride ($LiBH_4 - MgH_2$) requires 0.8 kWh/kg H_2, lithium-nitrogen-magnesium requires 0.9 kWh/kg H_2. Aluminium hydride as a hydrogen storage method is not so energy efficient, but aluminium is a well-documented outlier when it comes to metal-hydrides. Its bonding is very weak and its reaction kinetics are known to be very slow. The liquid organic hydrogen carriers (LOHCs) also came out very well - 0.7 kWh/kg H_2, the same as MgH_2. Unfortunately the data for UH_3 energy storage cost wasn't included [4].

	Storage process				Release process	
Storage technology	Heat (kWh/kg H_2)	Temperature (°C)	Pressure (bar)	Electricity (kWh/kg H_2)	Heat (kWh/kg H_2)	Temperature (°C)
Gas 100 bar	-	-	100	1[a]	-	-
Gas 200 bar	-	-	200	1.2[a]	-	-
Gas 700 bar	-	-	700	1.6[a]	-	-
Liquid hydrogen	-	−253	-	6	-	-
Adsorption	-	−176	40	6.7	-	-
AlH_3	54	<70	-	10	1	100
MgH_2	-	300	30	0.7[a]	10.3	350
Intermetallic hydride[d]	-	<80	50	0.8[a]	≈2-6	<80
$NaAlH_4$	-	125	100	1[a]	5.7	160
$LiBH_4$–MgH_2	-	350	50	0.8[a]	6.4	350
2 $Li(NH_2)$–MgH_2	-	150	70	0.9[a]	5.6	150
Methanol	-	250	50	1.3–1.8	6.7	250[c]
Ammonia	-	400	250	2–4	4.2	>425
Formic Acid	64	100–180	105	6.7	4.3	<100
MCH-TOL	-	150	30	0.7	11.2	350[b]
DBT-PDBT	-	150	30	0.7	9	300
NEC-DNEC	-	150	30	0.7	7.6	220

[a] Estimated as the work of compressing hydrogen to the hydrogenation pressure with an isothermal efficiency of 0.7 [15].
[b] Approximately 13% of heat can be supplied at a temperature of around 101 °C, the rest at 350 °C.
[c] Approximately 66% of heat can be supplied at a temperature of around 100 °C, the rest at 250 °C.
[d] Generic intermetallic hydride (low-temperature heat may be used).

FIGURE 1.1: Operating costs in terms of heat (amount and temperature) and electricity for considered hydrogen storage technologies. If the process is thermoneutral or exothermal, no value for the required heat is specified in the table. MCH-TOL = methylcyclohexane and toluene, DBT-PDBT = dibenzyltoluene and perhydro-dibenzyltoluene, NEC-DNEC = N-ethylcarbazole and dodecahydro-N-ethylcarbazole (all Liquid Organic Hydrogen Carriers – LOHCs). Figure and caption taken from [4]

1.1.3 Depleted Uranium (DU) Bed Hydrogen Storage

Depleted uranium is a good choice of material for storing hydrogen isotopes in the form of a metal-hydride because it is relatively easy to form and decompose the hydride phase; it forms a very stable hydride; has good reversibility; and, the reaction and its kinetics are very well understood [5]. Depleted uranium will react with gaseous hydrogen, to form UH_3, at temperatures between 200 - 350°C when dealing with a bulk metal sample (as in this work). If the formation and decomposition of a hydride is repeated (cycled) then the atomic hydrogen will destabilise the lattice structure of the depleted uranium, causing it to crumble into a fine powder. After 4 - 6 (see § 5.1) formation & decomposition cycles the metal will be as fine as possible, increasing the surface area and exposing an increased number of low energy

sites for the hydrogen gas to permeate into the metal and lowering the activation energy of the reaction [5]. This increases the speed of the reaction kinetics and means that the formation reaction of UH_3 can be achieved at room temperature. This not only lowers the amount of energy required to store hydrogen on DU but also provides a convenient safety backstop in the event of a loss-of-power incident.

The gravimetric hydrogen capacity of depleted uranium - the amount of H_2 absorbed per unit mass - isn't very high when compared to some metals (a theoretical maximum of 0.0126 $kgH_2 \cdot kg^{-1}$ or 1.26 wt.% [6], for comparison to other materials see figures 1.2 & 1.3), but this is because of the very large size and weight of the ^{238}U atom. UH_3 offers a very high volumetric H_2 density of 140 $kg \cdot m^{-3}$ (theoretical maximum value) double that of liquid hydrogen, which is 70.85 $kg \cdot m^{-3}$ [7] and 20 times that of compressed hydrogen at 100 bar, which is 7 $kg \cdot m^{-3}$ [7]. For further comparison to other methods and materials used for hydrogen storage see figure 1.2.

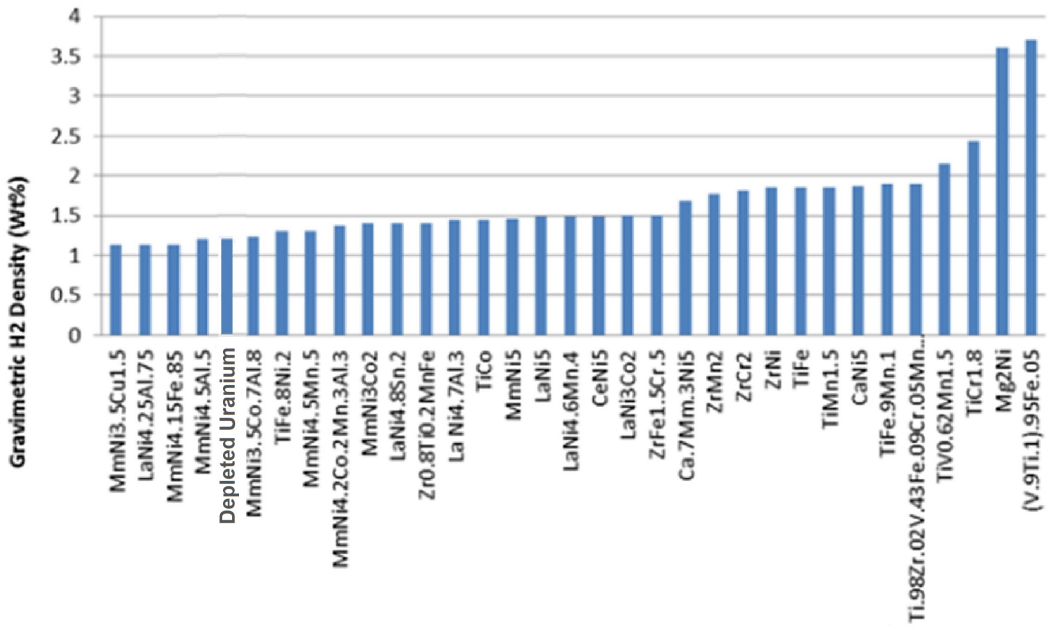

FIGURE 1.2: Metal hydrides versus hydrogen capacity. Figure taken from [8] and adapted.

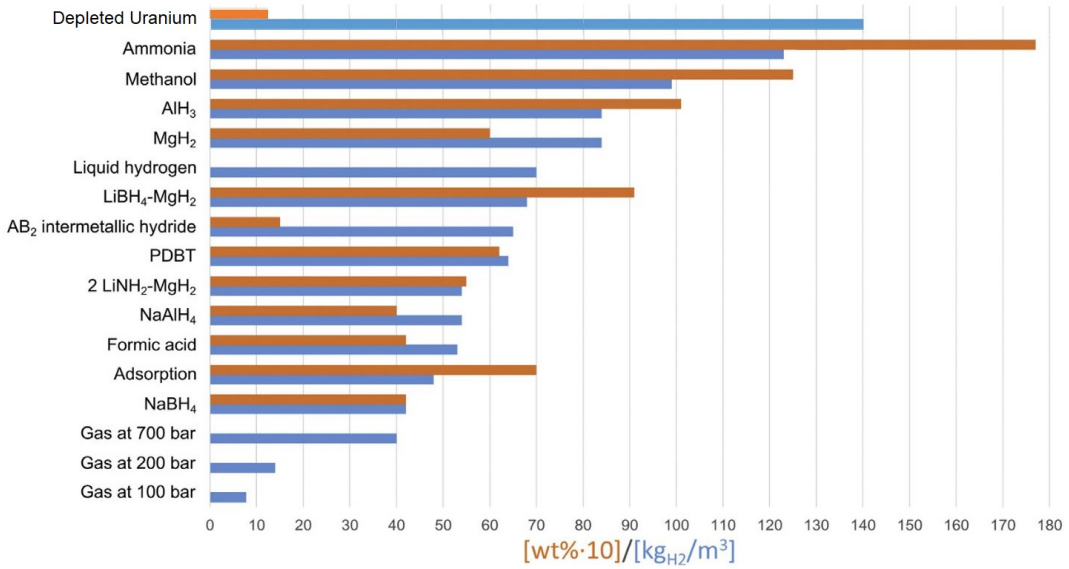

FIGURE 1.3: Volumetric ($kg \cdot m^{-3}$ in blue) and gravimetric (wt% multiplied by ten in orange) hydrogen storage densities of considered technologies. For the metal hydrides, the values in the graph indicate volumetric and gravimetric hydrogen storage densities that have been achieved in practice. The AB2 intermetallic hydride is Hydralloy C52 compacted with ENG. For NaBH4 a 20% solution in 10% NaOH is assumed. Adsorption refers to values by Mokaya et al. (2017) for cellulose acetate-derived activated carbons at 30 bar and 196°C. Figure and caption taken from [4] and adapted.

According to the Office of Nuclear Regulation (ONR) the 2020 annual figure for holdings of civil depleted, natural and low enriched uranium in the UK nuclear fuel cycle was 1.2 million tonnes [9]. This amount of uranium would be theoretically capable of storing 8,832 tonnes of hydrogen (this value pertains to protium, ^1H, for tritium it would be triple this value). Hydrogen (when used as a source of energy for power generation) can generate 40,000 kWh per tonne [10] so this amount of uranium could store 0.35TWh of energy. The UK total energy consumption in the previous year (2019) was 11.63TWh [11]. The UKs store of uranium in 2020 could have stored enough hydrogen to account for 3.01% of the previous years total UK energy consumption.

1.2 Hydrogen Isotope Separation in Fusion Energy

Because of its tendency to preferentially absorb the lighter hydrogen isotopes, combined with its low activation energy and its high capacity for accommodating and holding hydrogen isotopes in its lattice structure, palladium has generally become the preferred choice for separating hydrogen isotopes by exploiting the above characteristics of palladium and its hydride: $Pd[^{1/2/3}H]_x$.

The hydrogen absorption characteristics of palladium are often exploited to separate isotopes by inducing a temperature swing adsorption or a pressure swing adsorption. A technique that involves both of these (temperature as a driver and pressure as a useful consequence) is currently under consideration for use at UKAEA: *Thermal Cycling Absorption Process* (TCAP).

1.2.1 Thermal Cycling Absorption Process

Basic Principles of TCAP

TCAP separates gaseous hydrogen isotopes and is a semi-continuous method based on palladium gas chromatography. TCAP was first developed at Savannah River National Laboratory in 1980 [12], a working TCAP unit was assembled soon after. Since then, the evolution of TCAP has been continued by SRNL and others. The central principle of TCAP is to exploit the characteristics of palladium and how it interacts with hydrogen gas at different temperatures (see § 3.2). In general, the TCAP unit consists of a central column packed with palladium and a second column that provides a volume to be filled with gas while the palladium regenerates (see figure 1.4).

Column 1 is packed with palladium on a substrate material, usually kieselguhr (a soft, diatomaceous rock, comprised mostly of silicon dioxide, crumbled into a fine powder) but aluminium oxide (Al_2O_3) has also been used

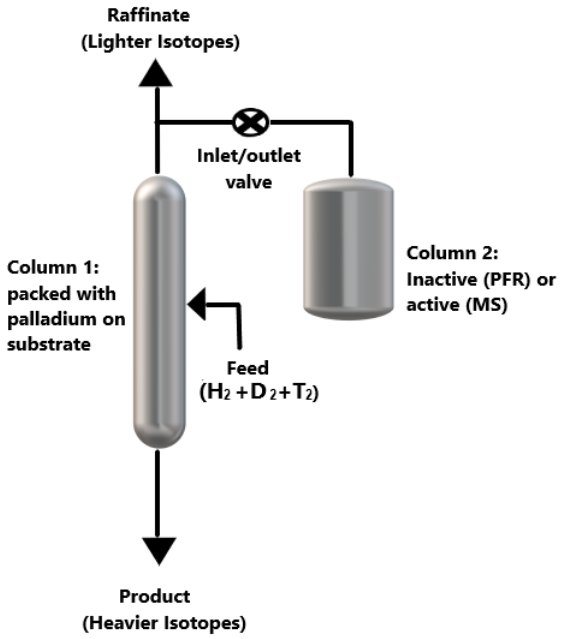

FIGURE 1.4: Simplified schematic of the basic design of the two TCAP columns.

in some designs. Kieselguhr helps to reduce the pressure drop along the column and provides a large surface area of palladium metal to get a faster isotope exchange reaction [13]. Column 2 was originally used as an inactive volume packed with kieselguhr whose purpose was to accommodate the unabsorbed portion of the feed gas without too much mixing. This is called a *plug flow reverser* (PFR), but in later designs it was packed with MS4A (a molecular sieve material) to provide further separation of hydrogen isotopes referred to as an inverse column [14]. Making the PFR (column 2) shorter and wider than column 1 and packing it with kieselguhr has the effect of allowing gas to flow between the two columns whilst minimising the mixing of the two volumes of gas (by minimising density variation along the length of the column and minimising radial variations in the velocity and concentration of the gas, making turbulent gas transport that will disturb the axial purity less likely - see the plug-flow reactor model [15]), thus maintaining the isotopic concentration profile created by column 1 [16].

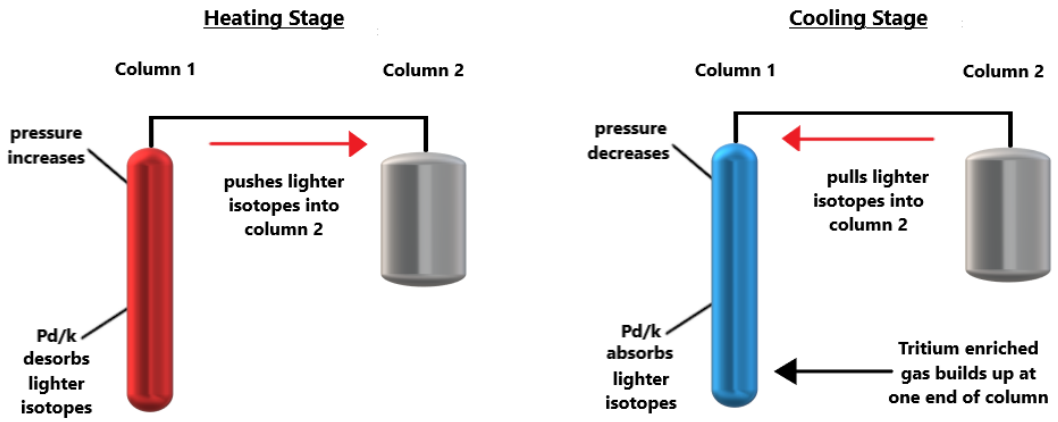

FIGURE 1.5: Heating and cooling stages of the TCAP process. The wording "lighter isotopes" is used for simplification. In reality it is a gaseous mixture of all isotopes, with the lighter isotopes being the largest component that becomes progressively more depleted in heavier isotopes as the process progresses.

The Cycling Process

During the TCAP process, column 1 is thermally cycled by a heating and cooling system. When the palladium in column 1 is heated it will desorb gas, thus creating a higher pressure that will push the gas into column 2. When it is cooled it will absorb gas, creating a lower pressure that is able to pull gas out of column 2 (see Figure 1.5). This creates temperature and pressure swings which are the driving forces of the TCAP process [16].

During the cooling stage, the palladium will absorb the hydrogen isotopes flowing into column 1 from column 2. As the gas flows through the column, isotopic exchange occurs between the gas and the solid (Pd) phases [17]. The lighter isotopes will be absorbed preferentially. This means the heavier isotopes travel faster than the lighter ones. As a result, a concentration profile develops along the length of column 1, with the heavy isotope concentrated at the product end, and lighter isotopes remaining at the raffinate end (as shown in figure 1.5) [12]. During the heating stage, the gas is desorbed from the Pd and flows from column 1 into column 2. Again, due to preferential isotopic absorption, the heavier isotopes travel faster than the

lighter isotopes which partially negates the separation gained in the cooling stage. However, the heating stage does not completely negate the separation gained in the cooling stage since the preferential absorption of lighter isotopes by Pd is significantly reduced at high temperatures. As a result, the concentration profile is reduced somewhat but is still present at the end of the heating stage. Therefore, a net gain in separation is achieved after each full cycle [12]. After a number of cycles, quite a significant isotope separation boundary is created. The product and raffinate can then be extracted from either end of column 1 (as shown in figure 1.4) and more feed gas can be inserted (into the middle of column 1). In order to maintain semi-continuous operation, only a small amount of the column inventory should be withdrawn from the two ends of column 1 at the beginning of each heating stage. An equal amount of feed gas should then be inserted into the middle of column 1 at the beginning of each cooling stage to keep the column inventory constant [18]. The low flow rate required in the cooling stage (to maintain good separation whilst also avoiding axial mixing) was found to be the rate-limiting step in the TCAP process [19].

Advantages of Using TCAP

The main advantages of using TCAP over other hydrogen isotope separation methods are:

1. It is a semicontinuous rather than a batch process - which results in much higher production rates and overall separation factors;

2. Its compact size – all TCAP units have (at the time of writing) been small enough to fit inside a glove box, which makes confinement of radioactive substances easier;

3. Its separative capacity – a TCAP unit roughly the size of a large suitcase has the separative capacity comparable to a two-story cryogenic distillation column or ten two-story thermal diffusion columns [18].

Current Challenges Around TCAP

One of the biggest challenges, currently, is around the scaling-up of the TCAP unit. In 2004 SRNL attempted to design and build a scaled-up version of their TCAP design for separating protium-tritium mixtures and was named HT-TCAP. They were unsuccessful in their attempt due to significantly reduced separating capability [20, 21]. The reasons for this were not known until recently (Xiao et. al, 2019 [22]). The issue is likely to be the increase in radius of a separating column of coiled geometry. When testing their new design, HT-TCAP, SRNL found that the increase in the column diameter of the coiled column decreased its separating ability by a factor of 2.5, which they confirmed was in accordance with the Giddings model [22] (A model derived by J. Calvin Giddings, showing that increasing the radius of a separating column of coiled geometry has a detrimental effect on its separating ability [23]).

1.3 Project Aim & Scope

The recent growth of the fusion industry, in both the public and private sectors, has meant that a number of new reactors are being designed (and in some cases are already in the process of being constructed). Some of these new reactors (such as ITER) will be much larger than previous reactors, and some will be updated iterations of the current reactors (such as STEP and DEMO). These new designs will require the tritium storage and handling systems to be as efficient and reliable as possible

For the reasons explained above uranium is the chosen method for storing hydrogen isotopes in the fusion industry. Much work has been done on optimising materials for solid-state hydrogen storage in the past [24]. This mostly tends to be focused on hydrogen storage for the transportation sector: hydrogen-powered cars, lorries, planes; transporting hydrogen to refuelling stations; movable means of supplying power to temporary sites (shipping crate style power plants) [25–27]. These sectors have very different criteria for optimising a hydrogen storage material than the fusion industry. Depleted uranium is often precluded from the investigations firstly because of its weight (the low gravimetric density of UH_3, described above in § 1.1.3 and figures 1.2 & 1.3) but also because of safety and regulatory considerations due to uranium being a controlled, radioactive substance.

The aim of this work is (in part) to perform an investigation into the optimisation of the approach of using uranium as a solid-state hydrogen storage material for the fusion industry. And to gain a full understanding of any optimisation techniques that arise from the investigation.

Another aim of this work is to gain an understanding (through experimentation, not just relying on preexisting literature) of the palladium-hydrogen system, at various temperatures and pressures, so as to best utilise the temperature and pressure swing absorption methods described above.

Chapter 2

Theory

2.1 Fusion Energy

Nuclear fusion is the process of fusing two atoms together into a single atom, usually, of a different element. The most favourable reaction for generating energy from the nuclear fusion process uses deuterium and tritium (known as a *D-T reaction* - see figure 2.1), this is the combination of isotopes with the highest probability of undergoing a fusion reaction due to the large reaction cross-section between them; and the combination that gives back the largest energetic return on the energy invested in the reaction [28]. Equation 2.1 shows the energy produced by the D-T fusion reaction [29].

$$ {}^{2}_{1}H \; + \; {}^{3}_{1}H \; \rightarrow \; {}^{4}_{2}He \; [3.56\, MeV] + \; {}^{1}_{0}n \; [14.03\, MeV] \tag{2.1} $$

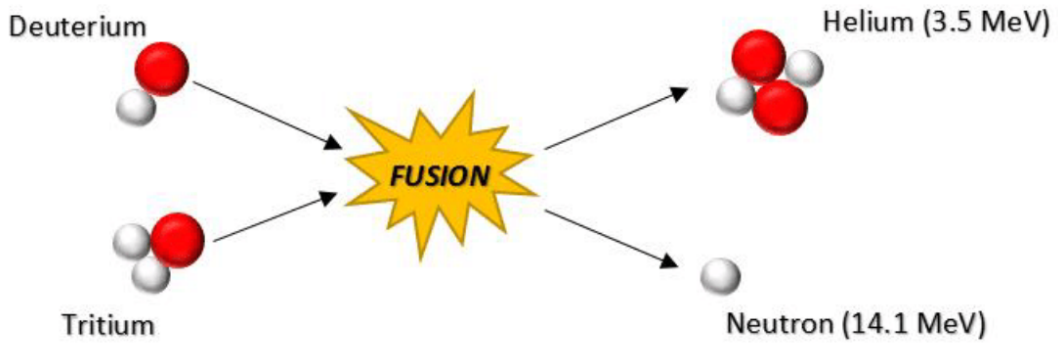

FIGURE 2.1: Illustration of the D-T fusion reaction.
Image taken from [30].

There are two main approaches to generating power by fusion currently being used: *Magnetic Confinement Fusion* and *Inertial Confinement Fusion*.

2.1.1 The Coulomb Barrier

In order for the D-T fusion reaction to occur the two nuclei need to be forced close enough together that the attraction of the strong nuclear force can pull them together. Because both of the reactants are partly made of protons, Coulomb repulsion exerts a force on the two nuclei. The Coulomb force is greater in range than the strong nuclear force [31] so the nuclei must be energetic enough to overcome the repulsion of the Coulomb force to get within the short range of the strong force (≈ 1.3 fm [32]). A potential barrier is formed which must be overcome, this is known as *the Coulomb barrier*. The height of the Coulomb barrier is equivalent to the energy that is needed to bring the nuclei in close enough proximity to each other. Coulomb barrier height is given, in MeV, by equation 2.2 [33], where k is Coulomb's constant (in MeV $\cdot$ fm), A_i and Z_i are the nucleon number and proton number of nucleus i, respectively, and R_i is position of nucleus i (in fm).

$$U_{Coulomb} = \frac{k\, Z_1\, Z_2\, e^2}{R_1 + R_2} = \frac{1.44\, Z_1\, Z_2}{1.2\,(A_1^{1/3} + A_2^{1/3})} \tag{2.2}$$

For the example of the D-T reaction (where A_1=2, Z_1=1, A_2=3, Z_2=1), equation 2.2 gives:

$$U_{D-T} = \frac{1.44 \cdot 1 \cdot 1}{1.2(2^{1/3} + 3^{1/3})} = 0.44\dot{4}\, MeV \tag{2.3}$$

this gives the energy required to bring the nuclei within such a radius that the strong force can overpower the electric repulsion.

2.1.2 Quantum Tunnelling

The description in §2.1.1 might seem to suggest that the temperature required to initiate a D-T fusion reaction (the *critical ignition temperature*) can be found by equating the Coulomb barrier height with the average thermal energy of the nuclei:

$$E_{Thermal} = \frac{3}{2}kT \tag{2.4}$$

This is, in fact, not the case. The nuclei actually penetrate the barrier and come within close enough proximity for fusion to occur by a process of *quantum tunnelling* (each nuclei's wavefunction, that represents the probability of finding a nuclei at a given location, extends to the other side of the Coulomb barrier). This means that a lower temperature is required for a fusion reaction to take place than the temperature given by equating equations 2.2 & 2.4.

2.2 Tritium

Tritium is the heaviest natural isotope of the lightest element, hydrogen (see figure 2.2). Hydrogen ($^1_1$H) is comprised of one proton and a single electron in its 1s shell. Tritium ($^3_1$H or T) is the third isotope of hydrogen. It is the only naturally occurring radioisotope of hydrogen. The tritium nucleus consists of one proton and two neutrons. Hydrogen has a lower isotope, deuterium ($^2_1$H or just D), with one proton and just one neutron. Due to having the same number of protons, tritium's nucleus has the same electric charge as the protium ($^1_1$H) nucleus, and so the neutral atom contains the same number of electrons. Tritium has roughly three times the atomic weight of protium (due to the two extra nucleons).

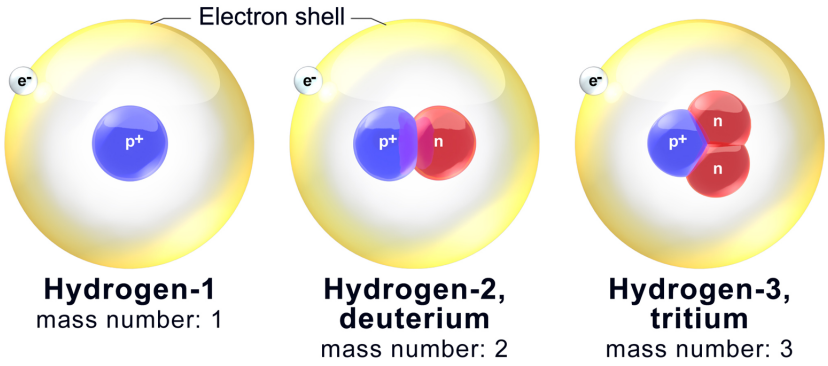

FIGURE 2.2: Three Isotopes of Hydrogen (artist's impression). Image adapted from Wikimedia Commons. Created by BruceBlaus, under the Creative Commons Attribution 3.0 Unported license.

2.2.1 Production

Naturally occurring tritium is produced by reactions between cosmic ray protons and neutrons with atmospheric nitrogen and oxygen in the upper atmosphere:

$$^{14}_{7}N + ^{1}_{0}n \rightarrow ^{12}_{6}C + ^{3}_{1}H \tag{2.5}$$

Tritium is transported by tritiated water molecules either in the form of tritium oxide (T_2O) or hydrogen tritium oxide (HTO). Tritium can then take part in the the hydrologic cycle [34]. The ratio of naturally occurring tritium to protium is $\frac{T}{H} = 10^{-16}$ [35].

Human-made tritium is produced as a by-product, in tertiary fission reactions, in energy generation. Small amounts of tritium are produced in nuclear power reactors by fast-neutron bombardment of the ^{10}B control rods or the ^{14}N in the residual air. Larger amounts are produced by thermal-neutron irradiation of ^{2}H, ^{3}He or ^{6}Li in the coolant of the reactor [36].

Tritium can be produced by including magnesium–lithium alloy cartridges into the aluminium cladding in a fission reactor (e.g. Windscale [37]). Purpose-built tritium production plants use linear accelerators to bombard either ^{3}He

or lithium, either in metallic form or in a compound [38].

Most European fusion reactors currently buy tritium from the CANDU reactors in Ontario, Canada [39].

2.2.2 Radioactive Decay

Tritium is the most unstable natural isotope of hydrogen, it undergoes nuclear decay in order to become stable. Tritium decays to the nearest stable atomic species, ^{3}He, via β^- decay. During β^- decay a neutron in an atom's nucleus undergoes transmutation into a proton by emitting an electron, maintaining the same nucleon number but increasing the proton number by one. Equation 2.6 shows tritium's β^- decay.

$$^3_1H \rightarrow ^3_2 He^+ + e^- + \overline{\nu_e} \tag{2.6}$$

Tritium decays with a half-life of $t_{\frac{1}{2}} = 12.43 \pm 0.04$ years. The average energy of the beta particle that is emitted during tritium decay has 5.52 ± 0.02 keV [40] of energy, with a maximum energy of 18.6 keV [41].

In equation 2.6 ^{3}He has a net positive electrical charge, a *free electron* from the β^- decay of a neighbouring tritium atom is captured by the positively charged atom to neutralise the overall net charge of the atom.

Due to tritium decay, the amount of tritium in a sample decreases over time as it decays into helium. Helium is more stable than tritium, so the amount of activity in a sample will also decrease over time [40].

2.3 Uranium

2.3.1 Physical Properties & Characteristics

Uranium is an actinide series element with a nuclear proton content of 92. It is the largest naturally occurring element (with any notable abundance) in

the periodic table. Uranium was discovered as a unique element in 1789 by Martin Heinrich Klaproth, it was named after the planet Uranus. Klaproth discovered UO_2, which was mistakenly thought to be its elemental form for 50 years. This only became apparent in 1841, when Eugene-Melchior Peligot discovered its actual elemental form of uranium, and then reduced Klaproth's dioxide form into metallic uranium [42].

Relative Atomic Mass	238.029	[43]
Density	$19.1\ \mathrm{g \cdot cm^{-3}}$	[43]
Ionisation Energy	$1st = 597.64\ \mathrm{kJ \cdot mol^{-1}}$	[43]
	$2nd = 1022.7\ \mathrm{kJ \cdot mol^{-1}}$	[43]
Non-bonded Atomic Radius	0.241 nm	[43]
Covalent Radius	0.183 nm	[43]
Electronegativity	1.7 (Pauling scale)	[43]
α - Decay Half-life of Key Isotopes	$^{238}U = 4.468 \cdot 10^9$ yr	[42]
	$^{235}U = 7.038 \cdot 10^8$ yr	[42]
Crystal Structure	orthorhombic	[42]
Crystal Structure Cell Parameters of α-U	a: 285.37 pm	[44]
	b: 586.95 pm	[44]
	c: 495.48 pm	[44]
	$\alpha = \beta = \gamma = 90^\circ$	[44]

TABLE 2.1: Some physical characteristics of uranium

Table 2.1 contains some of the physical characteristics of uranium at room temperature and equation 2.7 shows the ground state e^- configuration of uranium [43].

$$[Rn]5f^3 6d^1 7s^2 \tag{2.7}$$

Uranium has electrons in the $5f$ sub-shell which makes it a part of the actinide group. All actinides share certain similar characteristics. They are transition metals (have a partially filled d sub-shell) and all exist in compounds and solutions in the form of cations. Most actinides have $5f$ orbitals that

contain *itinerant* electrons, meaning that they are delocalised, form chemical bonds and contribute to the electrical conductivity [42].

Uranium metal can exist in 3 distinct, temperature-induced *allotropic* forms. The three structural phases of uranium are the *α-, β-, and γ- phases*. Allotropes are forms of an element that have atoms that are arranged differently by chemical bonds. The most common phase of uranium, α-U, exists at temperatures up to T = 668 °C [42]. It has a face-centred orthorhombic structure with cell parameters: a = 285.37 pm, b = 586.95 pm, c = 495.48 pm [44], and density 19.1 $g \cdot cm^{-3}$ [43]. When α-U is heated to reasonably high temperatures it expands in an *anisotropic* manner, its density decreases, and a phase change happens at T = 668 °C.

At temperatures above T = 668 °C the $\alpha \rightarrow \beta$ phase change occurs and α-U becomes β-U, which exists between T = 668 °C and T = 776°C. The crystal structure then becomes tetragonal with cell parameters: a = b = 1075.9 pm and c = 565.6 pm, and density 18.11 $g \cdot cm^{-3}$ [45].

A second phase change occurs at temperatures above T = 776 °C, the $\beta \rightarrow \gamma$ phase change. The metallic uranium exists in the γ-phase at temperatures up to T = 1133 °C [42], at which point it reaches its melting point. The third allotropic form, γ-U, has a body-centred cubic structure [45] with cell parameter: a = b = c = 352.4 pm and density 18.06 $g \cdot cm^{-3}$ [46].

2.3.2 Depleted Uranium

In nature uranium exists as a mixture of the isotopes ^{234}U, ^{235}U and ^{238}U, in abundances of (0.005 ± 0.001) %, (0.720 ± 0.001) % and (99.275 ± 0.002) % respectively [47].

^{235}U has the ability to sustain a nuclear chain reaction, making it the isotope which is the most sought after. Enrichment techniques have been developed to enrich the naturally occurring uranium ore that can increase the

concentration of ^{235}U in a sample to 2 - 4 % for *low-enriched uranium*[48] and even higher to 20 - 88 % for *highly enriched uranium* (weapons-grade) [49]. The by-product of this process, *depleted uranium* (DU), has a decreased concentration of ^{235}U. DU has the same density and chemical properties as naturally occurring uranium, but has less than 30% of the radioactivity [50]. DU can be used for: shields to protect against ionising radiation in hospitals; counterbalance weights in aeroplane construction; containers for transport of radioactive sources; and historically small amounts are used in the formation of porcelains, glasses, and catalysts [48].

2.3.3 Radioactive Decay

The isotopes of uranium decay via the α-decay mode, the emission of two protons and two neutrons (a ^{4}He nucleus). Under α-decay, uranium is transmuted into: ^{230}Th in the case of ^{234}U; ^{231}Th in the case of ^{235}U; and ^{234}Th in the case of ^{238}U [50]. ^{235}U & ^{238}U are both progenitors of a decay series which includes other ^{x}U isotopes. ^{235}U is the progenitor of the *Actinium series* and ^{238}U is the progenitor of the *Uranium series*, which are both illustrated in figure 2.3.

2.3.4 Hazards to Health

Exposure to depleted uranium can result in toxicity due to both its chemical properties and its radiological properties.

Radiological Toxicity

Due to its decay via the α-decay mode, the penetrating ability of uranium's nuclear emission is very low. DU poses very little hazard unless ingested or inhaled [51]. Some of the decay products of uranium don't decay through the α-decay mode and so could, possibly, pose a slightly greater hazard.

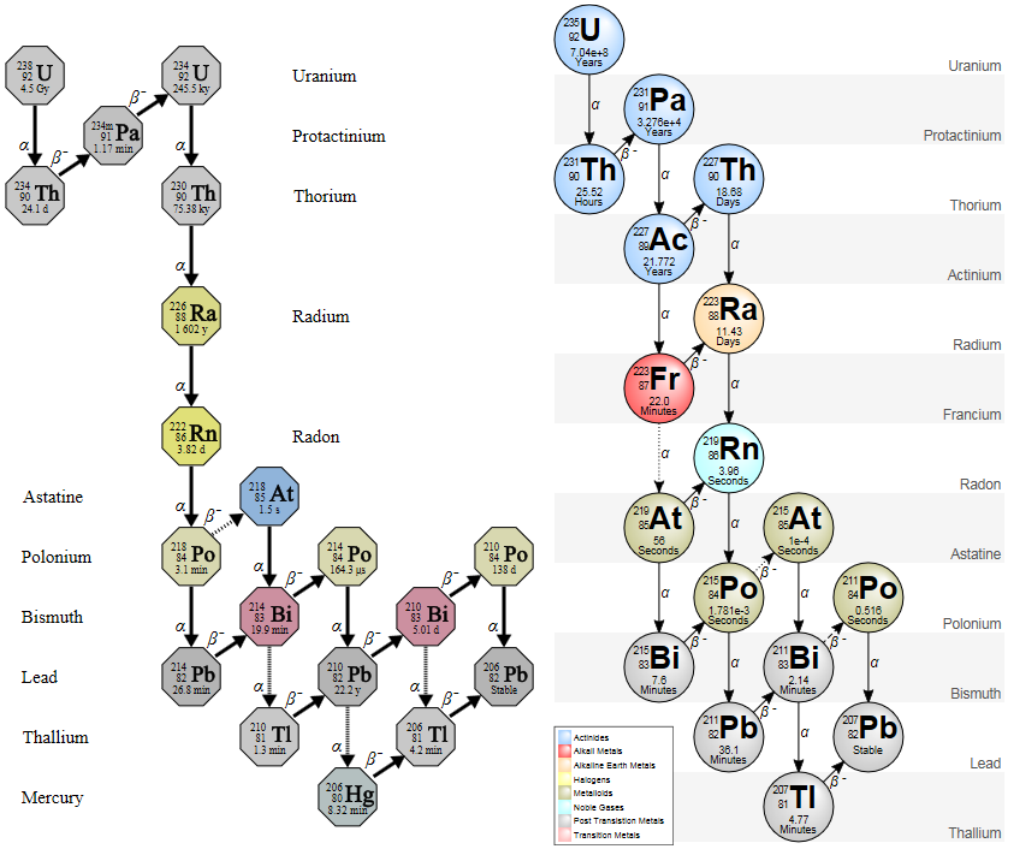

FIGURE 2.3: Uranium decay chain and Actinium decay chain. Dashed and dotted arrows are decay modes with < 1% probability and < 0.01% probability respectively. Image adapted from Wikimedia Commons. Created by Edgar Bonet, under the Creative Commons Attribution 3.0 Unported license.

Chemical Toxicity

Depleted uranium is retained mainly in the bones, liver, and kidneys of humans and animals. Only ≈ 5% of the DU that enters the body is actually absorbed into the bloodstream, and ≈ 95% is swiftly excreted in faeces [52]. Of the small percentage of DU that is absorbed, ≈ 67% is processed by the kidneys and leaves the body (in urine) within 24 hours [52]. Of the percentage that is not filtered by the kidneys, ≈ 66% is retained in the bones with a biological half-life of 70 - 200 days, DU is cleared from the rest of the body within a couple of weeks [53].

The severity of the harm from exposure to DU is determined by the *exposure pathway*. Table 2.2 shows the percentage of DU that will enter the bloodstream via the various exposure pathways, and the percentage retained over time in various parts of the body (based upon calculations using the figures quoted above).

Exposure Pathway	**% absorbed into bloodstream**	**% left after initial 24 hours**	**% in organs for up to 2 weeks**	**% left in bones (70 - 200 days)**
Inhalation	0.76 - 5.00 [53]	0.25 - 1.65	0.085 - 0.561	0.166 - 1.089
Ingestion	0.10 - 6.00 [53, 54]	0.033 - 1.98	0.011 - 0.673	0.022 - 1.307
Dermal	negligible	—	—	—

TABLE 2.2: The percentage of uranium absorbed into bloodstream due to different exposure pathways, and its persistence time in various parts of the human body

Chapter 3

Literature Review

3.1 Uranium Hydride (UH_3)

3.1.1 Physical Properties

UH_3, like its parent metal (elemental uranium), is toxic, pyrophoric and carcinogenic. The uranium-hydride reaction is considered a corrosion as it leads to the disintegration of the parent metal.

Uranium forms a binary compound with hydrogen in a metallically bonded lattice structure. The UH_3 can occur at temperatures as low as room temperature ($\approx 25°C$) up to $\approx 300°C$, at 1 atm pressure [55]. The activation energy of the uranium-hydrogen reaction has been shown (over a wide range of pressures: < 100 bar, and temperatures: $< 500°C$) to be 29.3 kJ$\cdot$ mol^{-1} for higher pressures and 28.5 kJ$\cdot$ mol^{-1} for lower pressures [56]. Under increased temperatures, desorption also begins to happen concurrently with absorption. Optimum temperature for maximum net production of UH_3 has been observed to be $\approx 225°C$ [57]. The activation energy for decomposition of UH_3 has been shown to be 43 kJ$\cdot$ mol^{-1} [58].

Uranium hydride is not an interstitial compound and so can't hold hydride ions in interstitial sites between uranium atoms in the lattice. This leads to an increase in the volume of the material, and so a reduction in the density [59].

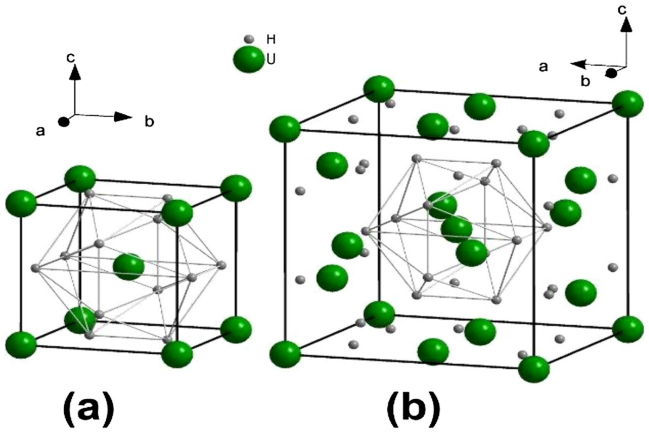

FIGURE 3.1: Crystal structure of (a) α-UH3 and (b) β-UH3. Image taken from [5]

UH_3 is a very brittle material due to hydrogen embrittlement, it generally exists as a very fine powder. A major issue with UH_3 is that it is pyrophoric, which means it can spontaneously ignite in air (though it is possible to form non-pyrophoric UH_3 [60]).

UH_3 can exist in two structural phases (shown in figure 3.1), the α- phase and the β- phase (β-UH_3 is, in general, the more common of the two phases) and the UH_3 crystal structure has been found to show some differences depending on the isotope of hydrogen that is bonding with the uranium. The differences, for the range of isotopes and their phases, are displayed in table 3.1.

UX_3	**Hydride Phase**	**Structure**	***a* (nm)**	**Density ($g \cdot cm^{-3}$)**	
X = H	α	Cubic	0.4160	11.12	[61]
X = D	α	Cubic	0.4150	11.33	[62]
X = T	α	Cubic	0.4142	11.55	[62, 63]
X = H	β	Cubic	0.6645	10.92	[64]
X = D	β	Cubic	0.6635	11.11	[65]
X = T	β	Cubic	0.6625	11.29	[62, 63]

TABLE 3.1: Characteristics of UH_3 under different hydrogen isotopes

The ratio of these two structural phases has been shown to be dependent

upon hydride formation rate. This means it's also indirectly determined by the formation temperature. UH_3 formed at room temperature was found to be 25 - 40 % α-phase, whilst UH_3 formed at 125 °C was just 15 % α-phase. UD_3 (having a slower reaction rate) formed at 25 °C was observed to be $\approx$ 50 % α-phase [61, 66].

This result was further supported by a study that compared the formation rate of UD_3 (by controlling gas influx, rather than sample temperature) to the composition of the resulting UD_3. An increase in the ratio of α:β phase was correlated with an increase in UH_3 formation rate [67].

It was observed that heating a UH_3 sample of $\approx$ 33 % α-phase at 250 °C for 100 hours, the sample converted to 100% β-UH_3 [61, 68]. This comprehensive phase change (to 100% β-UH_3) was retained when the sample was cooled 100 °C, this was taken to imply that temperature can induce an irreversible $\alpha \rightarrow \beta$ in UH_3. This prompted the suggestion that the α-phase of UH_3 could be just a transitional stage in the process of forming β-UH_3 (rather than a distinct, metastable phase) [61, 69].

3.1.2 The Uranium-Hydrogen Reaction

The $U + H_2$ reaction takes place between metallic uranium and gaseous hydrogen and results in uranium hydride (UH_3). The reaction progresses via equation 3.1.

$$2U + 3H_2 \rightleftharpoons 2UH_3 \tag{3.1}$$

During the reaction uranium metal is changed from an elemental form into a trivalent state, with the hydrogen gas being chemically entrapped. The reaction is exothermic and, as it is a corrosion, has a deleterious affect on the metallic uranium.

The progression of the UH_3 reaction front through the metal shows a square-root dependence on the rate on hydrogen pressure, $r \propto \sqrt{\rho}$, with some small deviations at higher pressures and at pressures approaching equilibrium [56].

An equation used to describe the UH_3 reaction as a function of temperature is the *Arrhenius equation*:

$$k = Ae^{-E_a/RT} \tag{3.2}$$

where k is the reaction rate, A is a "frequency term" or "pre-exponential term" (which depends on how often molecules collide when all concentrations are $1\,\mathrm{mol}\cdot\mathrm{l}^{-1}$), E_a is the activation energy of the reaction, R is the universal gas constant (which has the value: $8.314{\cdot}10^{-3}$ kJ·mol^{-1}·K^{-1}) and T is the temperature in kelvin. [70].

The Arrhenius equation (eq. 3.2) can also be rearranged to find the activation energy of the absorption reaction:

$$E_a = RT\,[ln(A) - ln(k)] \tag{3.3}$$

Equation 3.4 gives the desorption activation energy for metal hydrides, here ϕ is the temperature ramp rate in $\mathrm{K}\cdot\mathrm{min}^{-1}$, T_{max} is temperature of the maximum hydrogen desorption rate in K, R is the ideal gas constant and is equal to $8.314\ \mathrm{J}\cdot\mathrm{K}^{-1}\cdot\mathrm{mol}^{-1}$, E_A is the activation energy for the process in $\mathrm{J}\cdot\mathrm{mol}^{-1}$ and k_0 is a pre-exponential factor with units of s^{-1} [58].

$$E_a = RT_{max}^2 \frac{k_0}{\phi} e^{(-E/RT_{max})} \tag{3.4}$$

The reaction between uranium and hydrogen is generally considered to progress through four main stages [71, 72]:

1. **The induction period** - Hydrogen penetrates the surface passivation layer then gathers at the SPL-metal interface.
2. **The nucleation and growth period** - Discrete UH_3 sites form and grow.
3. **The bulk reaction period** - Adjoining UH_3 sites create a reaction front that engulfs the surface and progresses inwards consuming the U metal.
4. **The termination period** - Complete transformation of U to UH_3.

The Induction Period

During the induction period gaseous, molecular hydrogen is transported onto the surface of the metal. The gas must first penetrate the *surface passivation layer*, a layer covering the surface of the metal consisting of mostly oxides (but can also contain carbides, hydroxides and water [72]). The surface oxide layer acts as a barrier to hydrogen diffusion and so constitutes the main factor in the induction period. The rate at which permeation through the oxide layer takes place is determined by its thickness, its stoichiometry and the inclusion of impurities in the oxide layer (such as water or carbon) [73] or in the hydrogen gas (such as oxygen or CO) [74]. Environmental factors, such as temperature and gas pressure, also have an accelerating affect on the flux of hydrogen onto the metal surface.

The hydrogen molecules are dissociated (into either atomic or ionic form) both at the oxide-gas interface and at the oxide-metal interface via a process of dissociative chemisorption (the energy for this process to occur coming from either the kinetic energy of the incoming molecule or from translational and vibrational energy) [75].

The Nucleation and Growth Period

Hydride nucleation begins when the build up of hydrogen gas at sites on the metal-oxide interface exceeds a critical pressure, greater than the solubility

limit of hydrogen in uranium (the equilibrium pressure of uranium hydride), and very small amounts of hydride start to form spots at nucleation sites on the surface of the metal [76]. Localised gas build up between the oxide layer and the metal surface is determined by the difference between the rate at which the gas is permeating the oxide layer compared to the rate at which it is diffusing into the bulk of the metal. The locations of these nucleation sites are determined by a number of factors (besides localised hydrogen flux, as discussed above). Small hydride spots have been observed to form at points on the metal surface that offer lower energy routes for hydride precipitation, such as metal grain boundaries and twin boundaries [76, 77] and at sites of surface damage and impurity inclusion [78] (which has been attributed to surface strain of the metal, with a higher nuclei number density for the more strained surfaces [79]).

Four different families of hydride nuclei (that differ in density, size and growth rates) have been observed [80]:

(i) **Submicron sized, very dense blister-like nuclei** - This family of hydride nuclei appear under irregularities (such as scratches) in the oxide layer, which provide a preferential channel for hydrogen flux onto the metal surface.

(ii) **Blister-like, small nuclei** - These nuclei also appear mostly under scratches and defects in the oxide layer. They have a slow growth rate, thought to be caused by compression by the oxide layer. Their size seems to be determined by the thickness of the oxide layer, with a thinner oxide layer leading to larger blisters.

(iii) **Nucleation around carbide inclusions on the metal surface** - This family of hydride nuclei tend to be large and fast growing. Hydride nuclei at inclusion sites have been observed to penetrate deeper into the bulk

of the metal [81]. Inclusions create a discontinuity in the oxide layer exposing the metal surface to the gas.

(iv) **Fast-growing nuclei around other defects on the metal surface** - This family of hydride nuclei also tend to be large and fast growing. They grow at sites of microstructural discontinuities in the metal such as grain boundaries, twin boundaries and sharp geometrical features. These features of the metal have an affect on the oxide layer, creating preferential paths for the gas to reach the metal.

Due to the UH_3 being less dense, and therefore more voluminous, than metallic uranium (as shown in figure 3.1) some of the hydride nuclei will exert a pressure on the oxide layer and cause it to rupture creating a discontinuity in the oxide layer exposing the metal surface to the gas, which leads to a local increase in the amount of hydride on the metal surface [74].

The Bulk Reaction Period

Each of the hydride sites on the surface of the metal (described in the previous step) grow in size radially and linearly, until eventually they overlap to create a UH_3 layer at (what was) the metal-gas interface [82], the bulk reaction period then initiates [56]. A *reaction front* then progresses through the bulk metal in accordance with the *shrinking core model* [83].

The shrinking core model considers the metal as being progressively consumed by the reaction from the outside by a progressing reaction front (the metal-hydride interface) moving through the metal, radially inwards, from (what is initially) the metal-gas boundary towards the centre of the bulk metal (see figure 3.2).

The Johnson–Mehl–Avrami–Kolmogorov (JMAK) equation (equation 3.5) is an equation that can be applied to the shrinking core model, it describes the fraction of metal that has been converted to hydride as a function of time:

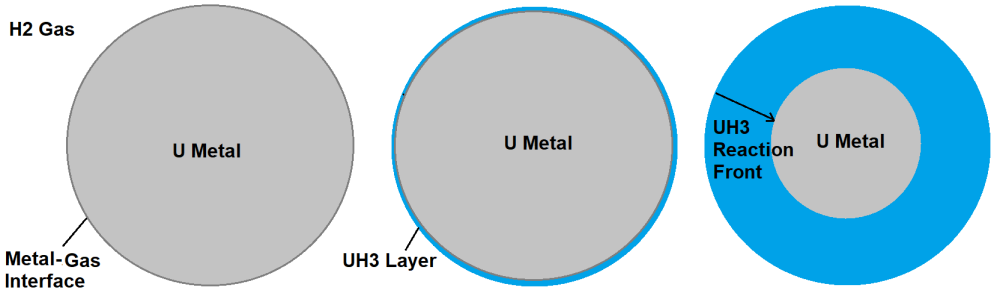

FIGURE 3.2: Graphic of The Shrinking Core Model (shown in 3 stages)

$$\alpha = 1 - e^{-kt^n} \tag{3.5}$$

where α is the fraction of metal that has been converted to hydride, k is a time constant, n is the growth exponent (an integer or half integer, its value depends on the geometry) [84]. For example, for continuous nucleation and three-dimensional (3D) spherical growth, $k = \frac{\pi}{3}$ and n = 4. The exponent n is the Avrami exponent [85].

Due to the $\approx$ 74% increase in volume (UH_3) stress causes the the corrosion product to crack, flake and fragment after the reaction front has passed through, along lines parallel it. This increases the ability of the H_2 gas to access the reaction region and increases the flux of the gas to the metal [86]. As the reaction front progresses through the bulk metal, the surface area of the metal available for reaction with the incoming gas is reduced with time, but the thickness and velocity of the reaction front remain constant [87] (which is reflected in the decreasing reaction rate). H_2 gas absorption rate curves show a decelerating parabolic curve for high temperatures that become an 'S' shape at slower absorption rates (lower temperatures and pressures), an example of this is shown in figure 3.3. The gas absorption rate during bulk reaction period shows a temperature and pressure dependence.

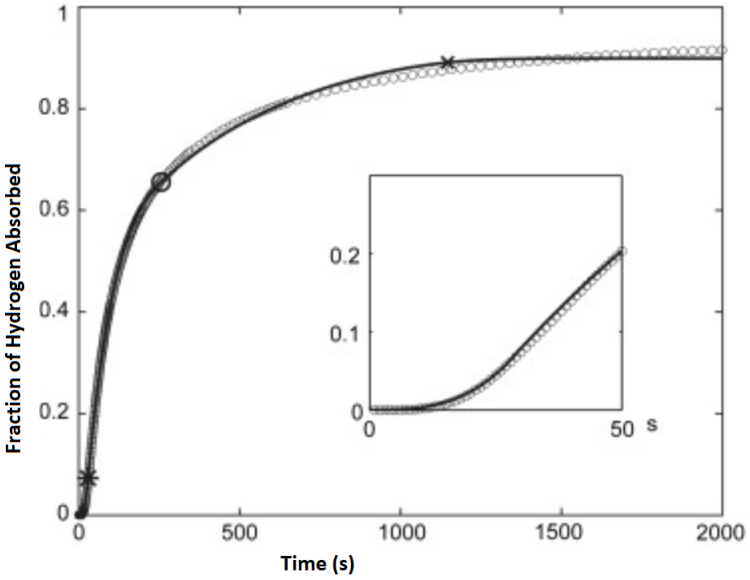

FIGURE 3.3: An example of an absorption curve of hydrogen gas by depleted uranium at 370 ^{o}C, the first 50s of the reaction is shown in the smaller box. Image adapted from [87]

The Termination Period

The termination period happens at the end of the bulk reaction stage, when the reaction front reaches the centre of the bulk metal, and the uranium metal has reached total transformation into UH_3.

3.2 The Palladium-Hydrogen System

Palladium, as with many metals, can accommodate hydrogen atoms in its lattice structure and store hydrogen in the form of a metal-hydride. In general, during the formation of metal-hydrides, the gaseous hydrogen is transported to the surface of the metal where the molecules dissociate into atomic form ($H_2 \rightarrow 2H$) and permeate through the metal. Bugaev et al. (2014 [88]) showed that during the isothermal absorption of hydrogen the Pd–Pd interatomic distances increased from 2.74 $\pm$ 0.01 to 2.81 $\pm$ 0.01 Å. Energy is usually required to be added to the system to overcome the activation energy barrier, but this is not the case with palladium as it has an extremely small

activation energy and so can readily absorb hydrogen at room temperature. It was reported by Kay et al. (1986 [89]) that the bulk diffusivity of hydrogen in palladium has an activation barrier of 5.39 $\pm$ 0.30 kcal/mol with a pre-exponential factor of (2.83 $\pm$ 0.05)$\cdot 10^{-3} cm^2/s$. The rate limiting step is the dissociation of the hydrogen molecules.

Palladium hydride can exist in two geometric phases: α-PdH and β-PdH (shown in figure 3.4). The two phases differ in the amount of hydrogen atoms per palladium atom that are held within the metal structure and in their crystal lattice constant (the $\alpha \rightarrow \beta$ phase changes constitutes a 10.4% isotropic volume increase [90]). Palladium and both its hydride phases have a face-centred cubic crystal structure (see table 3.2).

	Lattice Constant (nm at 298 K)	**Stoichiometry (PdH_x)**	**Crystal Structure**
Pd	0.3890 [91]	X=0.000	fcc
α-PdH	0.3894 [91]	X=0.015 [92]	fcc
β-PdH	0.4025 [91]	X=0.607 [93]	fcc

TABLE 3.2: Characteristics of palladium and its two hydride phases

Palladium hydride exists as a mixture of the α- and β- phases with the α / β ratio decreasing with increasing temperature up to a critical temperature T_c = 570 K, after which only the β-phase has been observed [94].

As described by Lacher (1937 [95]), it has been shown by Sieverts et al. (1932, 1935) that both hydrogen and deuterium dissolve in palladium in accordance with the $\sqrt{P}$ law only in the temperature range 600-1200° C. and pressures below 1 atm. Outside of these ranges the uptake of hydrogen deviates from the $\sqrt{P}$ law.

Palladium shows a characteristic preferential absorption for the lighter isotopes of hydrogen, which is what makes it such a good choice for use in

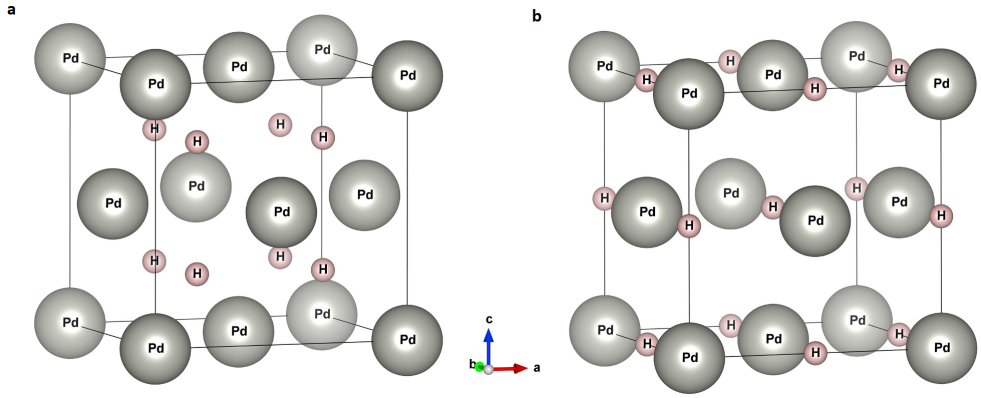

FIGURE 3.4: The unit cell of the hydride phases of palladium (with *a* being the low-temperature α-phase and *b* as the higher-temperature β-phase). Image taken from [98]

techniques intended to separate hydrogen isotopes that exist in gaseous mixtures. This isotopic effect becomes more pronounced at lower temperatures [96], it absorbs all hydrogen isotopes in general better at lower temperatures [97], [92].

Palladium's preference to absorb the lighter isotopes of hydrogen gives a separation factor greater than one [17]. The separation factor is defined by the ratio of the heavier-to-lighter isotopic concentration ratio in the gas phase to the same ratio in the solid phase (it is a ratio of those two ratios). For protium and deuterium gases, for example, it can be expressed as:

$$\alpha_{Pd} = \frac{D_{gas}}{H_{gas}} \cdot \frac{H_{solid}}{D_{solid}} \tag{3.6}$$

Where α_{Pd} is the separation factor of palladium, D_{gas} & H_{gas} are the amounts of deuterium and protium (respectively) in the gas phase, and H_{solid} & D_{solid} are the amounts of deuterium and protium (respectively) in the solid phase.

SRNL published a combination of experimental and calculated data on the separation factors of palladium for all the isotopologues of hydrogen (shown in Figure 3.5) [12].

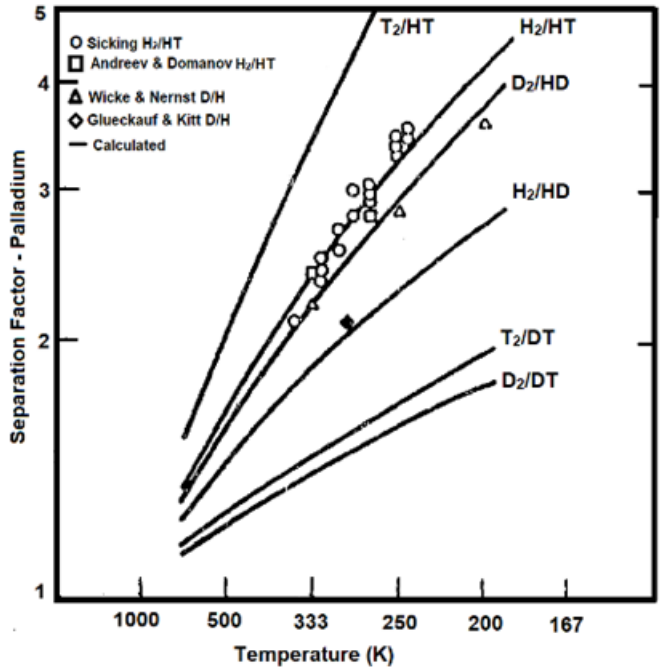

FIGURE 3.5: The separation factors of palladium for the isotopologues of hydrogen. Image taken from [12]

3.3 Isotopic Exchange

Isotopic exchange is the process of a material, when in the form of a compound with a given element, exchanging one isotope of the given element for another. The case that we are interested in (a metal-hydride and exchange between hydrogen isotopes) is described in equation 3.7

$$M_iT_j + H_2 \rightarrow M_iH_2T_{(j-2)} + T_2 \tag{3.7}$$

When considering the focus of this work, tritium storage and separation, this phenomenon could be exploited to ensure that all tritium has been retrieved from any storage or separating material. Any residual tritium in a material can be exchanged for protium or deuterium and removed. This could be useful when measuring tritium inventory, and for extracting residual tritium when disposing of spent storage or separation beds [99].

Chapter 4

Equipment & Techniques

4.1 Corrosion Gas Rig

Throughout the course of this work (§ 5.1, 5.2, 5.2.2 & 6.4), all formation and decomposition of metal hydrides was, except where explicitly stated, performed using a bespoke-made corrosion gas rig. The corrosion gas rig was used during these experiments because it serves two purposes. The first is to form and decompose metal hydrides using gases and metal samples whilst having the ability to maintain an inert environment, the second is to produce data by logging pressure change over time at various temperatures thus determine the amount of gas that has reacted with a metal sample.

4.1.1 The Gas Rig Set-up

The gas rig is a system of high-vacuum sealed pipes, various measuring devices, a furnace, and a gas inlet. It is used to transport a controlled amount of gas to a sample of material whilst it is being heated to a controlled temperature. A schematic of the gas rig set-up is shown in figure 4.1.

The gas rig consists of: multiple lengths of steel tubing with an internal volume of $V_{piping} = 97.56$ ml; a bespoke-made copper pipe cell of volume $V_{cell} = 82.75$ ml (with a custom-made metal crucible inside for holding the metal sample); an empty cylinder of volume $V_{cylinder} = 300$ ml; two pressure

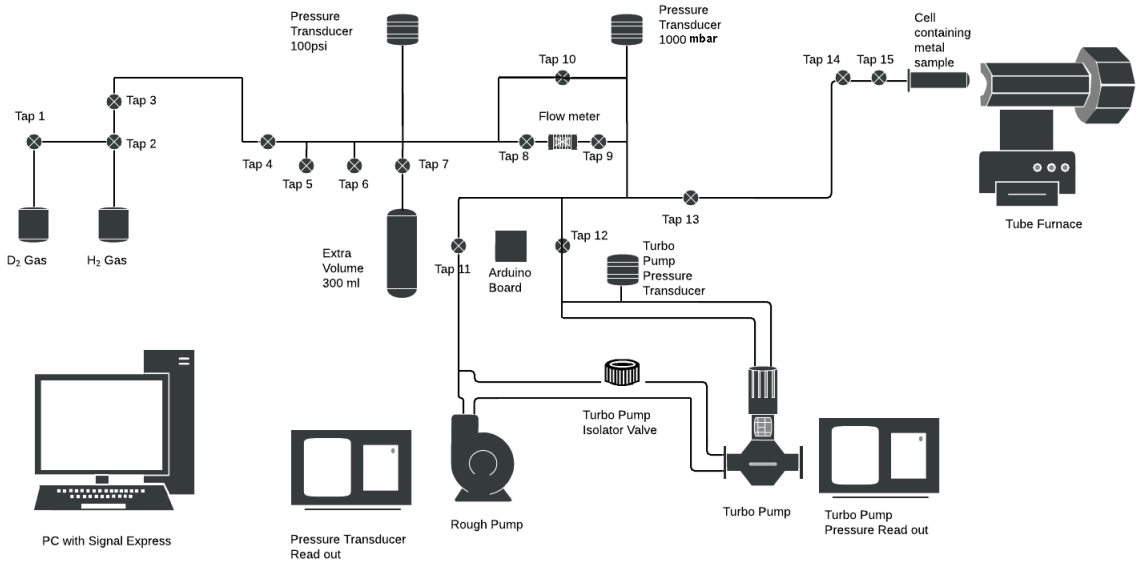

FIGURE 4.1: Schematic diagram of the bespoke gas rig

transducers; two pumps (a rough pump and a turbo pump); a furnace; and a gas inlet. The internal volume of the gas rig is $V_{rig} = 397.56$ ml and the total internal volume of the rig and the cell is $V_{total} = 480.31$ ml.

A thermocouple inside the furnace and the two pressure transducers all feed a data signal into a DAQ in combination with an Arduino board, for signal processing and data acquisition. The DAQ is attached to a desktop computer so the *National Instruments* software package *Signal Express 2015* can collate and log the data over the chosen time period.

4.1.2 Experimental Procedure

Inside an argon-environment glove box the powdered metal sample was placed into the crucible which was, in turn, inserted into the copper reaction cell. The reaction cell was then sealed and removed from the glove box. The cell was then attached to the gas rig on the far right side, inside the furnace. The furnace was heated to the required temperature whilst the entire gas rig was pumped down to a high vacuum (approximately $\approx 10^{-7}$ mbar) to

remove any impurities that might be desorbed from the sample or the gas rig system.

Once the furnace was heated to the required temperature and the system had stopped out-gasing then the cell was sealed using tap 15 in figure 4.1 (all other taps left open). The pumps were isolated from the rig. The rig was then filled with H_2 gas to the required pressure, from a gas bottle attached to tap 1, 2 or 3. The data logging function of Signal Express was started so that the pressure and time data was being logged. Tap 15 was then opened, turning it as quickly as possible to ensure enough time for the gas pressure to equilibrate before gas absorption starts. The metal sample in the cell would then start absorbing the gas, forming a metal hydride, and a formation curve (P vs t) would appear on the screen of the computer.

Once the internal gas pressure had reached a constant value, indicating that the reaction had stopped, the furnace was switched off and the system was left to cool down. The gas was not pumped out of the rig until the temperature dropped below 75 °C, this was to make sure that the metal-hydride was stable and no decomposition happened during the evacuation of the gas. Once the temperature was low enough then the pumps were used to evacuate all the gas out of the rig. The furnace was moved off the cell (because the cell was fixed in place but the furnace was not).

At this point a metal hydride had been formed and could be removed from the cell inside the glove box.

To decompose the metal hydride the gas rig and cell were again pumped down to a high vacuum and the furnace was then moved away from the cell and heated to the required temperature. Once the furnace was hot enough and the gas rig and cell were completely evacuated of all gas then the pumps were isolated, Signal Express was switched on to log data and the furnace was moved back onto the cell to decompose the metal-hydride. Once the

decomposition reaction had stopped (ie. the pressure had reached an equilibrium point), the furnace was switched off and the pumps were opened up to evacuate the decomposed gas.

In the case that the metal sample that was being used was uranium then the sample had to be powderised before the corrosion experiments could be performed. Before the uranium sample was placed inside the crucible and reaction cell it was polished by hand using a fine sand paper, until it became a silvery colour all over (see figure 4.2), to remove any surface impurities such as oxides and carbides (known as a *surface passivation layer*). The uranium sample was then placed in the crucible and cell and attached to the gas rig. To powderise the uranium, a metal hydride (UH_3) was formed and decomposed (as above) five times to ensure sufficient powderisation.

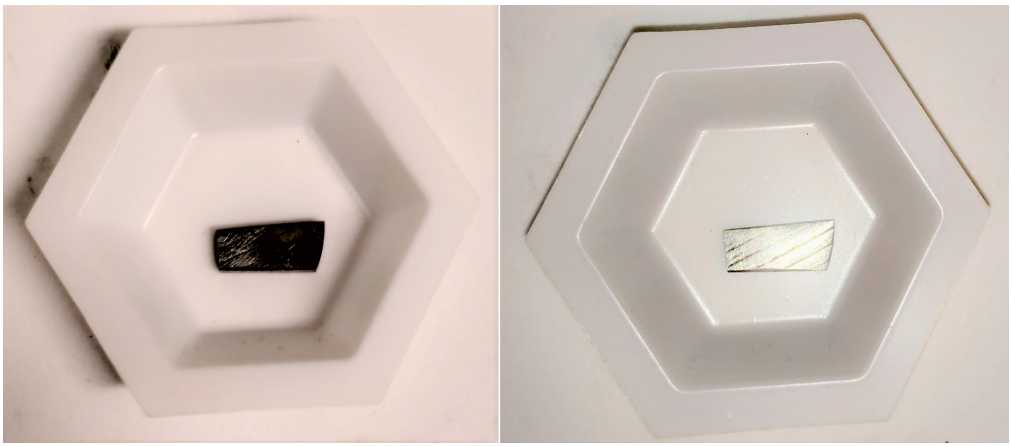

FIGURE 4.2: Uranium metal before (a) and after (b) polishing.

4.2 Thermogravimetric Analysis (TGA)

Thermogravimetric analysis is an analytical technique that heats a sample and tracks its percentage weight change with both time and temperature. TGA is performed in a controlled environment (often nitrogen or argon, to avoid unwanted reactions with the test sample) and the temperature of the sample is varied in a uniform and controlled way. The change in weight

of the sample upon heating can suggest either dehydration, decomposition or oxidation (if the test sample is analysed in an air/oxygen environment). Characteristic thermogravimetric curves have been established for various materials, these unique characteristic curves are related to the molecular structure of the sample and can be used to identify and characterise test samples.

4.2.1 The TGA Machine

A TGA machine is a purpose-built machine to perform thermogravimetric analysis on a test sample. The TGA machine used during this work was a *Mettler Toledo simultaneous TGA/DSC1* (a Windows-XP controlled instrument used in correlation with the STARe software). A schematic of the TGA set up used in this work is shown in figure 4.3.

The machine consists of a sample pan attached to a highly sensitive microbalance to accurately measure the weight of the test sample and a microfurnace, that houses the sample pan, to heat the sample during the analysis. The sample pan and furnace are sealed in an airtight housing with gas inlet and outlet tubes in order to control the environment in which the analysis takes place.

Data is output to a computer connected to the balance controller that can be used for analysis of the change in sample mass with either time or temperature.

In this work the data (presented in § 6.2) was considered for sample mass change with temperature for the purpose of assessing the amount of H_2 gas that was absorbed by the palladium sample during the PdH_x formation process (performed using the gas rig and the same method outlined in § 4.1). Unfortunately, no technique was conceived of to estimate the time lag for the system to equilibrate at a given temperature.

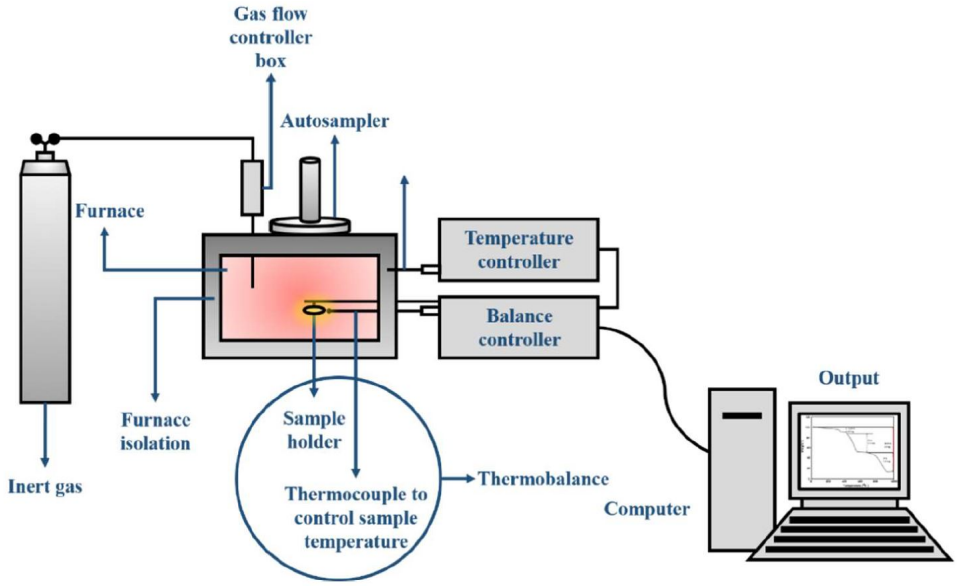

FIGURE 4.3: Schematic of the TGA set up used in this work. Image taken from [100].

4.3 X-Ray Diffraction (XRD)

X-ray diffraction is a technique that involves aiming x-rays at a material sample in order to reveal its structure and composition. It is a non-destructive technique that can be used for characterising materials or distinguishing between the different phases of solids.

When x-rays are incident on atoms in a crystal sample, inner shell electrons of the atoms are excited, the added energy resulting in a jump from an inner orbital shell to a higher shell, leaving an electron vacancy. When an electron relaxes into that vacancy x-rays of specific wavelengths are produced. The atom becomes a source of x-rays itself by absorbing and re-emitting x-rays isotropically. The energy of these characteristic emitted x-rays corresponds to a specific electronic transition.

4.3.1 The Bragg condition

In a crystalline material atoms are arranged in a lattice structure, giving a regular spacing between them. Layers of these regularly spaced atoms create parallel planes, with a regular spacing d (see figure 4.4). When x-ray waves are incident on the planes, the x-rays interact with the electrons of the atoms that constitute that plane. The re-emitted x-rays from successive lattice

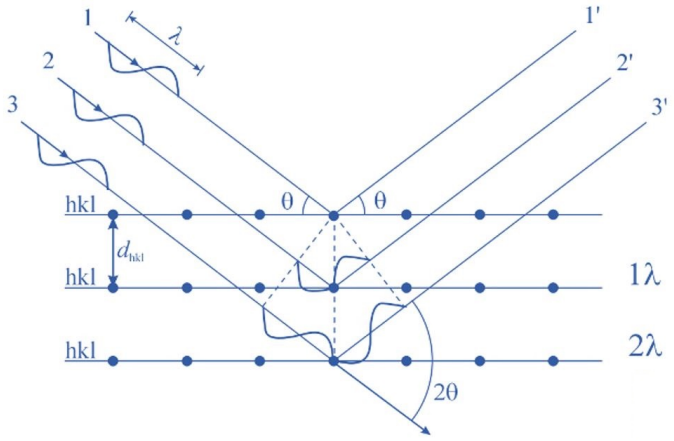

FIGURE 4.4: Diagram of Bragg diffraction. The x-rays are scattered by the planes of the crystal lattice. Image by University of Illinois

planes interfere with each other. This leads to constructive and destructive interference, and means that x-rays will only be detected from the sample at specific angles (as in figure 4.4). These specific angles occur when the Bragg condition is met (i.e. when the path difference is an integral number of wavelengths):

$$n\lambda = 2dsin\theta \tag{4.1}$$

The Bragg equation (4.1) does not give a full explanation of x-ray scattering from a crystal structure.

4.3.2 The Reciprocal Lattice

The reciprocal lattice represents the Fourier transform of a crystal lattice structure (a periodic spatial function in real-space). The reciprocal lattice exists in

reciprocal space (sometimes called momentum space or k-space).

If we consider a (real-space) vector that represents the position of a lattice point:

$$\vec{\mathbf{R}}_{\mathbf{n}} = n_1\hat{\mathbf{a}}_1 + n_2\hat{\mathbf{a}}_2 + n_3\hat{\mathbf{a}}_3 \tag{4.2}$$

then its corresponding vector in reciprocal space can be defined as:

$$\vec{\mathbf{G}}_{\mathbf{m}} = m_1\hat{\mathbf{b}}_1 + m_2\hat{\mathbf{b}}_2 + m_3\hat{\mathbf{b}}_3, \quad \textit{where} \quad \hat{\mathbf{a}}_i \cdot \hat{\mathbf{b}}_j = 2\pi\delta_{ij} \tag{4.3}$$

The reciprocal primitive vectors, $\hat{\mathbf{b}_1}$, $\hat{\mathbf{b}_2}$, $\hat{\mathbf{b}_3}$, can be found from the (real-space) primitive vectors, $\hat{\mathbf{a}_1}$, $\hat{\mathbf{a}_2}$, $\hat{\mathbf{a}_3}$, by:

$$\hat{\mathbf{b}_1} = 2\pi\frac{\hat{\mathbf{a}_2}\times\hat{\mathbf{a}_3}}{\hat{\mathbf{a}_1}\cdot(\hat{\mathbf{a}_2}\times\hat{\mathbf{a}_3})} \quad \hat{\mathbf{b}_2} = 2\pi\frac{\hat{\mathbf{a}_3}\times\hat{\mathbf{a}_1}}{\hat{\mathbf{a}_2}\cdot(\hat{\mathbf{a}_3}\times\hat{\mathbf{a}_1})} \quad \hat{\mathbf{b}_3} = 2\pi\frac{\hat{\mathbf{a}_1}\times\hat{\mathbf{a}_2}}{\hat{\mathbf{a}_3}\cdot(\hat{\mathbf{a}_1}\times\hat{\mathbf{a}_2})} \tag{4.4}$$

4.3.3 The Laue Condition

If we represent the direction of the incident x-ray as the vector $\hat{\mathbf{n}}$ and the direction of the scattered x-ray as the vector $\hat{\mathbf{n}}'$, then the wave vectors are given by:

$$\vec{\mathbf{k}} = \frac{2\pi}{\lambda}\hat{\mathbf{n}} \tag{4.5}$$

$$\vec{\mathbf{k}}' = \frac{2\pi}{\lambda}\hat{\mathbf{n}}' \tag{4.6}$$

then the scattering vector is given by:

$$\vec{\Delta\mathbf{k}} = \vec{\mathbf{k}}' - \vec{\mathbf{k}} \tag{4.7}$$

if we take $\hat{\mathbf{a}_1}$, $\hat{\mathbf{a}_2}$ and $\hat{\mathbf{a}_3}$ to be the primitive vectors of the crystal lattice unit cell (see figure 4.5) then the components of the scattering vector could be written as:

$$\hat{\mathbf{a}}_1 \cdot \vec{\Delta\mathbf{k}} = 2\pi h, \quad \hat{\mathbf{a}}_2 \cdot \vec{\Delta\mathbf{k}} = 2\pi k, \quad \hat{\mathbf{a}}_3 \cdot \vec{\Delta\mathbf{k}} = 2\pi l \tag{4.8}$$

where (*h,k,l*) are integer numbers called the *Miller indices*. These are the conditions that the scattering vector must satisfy, called the Laue equations. Each

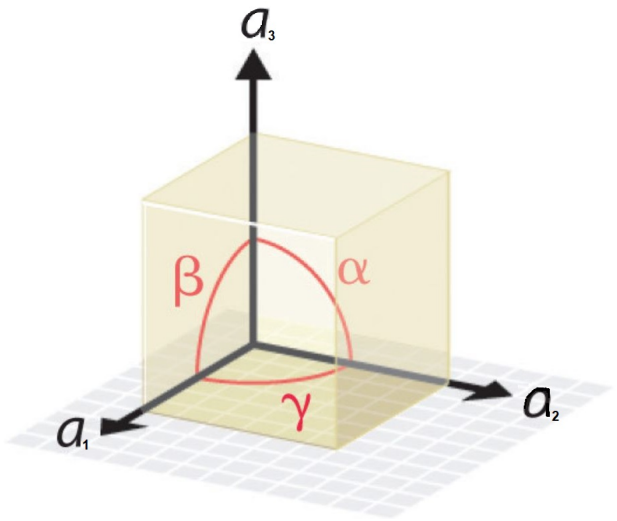

FIGURE 4.5: The primitive unit cell of a crystal lattice structure. a_1 = cell parameter along the x axis, a_2 = cell parameter along the y axis, a_3 = cell parameter along the z axis, α = angle in the yz plane, β = angle in the xz plane, γ = angle in the xy plane. Image from [101].

choice of integer values (*h,k,l*) determines the scattering vector.

We must now define a *reciprocal lattice vector* $\vec{\mathbf{G}}$, where the vectors of the reciprocal lattice are $\hat{\mathbf{b_1}}$, $\hat{\mathbf{b_2}}$ and $\hat{\mathbf{b_3}}$, and such that:

$$\vec{\mathbf{G}} = \Delta\vec{\mathbf{k}} = \vec{\mathbf{k}}' - \vec{\mathbf{k}} \tag{4.9}$$

the Laue condition states that constructive interference will occur provided that the change in wave vector ($\vec{\mathbf{G}}$) is a vector of the reciprocal lattice.

Bragg-Laue Equivalence

The Bragg condition (equation 4.1) is a specific example of the Laue condition (equation 4.9). For elastic scattering $|\overrightarrow{k}| = |\overrightarrow{k'}|$ the Laue condition becomes:

$$|\overrightarrow{G}| = 2|\overrightarrow{k}|sin\theta \tag{4.10}$$

we know that:

$$|\overrightarrow{G}| = \frac{2\pi}{d} \; and \; |\overrightarrow{k}| = \frac{2\pi}{\lambda} \tag{4.11}$$

Therefore:

$$\frac{2\pi}{d} = 2\frac{2\pi}{\lambda} sin\theta \Rightarrow 2dsin\theta = \lambda \tag{4.12}$$

If there is a common factor n in (hkl) of equation 4.3 then:

$$d(hkl) = \frac{d(h/n, k/n, l/n)}{n} \tag{4.13}$$

and equation 4.12 becomes:

$$2dsin\theta = n\lambda \tag{4.14}$$

4.3.4 The Ewald Sphere

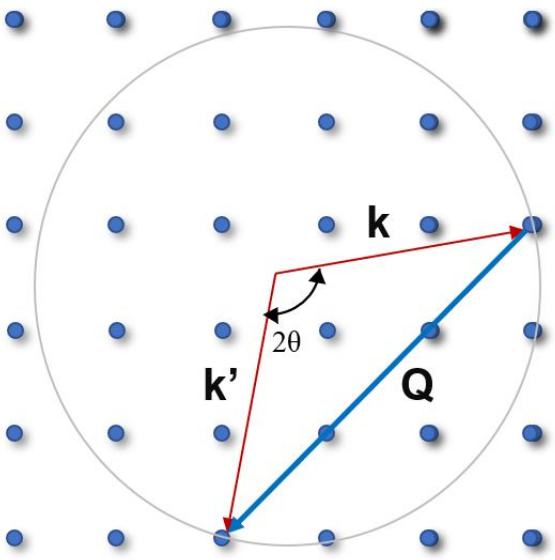

FIGURE 4.6: A construction of an Ewald sphere illustrating the Laue condition.

The Ewald sphere (figure 4.6) is a way of visualising the Laue condition. The sphere is constructed by positioning the incident wavevector, $\vec{\mathbf{k}}$, so that it terminates at a reciprocal lattice point. A sphere is drawn centred on the origin of $\vec{\mathbf{k}}$ with radius $k = \frac{2\pi}{\lambda}$. A diffracted beam will be formed if this sphere intersects another reciprocal lattice point and a vector, $\vec{\mathbf{k}}'$, can be drawn from the centre of the circle to this reciprocal lattice point. The angle θ between

the two vectors is the Bragg angle in equation 4.1. The two reciprocal lattice points are connected by a vector $\vec{\mathbf{Q}} = \vec{\Delta\mathbf{k}} = \vec{\mathbf{k}'} - \vec{\mathbf{k}}$. This is the definition of the reciprocal lattice vector, $\vec{\mathbf{G}}$, in equation 4.9, therefore $\vec{\mathbf{Q}} = \vec{\mathbf{G}}$, which is the Laue condition given in § 4.3.3.

4.3.5 XRD Peak Broadening

The effect of peak broadening in x-ray diffraction has contributions from two sources:

1. Contributions from the sample
2. Instrumental contributions

Instrumental contributions

The instrumental contribution to XRD peak broadening has a number of causes. The source of X-rays has some finite physical size, coupled with axial divergence of the incident and diffracted beams, means that any detected x-rays will be measured as a (small) range of angular values rather than a sharp, distinct angle. This is the resolution of the diffractometer, the effect increases with 2θ value. The x-rays produced by the instrument are not perfectly monochromatic, this means the wavelength of the incident x-rays also consist of a small range of wavelengths, which also makes up part of the instrumental contribution to peak broadening.

Sample contributions

The contribution from the sample comes from imperfections in the crystal lattice structure. Crystal lattice structures can suffer from lattice distortions due to dislocations of the atoms that make up the lattice, this is the cause of lattice micro-strain.

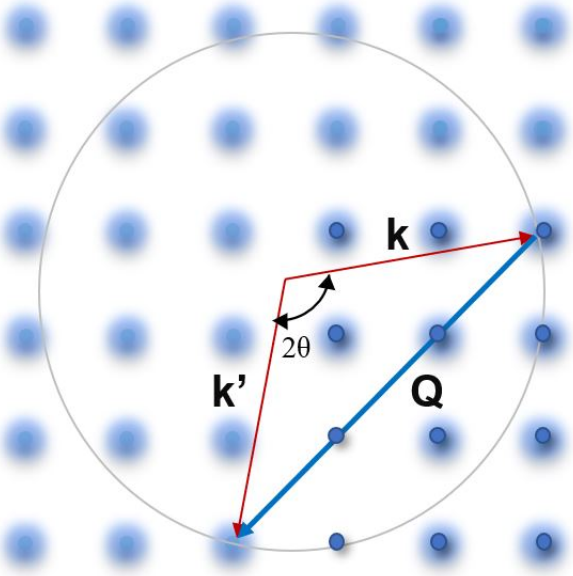

FIGURE 4.7: An Ewald sphere demonstrating XRD peak broadening

This peak broadening effect from lattice distortions can be shown using an Ewald sphere (see figure 4.7). Because reciprocal space is determined by the Fourier transform, the result of real-space lattice distortions is to decrease the definition of lattice points in reciprocal space, and, therefore, increase the volume over which the reciprocal lattice vector intersects the lattice points.

4.3.6 The X-Ray Diffractometer

The x-ray diffractometer is a device that uses X-ray diffraction to characterise the structure of a crystalline sample. It works by directing x-rays at a sample which has been placed on the machine's stage. The 2θ angles formed by the incident and reflected x-rays can tell us the structure and type of the crystal lattice of the sample and also the constituent elements that make up the sample.

All XRD analysis during this work (presented in §5.2.3) was performed using a Philips X'pert diffractometer (figure 4.8) with a copper target anode with K_α = 1.540598 Å and K_β = 1.544426 Å. The 2θ angles, and intensities, that

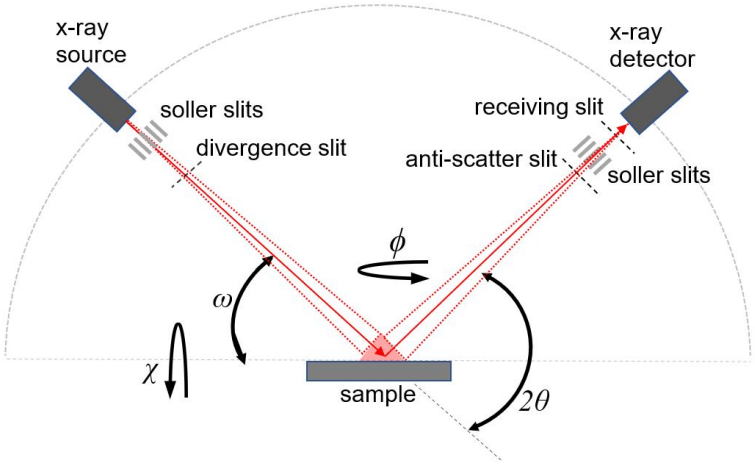

FIGURE 4.8: Schematic diagram of the Philips X'pert diffractometer in the scattering plane.

are detected are characteristic of elements and compounds, and their structural phases. The 2θ positions of the peaks for the XRD pattern of uranium is shown in figure 4.9 and some of the largest peaks are labeled with the Miller indices of their corresponding lattice planes.

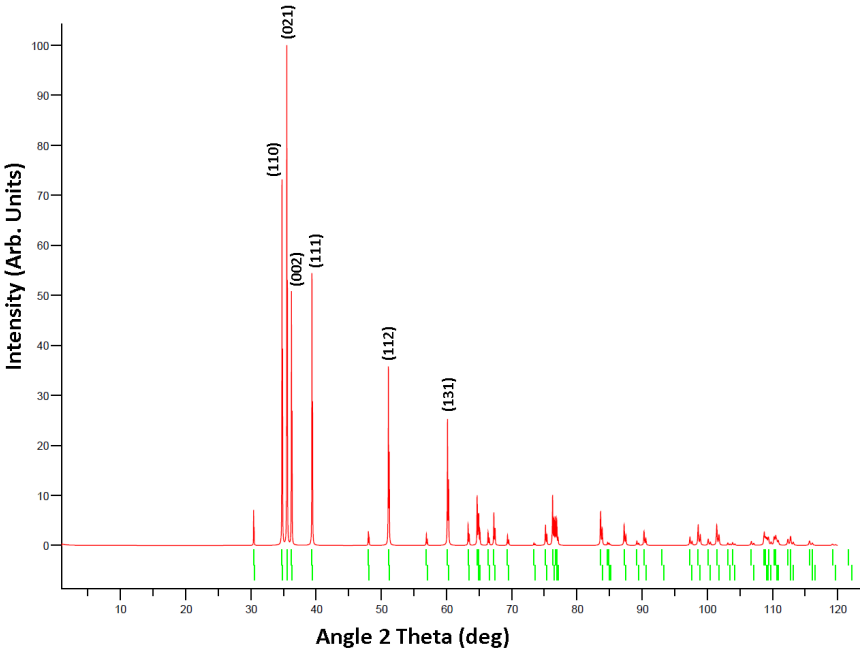

FIGURE 4.9: X-ray diffraction pattern of uranium. Some of the largest peaks are labeled with the Miller indices of their corresponding lattice planes. Image produced using data from *National Chemical Database Service*.

4.3.7 The PseudoVoigt Peak Fitting Function

The PseudoVoigt Peak Fitting Function is a probability distribution used to analyse data from spectroscopy or diffraction experiments. It is a linear combination of the Gaussian and the Lorentzian distributions (with η giving the weighting between the two functions) [102]. The three fitting functions, and the calculation for Full Width Half Maximum used in each, are given by equations 4.15, 4.16 & 4.17.

The Gaussian Function:

$$f_{Gaussian}(x, c, \sigma, A) = Ae^{-\frac{(x-c)^2}{2\sigma^2}}, FWHM_{Gaussian} = 2\sqrt{2ln2\sigma} \tag{4.15}$$

The Lorentzian Function:

$$f_{Lorentzian}(x, c, \sigma, A) = \frac{A}{\pi}\frac{\sigma}{(x-c)^2+\sigma^2}, FWHM_{Lorentz} = 2\sigma \tag{4.16}$$

The PseudoVoight Function:

$$f_{PseudoVoight} = \eta f_{Gaussian} + (1-\eta) f_{Lorentzian} \tag{4.17}$$

A= maximum peak height; c= position peak centre; σ= standard deviation.

The PseudoVoight peak fitting function was applied to experimental XRD results in this work, which can be seen in § 5.2.3.

4.4 X-ray Tomography

X-ray tomography (XRT) is an imaging technique that works by directing x-rays through the sample under consideration at a detector, which then measures the intensity of the signal that still remains after passing through the sample. X-ray attenuation is measured and an image of the sample is constructed based upon the intensity of the x-ray signal at the detector. The

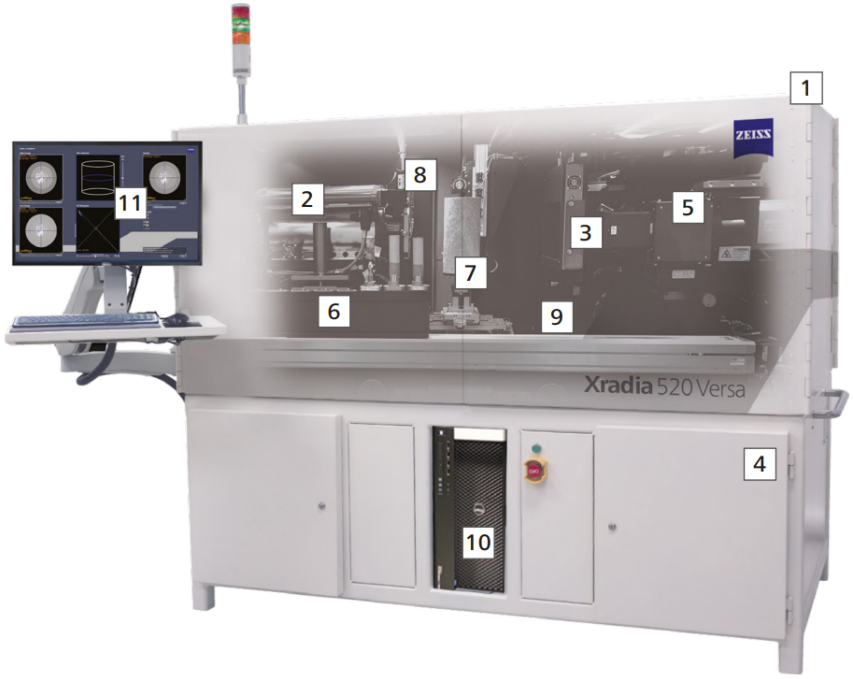

FIGURE 4.10: The ZEISS Xradia 520 Versa XRT Machine

degree of x-ray attenuation at a given point is a measure of the (straight line) density of the (sample) material that the x-rays have passed through at that point. XRT can image high-resolution, micron-scale structural details of a material [103].

An XRT machine rotates a sample through 360° whilst firing the x-rays at it. It measures the attenuation of x-rays that have passed through the sample at every point in the rotation in order to build up a 3-dimensional picture of the density measurements.

The XRT machine used in §5.2.5 of this work was a ZEISS Xradia 520 Versa, shown in figure 4.10:

1. X-ray Microscope
2. X-ray Source
3. Detector System
4. System Stability for Highest Resolution
5. System Flexibility for a Diverse Range of Sample Sizes

6. Autoloader Option
7. Sample Stage
8. X-ray Filters
9. In Situ and 4D Solutions
10. Instrument Workstation
11. Software

The ZEISS Xradia 520 Versa XRT uses a unique, two-stage magnification architecture. Sample images are initially enlarged through geometric magnification as they are in all conventional XRT machines. The image is then projected onto a scintillator, which converts X-rays to visible light, and is then magnified by an optical objective before reaching the detector. This unique feature, along with the conventional magnification architecture for comparison, is shown in figure 4.11.

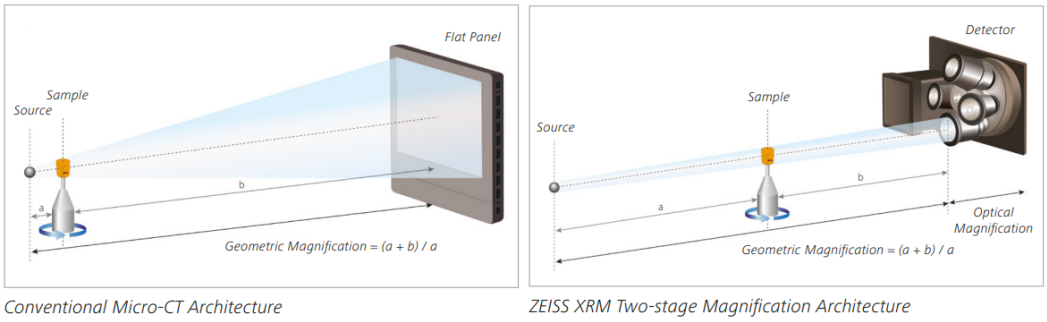

FIGURE 4.11: Left: Conventional Micro-CT Architecture, Right: ZEISS XRM Two-stage Magnification Architecture. Image from [104].

Chapter 5

Uranium Hydride

5.1 Powderising Uranium Metal

A method that is often used to powderise bulk uranium metal is to perform a number of hydride formation and decomposition cycles. Each formation - decomposition cycle causes the metal to expand and contract isotropically, creating stresses and strains in the lattice structure (as explained in § 3.1.2). The stresses and strains cause the metal to crack and crumble and, after repeated cycles, become a fine powder. The size of the particles produced by this method has a minimum limit. It has been found previously, during the research of others (Banos et al., 2018 & 2017 [5, 105]) that this minimum limit is reached after 6 formation-decomposition cycles (at formation temperatures of both 100°C and 320°C). It was also claimed by Bloch (2003 [106]) that repeated hydride-dehydride cycles (under formation conditions T = 370°C and P_{H2} = 626 mbar) led to unchanging kinetics after 6 cycles. Bloch also described, in the same 2003 paper, findings by Caralp-Amilhat et al. (1970 [107]) of similar experiments measuring particle size indicating that the specific surface areas of uranium samples and their hydrides approach unchanging values following several such cycles (11 cycles at 0°C and five cycles at 320°C). However during the current work it was found that the minimum limit was reached after just 4 cycles (at formation temperatures of 250°C and at starting H_2 gas pressure of 1900 mbar). The graph in figure 5.1 shows the

H_2 gas pressure change data of 2.5 grams of uranium metal during 5 initial formation half-cycles (starting from a bulk metal sample that had never been subjected to the formation-decomposition cycle process) at a formation temperature of 250°C and figure 5.2 shows the data from the 5 decomposition half-cycles of the same sample. The formation-decomposition cycles were all performed using the gas rig set up and experimental method described in § 4.1.

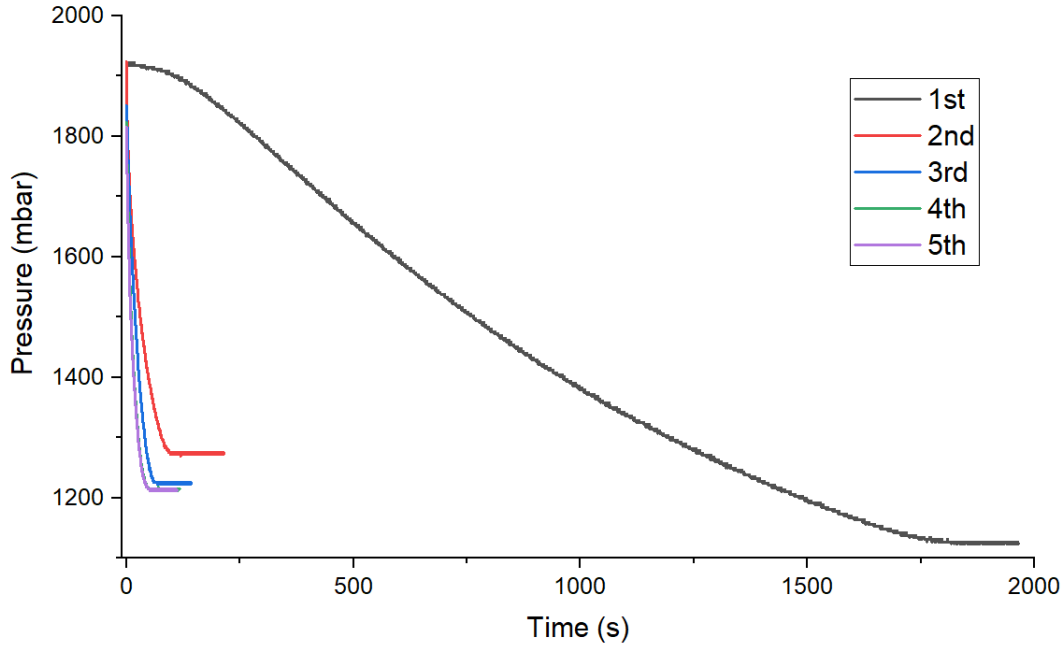

FIGURE 5.1: The five hydride formation cycles that powderise uranium. T=200°C, P = 1900mbar.

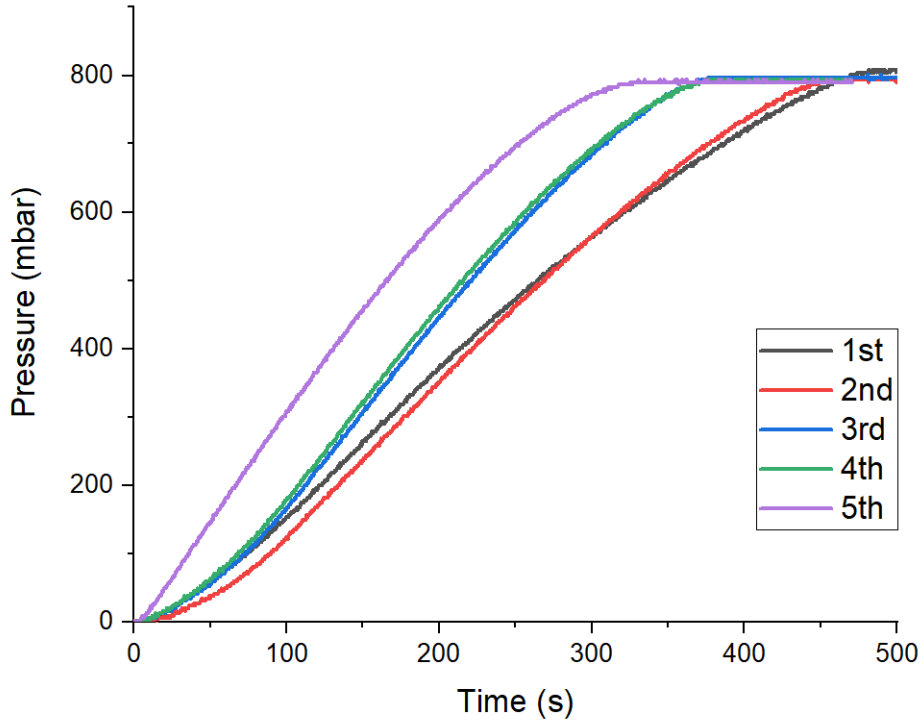

FIGURE 5.2: The five hydride decomposition cycles that powderise uranium. T = 500°C.

It is quite clear from the graph of the 5 initial formation half-cycles (figure 5.1) that the difference in H_2 gas uptake rate between formation half-cycles 1 and 2 are significantly greater than the differences between subsequent formation half-cycles, this suggests that the bulk of the powderisation happens during the first formation half-cycle.

The curves for formation half-cycles 2, 3, 4, and 5 appear to be, in comparison to the curve for formation half-cycle 1, all bunched up close together near the *y*-axis, with little difference between them. The curves for formation half-cycles 4 and 5 are indistinguishable from each other (the green curve can not be seen as it is perfectly covered by the purple curve), this suggests that the powderisation process ended with formation half-cycle 4 and the uranium metal particles were no longer reducing in size.

The H_2 gas pressure at which the sample stopped absorbing gas is different for each curve (except 4 and 5), this is assumed to be because a small

Cycle number	Time (s) at P = 200mbar	Time (s) at P = 600mbar	Gradient (mbar/s)
1	121.0	321.5	1.995
2	133.5	319.0	2.156
3	111.5	261.5	2.667
4	107.0	256.5	2.676
5	66.5	204.5	2.899

TABLE 5.1: The gradients of the curves of the 5 initial decomposition half-cycles.

amount of residual hydrogen remained in the sample after the decomposition half cycles. It could also be from a small amount of oxidisation of the sample at the high temperatures during hydride decomposition, which would reduce the samples capacity to accommodate H_2 gas.

To analyse the change in desorption rate during the 5 cycles the gradient of each curve was calculated (using equation 5.1) between the points on the curve where pressure was equal to 200mbar and 600mbar. The gradients of these curves are shown in table 5.1. The gradients were calculated using the standard method:

$$m = \frac{y_2 - y_1}{x_2 - x_1} \tag{5.1}$$

The gradients for the 5 decomposition half-cycles showed the same consistently progressive nature as the formation half-cycles. The gradient of the 3rd and 4th curves were almost identical. The results for decomposition did differ from those of formation in that there was a large difference between the curves for the 4th and 5th cycle (in figure 5.2).

5.1.1 Discussion

UH_3 formation-decomposition cycles were used to powderise a 2.5g uranium metal sample. These powderisation experiments showed results that were in disagreement with previously found results of Banos et al. (2018 [71] & 2017

[105]), Bloch (2003 [106]) and Caralp-Amilhat et al. (1970 [107]). All of whom claimed that more cycles (6, 6, & 5, respectively) were required than the 4 cycles demonstrated in this work.

This claim requires further verification by a more direct means of measuring the particle size. A more informative method of investigating this would be to remove the sample from the gas rig after every hydride formation-decomposition cycle and measure the particle size directly using a characterisation technique that is capable of performing such a measurement. For example, scanning electron microscopy (SEM) would be such an appropriate technique, or make a direct measurement of total surface area of the sample using Brunauer-Emmett-Teller (BET) surface area analysis.

5.2 Heat Treating Depleted Uranium

During earlier work it was discovered that heat treatment of a depleted uranium sample at 700 ^{o}C for an hour brought about a permanent change in the uptake rate of hydrogen gas by the metal sample.

Figure 5.3 shows two curves of pressure change over time during a UH_3 formation experiment. The two curves show the same 1.8 gram depleted uranium sample at 200 ^{o}C and $P_i = 2050$ mbar H_2 gas pressure. The red curve shows the reaction rate after the metal sample had been heat treated for one hour at 550 ^{o}C and the blue curve shows the reaction after heat treatment for one hour at 700 ^{o}C. The dashed line at $y = 1738.33$ mbar is the resulting pressure change when transporting the gas into an empty reaction cell (without any metal sample) under the same conditions, with the volume of the sample taken into account. This was determined by performing a procedure identical to those used in the hydride formation experiments in figure 5.3 (T = 200 °C and P_i = 2050 mbar), being performed with no uranium sample in the cell. During this empty-cell experiment a pressure of 1738 mbar was

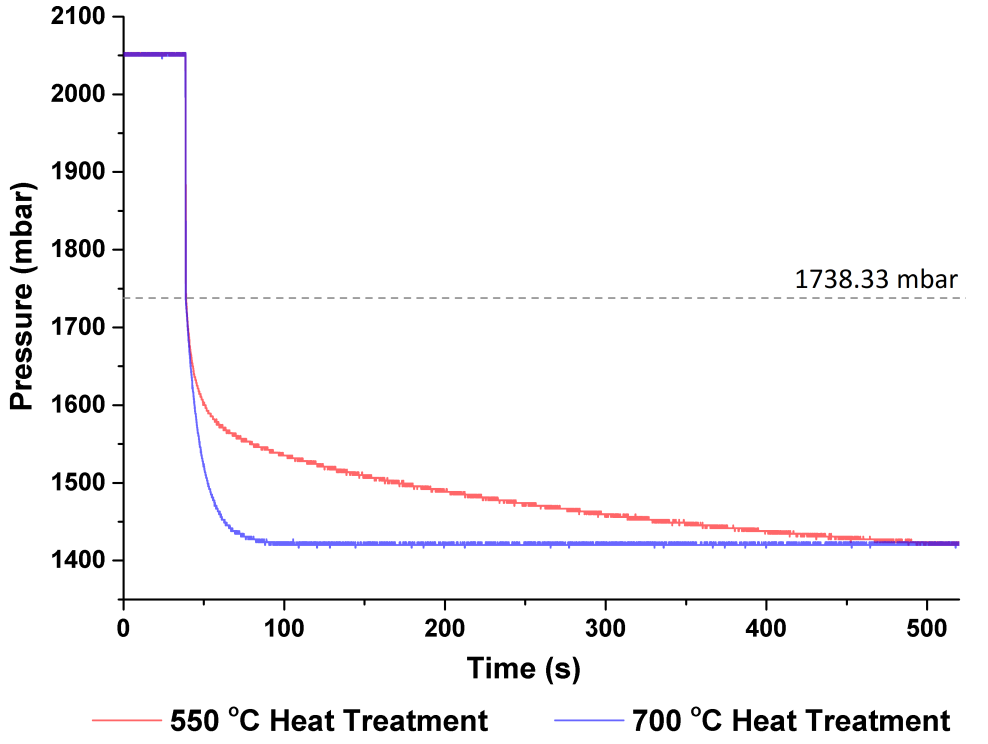

FIGURE 5.3: Graph showing two curves of pressure over time during a UH_3 formation experiment, using 1.8 gram uranium sample at 200 ^{o}C and P_i = 2050 mbar after different heat treatment temperatures.

reached when the gas filled the cell, which is a pressure drop of 312 mbar (311.67 mbar when the volume of the 1.8g sample is accounted for).

This was extended into an investigation into the hydride formation rate after a range of heat treatment temperatures, shown in figure 5.4. The percentages of total H_2 gas absorbed in figure 5.4 were found using:

$$(1 - (\frac{P - P_{min}}{P_{max} - P_{min}})) \times 100 \tag{5.2}$$

The range of the y-axis represents the pressure change between 1738.33 mbar (represented as 0 %) down to 1420 mbar (represented as 100 %). The pressure change between 2050 mbar and 1738.33 mbar does not describe the absorption of gas by the metal, merely the gas filling the reaction cell. The formation experiments performed here (again using the same 1.8g powdered metal uranium sample) showed a pressure drop to an equilibrium value of

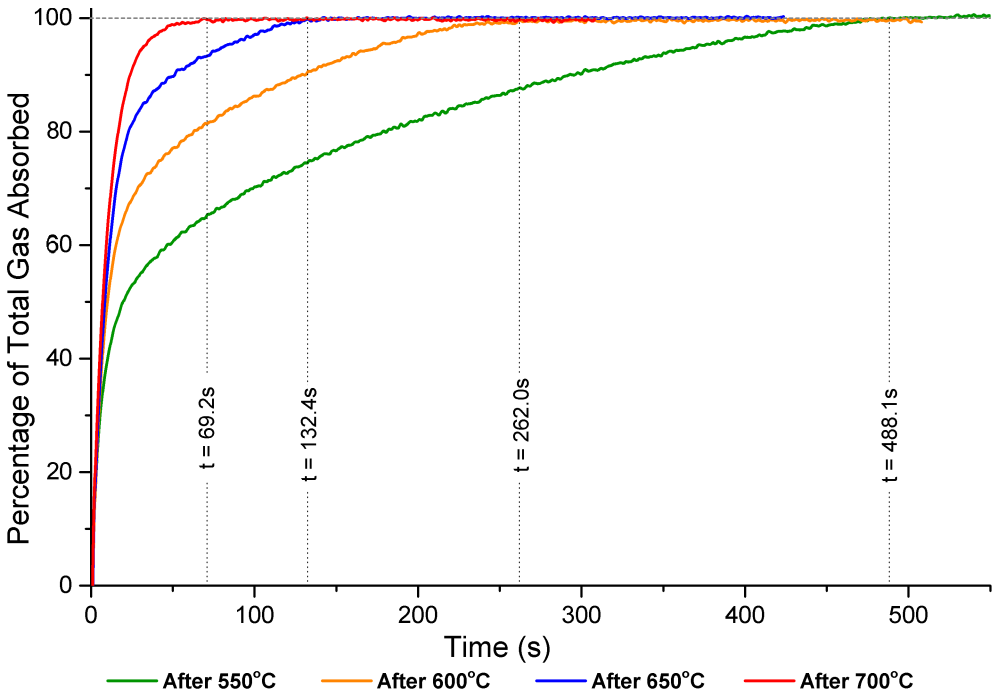

FIGURE 5.4: Graph showing percentages of H_2 gas absorption over time during UH_3 formation experiments after heat treatments of various temperatures, using a 1.8 g uranium sample.

1420 mbar, which is a pressure drop of 630 mbar. This indicates that the pressure drop from 2050 mbar to 1738.33 mbar is due to the cell filling with gas, and only the remaining the pressure change is actually due to the sample absorbing the gas because of UH_3 formation. This research is only concerned with the pressure drop due to absorption so only the data between 1738.33 mbar and 1420 mbar is included on the graph. The curve of the data between 2050 mbar and 1738.33 mbar is just a straight, vertical line.

5.2.1 Investigation via Pressure Change Curve Shape

The curves in the graphs in figures 5.3 and 5.4 appear to traverse a path (after the point P = 1738.33 mbar) that contains a quite sharp turning point. This gives the curves an appearance of being in two distinct sections: a section before the turning point and a section after the turning point. The difference in shape of the curves after different heat treatments seems to be: the turn

in the curve turns a sharper angle faster; and also the position of the turning point with relation to the y-axis. A higher heat treatment results in the turning point happening at a lower pressure (after more gas has been absorbed by the metal sample) and the curve makes a much faster change of direction. Then, after the turning point, each curve shows a very particular shape (representing a continuous decrease in gas pressure) until they each reach the same horizontal line (constant gas pressure).

In both figures 5.3 and 5.4 the curve representing 550 °C has a first section (before the turning point) that is quite a shallow angle from the vertical and a second section (after the turning point) that looks similar to a curve of the form x^2. This lead to speculation that the two sections could represent the induction period (hydrogen permeating through the metal lattice) and the bulk reaction period (the reaction front moving radially inwards into the grains, the "shrinking core") described in section 3.1.2. To investigate this some computer code was written in the programming language C# (shown in Appendix A) to produce a graph of the curve: radius of a sphere vs surface area of a sphere. This graph, shown in figure 5.5, could then be used for comparison with the shape of the second section of the 550 °C curves in figures 5.3 and 5.4.

The graph in figure 5.5 shows data produced from the C# code. The data shows the change in surface area of a sphere due to a reduction in its radius. The starting radius was set at 500nm, this is (approximately) the value that UH_3 particles have been shown to be after being powderised to their minimum size [87]. The code contains a loop that will iteratively calculate the surface area, print the data (radius and surface area) to a .csv file, reduce the radius by 5nm and then restart the loop.

The shape of the second section of the 550 °C curves in figures 5.3 and 5.4 do appear to be a shape that is related in some way to the changing surface area of the hydride-metal interface due to the 'shrinking core' nature of the

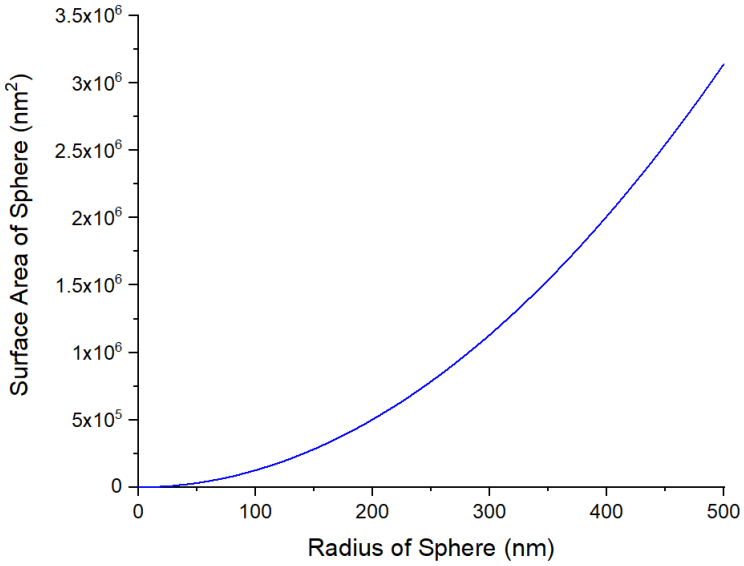

FIGURE 5.5: A graph of radius of a sphere vs surface area of a sphere between r = 0 - 500 nm. Data generated by code written in C#.

reaction front slowly moving inwards into the metal grains. The similarity between the shape of the curves in figure 5.4 and the curve of surface area vs radius in figure 5.5 becomes less and less apparent with increasing heat treatment temperature (the red curve in figure 5.4 looks more like the curve in figure 5.5 than the green curve does).

5.2.2 Investigating Carbon Poisoning in the Sample

As mentioned above, Rundle et al. (1948 [108]) claimed that a monoxide phase of uranium could only be formed in the presence of carbon. In order to investigate this claim the crucible used in the hydride formation & decomposition experiments (and also during the heat treatment process) was subjected to x-ray florescence (XRF) to find out if it contained carbon.

The data produced by the XRF scan of the crucible is shown in table 5.2. The XRF results show that the crucible is made of stainless steel 316, so carbon would have been present during the hydride formation & decomposition experiments and also during the heat treatment process. A new crucible was

Element	% Composition	% Error
Mo	2.491	0.002
Zr	0.003	0.001
Zn	0.015	0.001
W	0.05	0.002
Cu	0.35	0.004
Ni	11.633	0.014
Co	0.465	0.01
Fe	67.126	0.02
Mn	1.535	0.008
Cr	16.245	0.01
V	0.056	0.002
Nb	0.016	0.001
Bi	0.009	0.001
Ru	0.007	0.001
Alloy	SS-316	-

TABLE 5.2: Table showing XRF composition data of crucible.

FIGURE 5.6: The molybdenum crucible that was made for use on the gas rig

made out of molybdenum (shown in figure 5.6) to see if the new compound was present in the depleted uranium when the heat treatment at 700 °C was performed in a crucible made from a material that didn't contain carbon.

2.4g of depleted uranium powder was inserted into the molybdenum crucible and reaction cell and attached to the gas rig. A hydride formation-decomposition cycle was performed on the metal before the heat treatment, the hydride formation conditions were T = 200°C and P_{H2} = 1000 mbar and the hydride decomposition conditions were T = 500°C and P_{H2} = 0 mbar. The sample (in the molybdenum crucible) was then heat treated at 700°C for

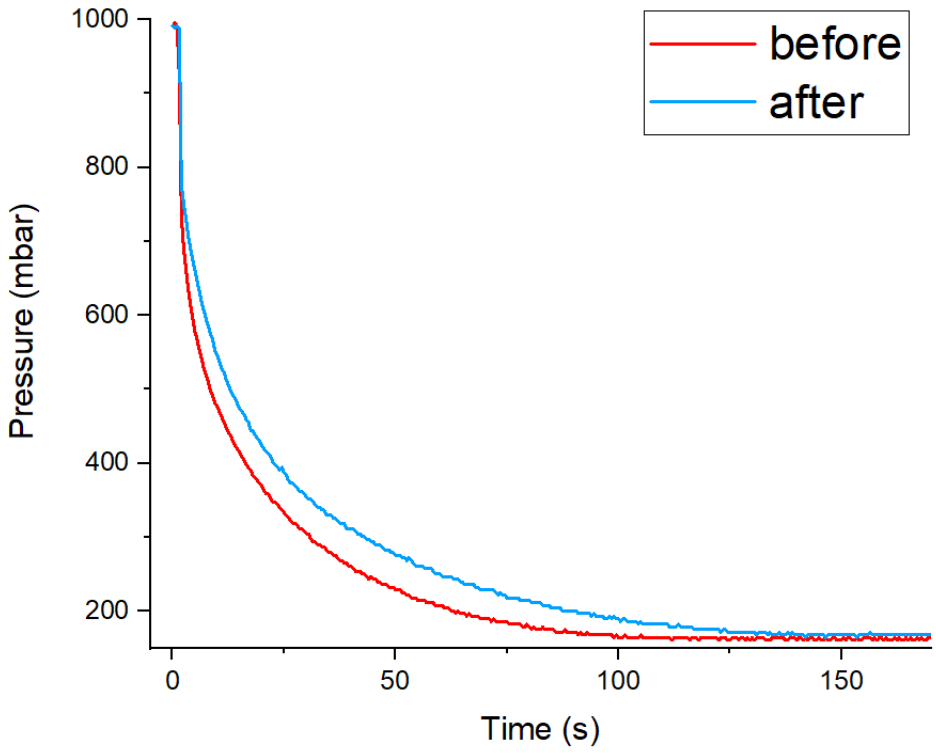

FIGURE 5.7: UH_3 formation in a molybdenum cell before and after heat treatment for 1 hour at 700°C.

1 hour under rough-pump conditions ($P \approx 10^{-3}$mbar). After the heat treatment an identical hydride formation-decomposition cycle was performed to show any change in gas absorption/desorption rate. The pressure change data for the UH_3 formation experiments (before and after heat treatment) are shown in figure 5.7 and the data for the 2 UH_3 decomposition experiments is shown in figure 5.8.

The increase in H_2 gas uptake rate after heat treatment in the steel crucible was not reproduced in the data when the sample was heat treated in the molybdenum crucible. In fact, both figures 5.7 and 5.8 appear to show that the absorption and desorption was slightly faster before the heat treatment than after. This could be due to that sample being exposed to a small amount of oxygen and the increased propensity for uranium metal to form UO_2 at higher temperatures, which might lessen the capacity of the metal to accommodate hydrogen and also slow down the reaction kinetics.

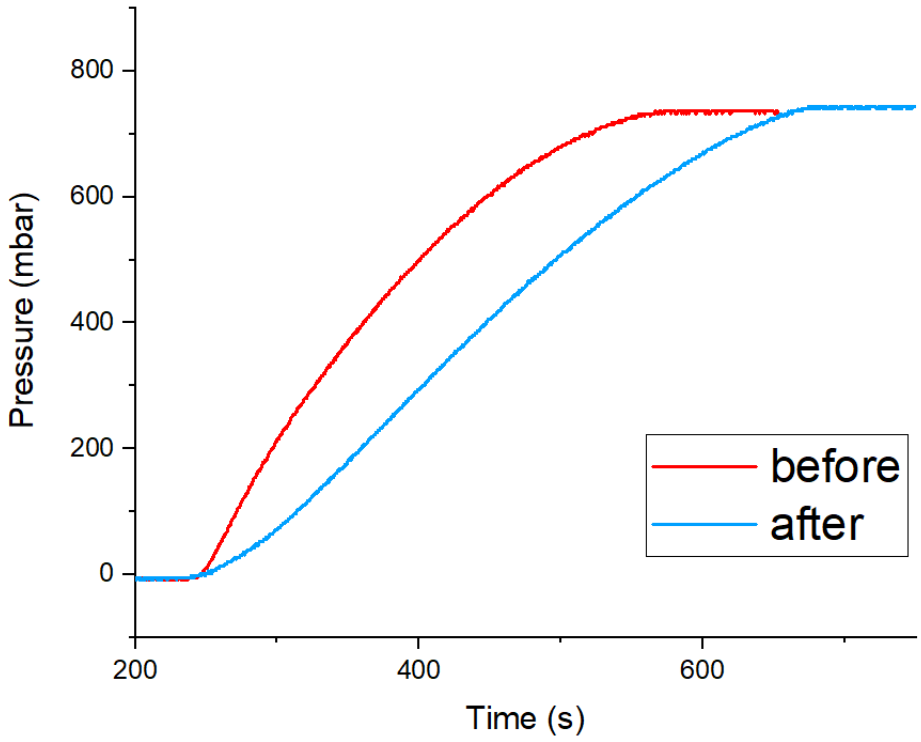

FIGURE 5.8: UH_3 decomposition in a molybdenum cell before and after heat treatment for 1 hour at 700°C.

X-ray diffraction was also performed on the uranium metal powder before and after heat treatment in the molybdenum crucible to see if the same diffraction peaks are produced as when the heat treatment was performed in a steel crucible. The data from the XRD scan both before and after the heat treatment are shown in figure 5.9.

X-ray diffraction data of the uranium metal that was heat treated in the molybdenum crucible did not show the same peaks (at 2θ = 31.63°±0.03°, 36.65°±0.03°, 52.88°±0.03°, 62.95°±0.03° and 66.15°±0.03°) as the sample heat treated in the steel crucible.

These results are in-line with the claim of Rundle et al. [64] that the presence of carbon is required to form the monoxide phase of uranium.

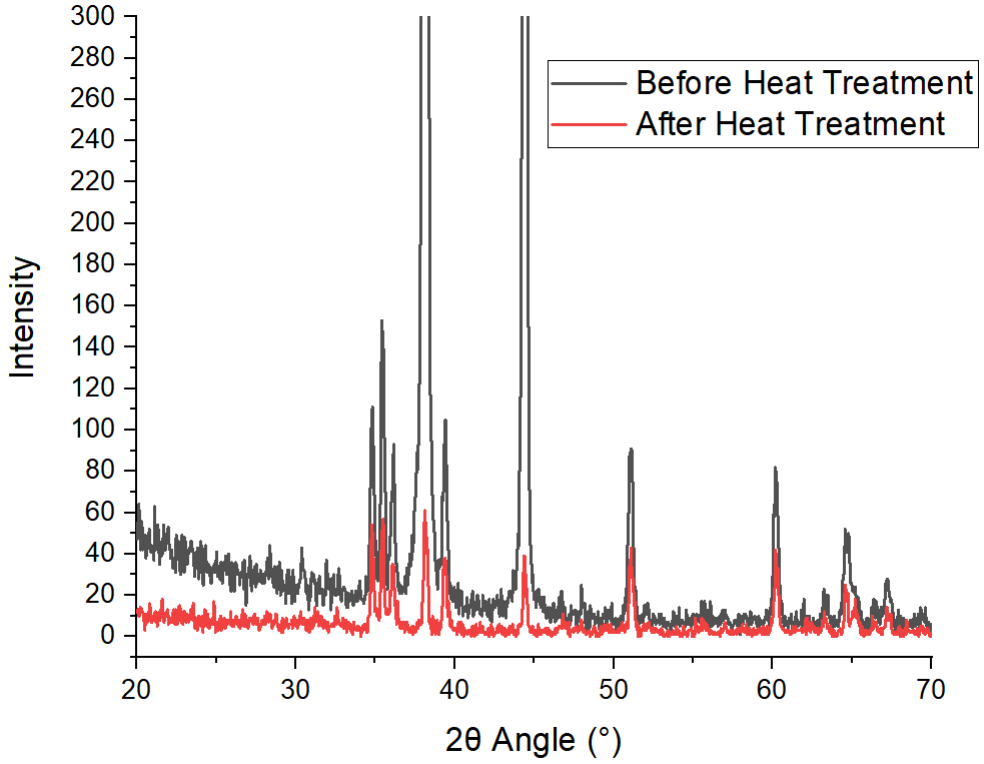

FIGURE 5.9: XRD scan of uranium metal before & after heat treatment in molybdenum cell

5.2.3 Investigation via X-ray Diffraction (XRD)

The effect of increasing the uptake rate of hydrogen by uranium after heat treating was investigated using XRD to identify any compositional change that may be happening as a result of the heat treatment. X-ray powder diffraction was performed on the powdered uranium metal before being heat treated at 700 °C and then again afterwards.

In order to perform these measurements, first a method of transporting the sample and installing it into the XRD machine without exposure to air was required to avoid changing the chemical composition of the sample.

Airtight Beryllium Cell

For performing XRD analysis on metal samples (which must remain sealed in a passive, air-tight environment), an airtight, purpose-built cell was designed and made out of a beryllium dome and an aluminium base (see figure 5.10). A pre-made beryllium dome constitutes the walls of the cell to allow

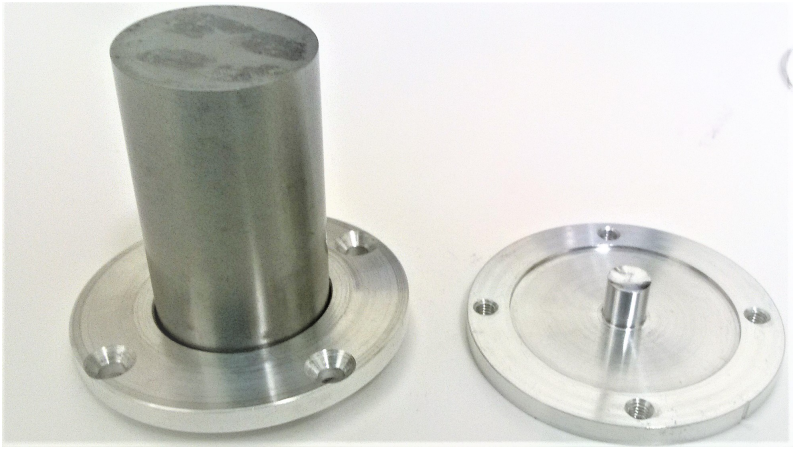

FIGURE 5.10: Photograph of custom made air-tight beryllium cell for performing X-ray Diffraction on samples which are sensitive to air. The cell is made up of a beryllium dome and a seal-able aluminium base.

the x-rays access to the powdered metal sample. The beryllium dome has a protruding lip at the bottom (its a top hat shape) which is clamped between the upper and lower half of a bespoke-made aluminium base, held together by tiny screws. A circle of 1mm indium wire is placed underneath the protruding beryllium lip (in a groove inside the bottom half of the aluminium base) to create an air-tight seal between the beryllium and the aluminium base. The lower half of the base has a vertical stub in the centre which is hollowed out into a bowl shape at the top to hold the powdered metal sample.

Beryllium metal was chosen to be used for the walls of the cell because it has a low proton number ($Z = 4$) and so has little interaction with the x-rays. Aluminium was chosen as the material that the base was made of because most of its diffraction peaks lie outside the range of angles used to characterise uranium (and its hydrides and oxides). When half-cutting the x-ray

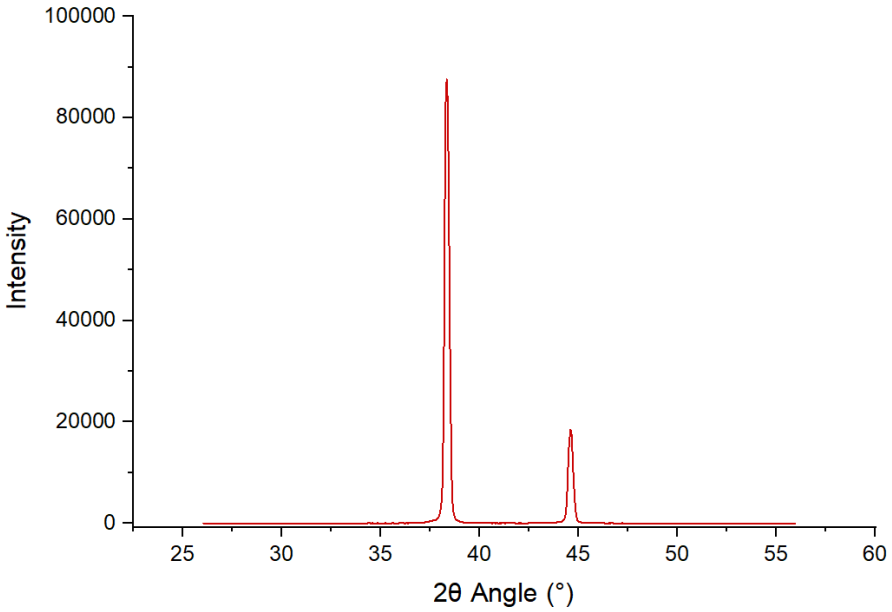

FIGURE 5.11: XRD scan between 26° - 56° of the beryllium dome with no sample, for calibration. The two peaks that can be seen at 38° and 44° are from the Aluminium base.

.

beam, it was found that the beryllium dome reduced the x-ray intensity that was detected by the XRD machine to almost exactly two-thirds of that detected without the beryllium dome.

The entire cell (the beryllium dome and aluminium base when clamped together) was measured to be 41 mm in height with a diameter of 44 mm at its base. The main body of the beryllium dome has an external diameter of 22.5 mm and an internal diameter of 21.5 mm, making the thickness of the beryllium walls 0.5 mm. Each of the halves of the aluminium base was measured to be 4 mm in height, and the stub in the centre (with the bowl at the top) was measured to be 9 mm in height and 6 mm in diameter. The bowl was designed to be this height so that it holds the sample no more than 10 mm above the aluminium base, so that the sample is at the correct height to initially calibrate the XRD machine by *half-cutting* the horizontal x-ray beam.

In order to investigate any compositional change that may be happening as a result of the heat treatment, x-ray powder diffraction was performed on the powdered uranium metal before being heat treated at 700 °C and then

again afterwards.

All x-ray diffraction scans were performed using the same instrument settings. The angular size of each incremental step that the instrument's x-ray emitter/detector moved through was: 0.05 °, the duration of each step was 4 seconds.

An XRD scan of the empty beryllium cell was performed for calibration purposes (see figure 5.11).

The graph of the XRD scan of the uranium metal before the heat treatment is shown in figure 5.12 and the graph of the XRD scan of the metal after the heat treatment is shown in figure 5.13 (and figure 5.14 shows both for easy comparison). All visible x-ray peaks are labeled with their 2θ angle, their metal/compound and the Miller indices (*hkl*) of the lattice plane that correspond to the peaks. All the peaks were identified using data from *The National Chemical Database*.

The two aluminium peaks at 2θ=38.33°±0.03° and 2θ=44.58°±0.03° are due to the aluminium bowl that is holding the powder, as described above. Both sets of XRD data show some peaks which were unexpected, namely, the peaks at 2θ = 31.63°±0.03°, 36.65°±0.03°, 52.88°±0.03°, 62.95°±0.03° and 66.15°±0.03°. Diffraction peaks at the same 2θ angles as these were identified in the published literature: Rundle et al. (1948 [108]) claimed that the peaks are caused by the rare compound uranium monoxide (*UO*). The peaks have been labelled as such on the graphs.

The Rundle et al. paper describes uranium monoxide as having a face-centered cubic (sodium chloride-type) crystal structure, with $a = 4.92 \pm 0.02$ Å. They discovered the monoxide during attempts to make X-ray diagrams of uranium metal in the beta and gamma temperature ranges (660–760 °C [109]). It is also claimed that the presence of carbon is necessary to promote the reaction of a higher oxide with uranium metal to form the monoxide phase.

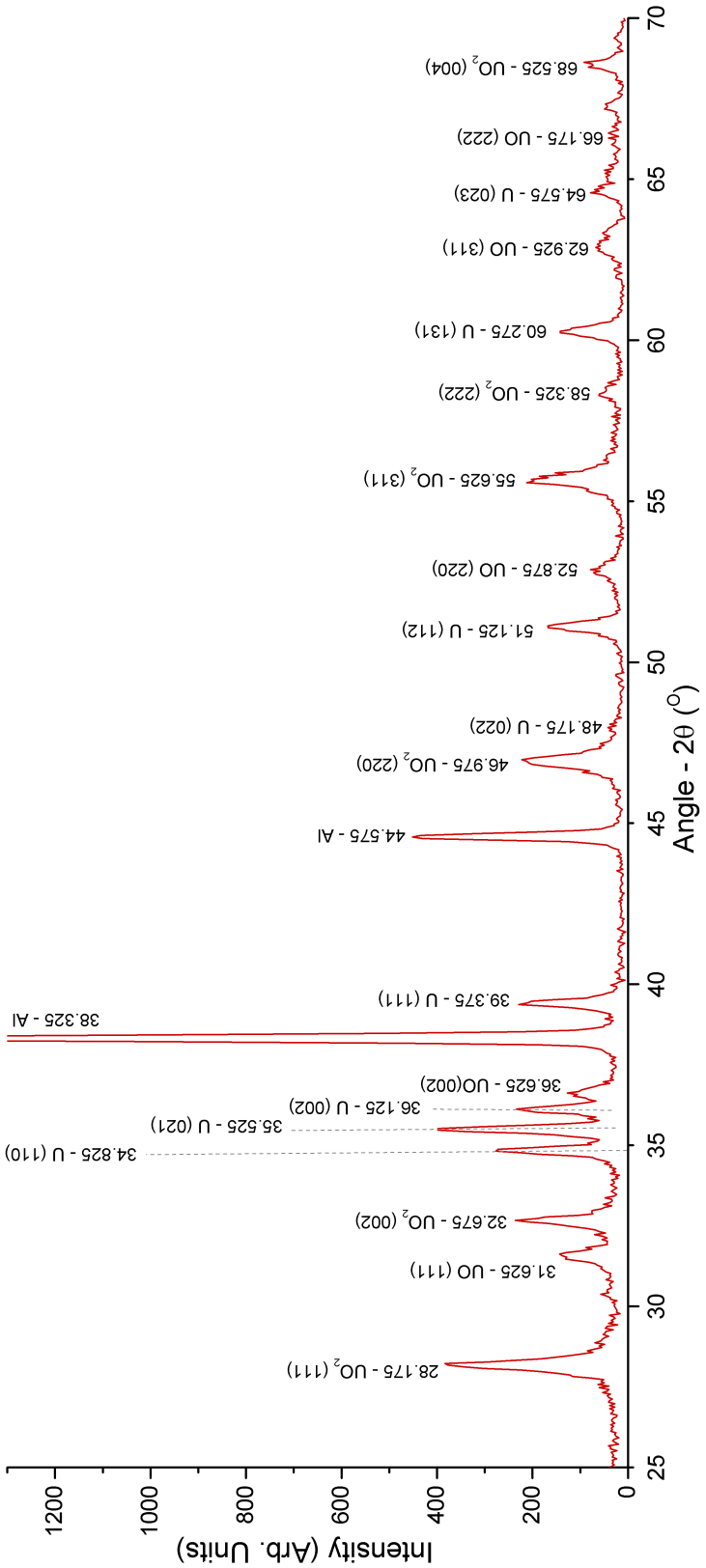

FIGURE 5.12: X-ray diffraction pattern of uranium metal powder before being heat treated at 700 ^{o}C. X-ray peaks are labeled with their 2θ angle, their metal/compound and the Miller indices (*hkl*) of the lattice plane that correspond to the peaks.

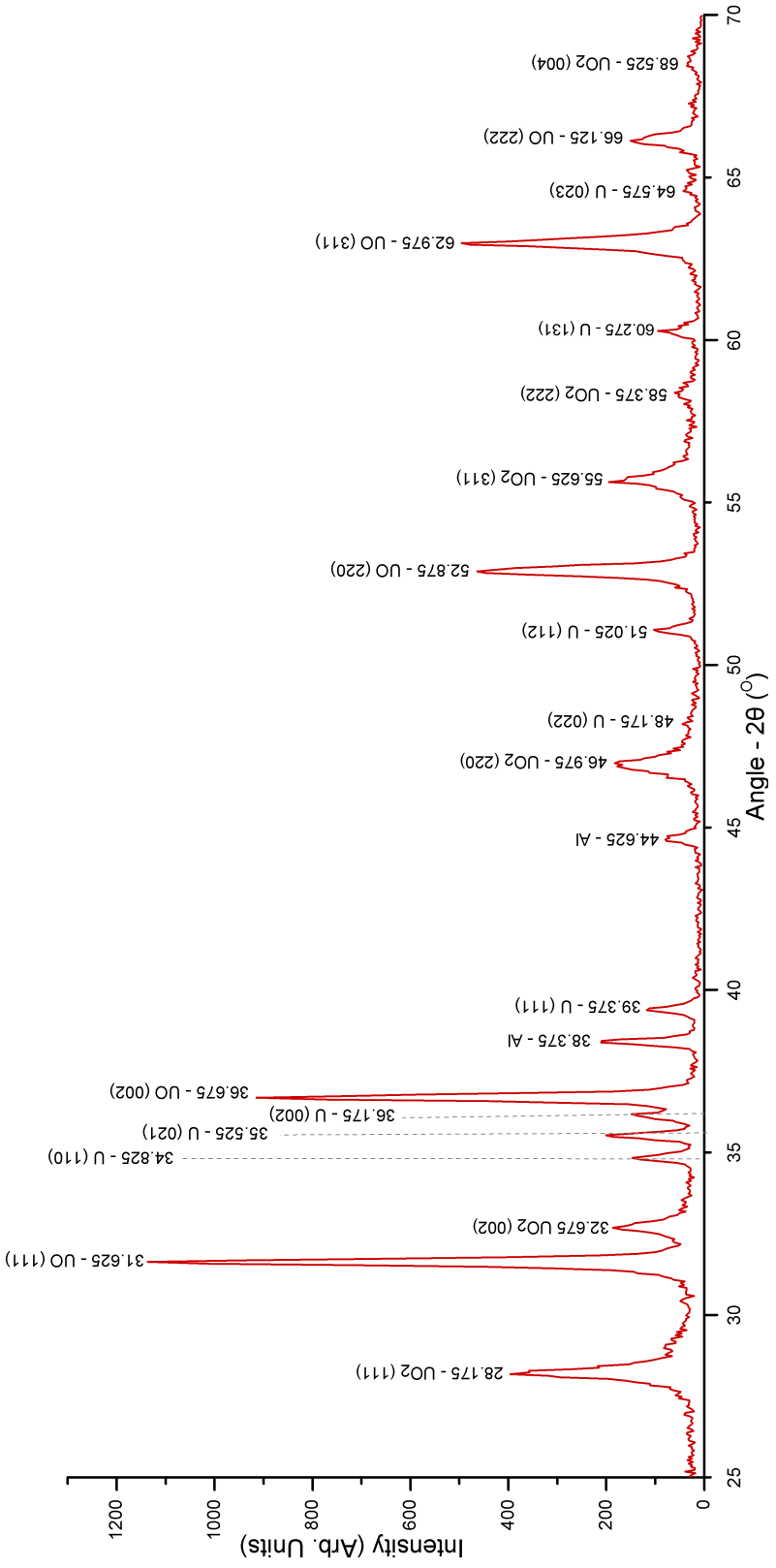

FIGURE 5.13: X-ray diffraction pattern of uranium metal powder after being heat treated at 700 ^{o}C. X-ray peaks are labeled with their 2θ angle, their metal/compound and the Miller indices (*hkl*) of the lattice plane that correspond to the peaks.

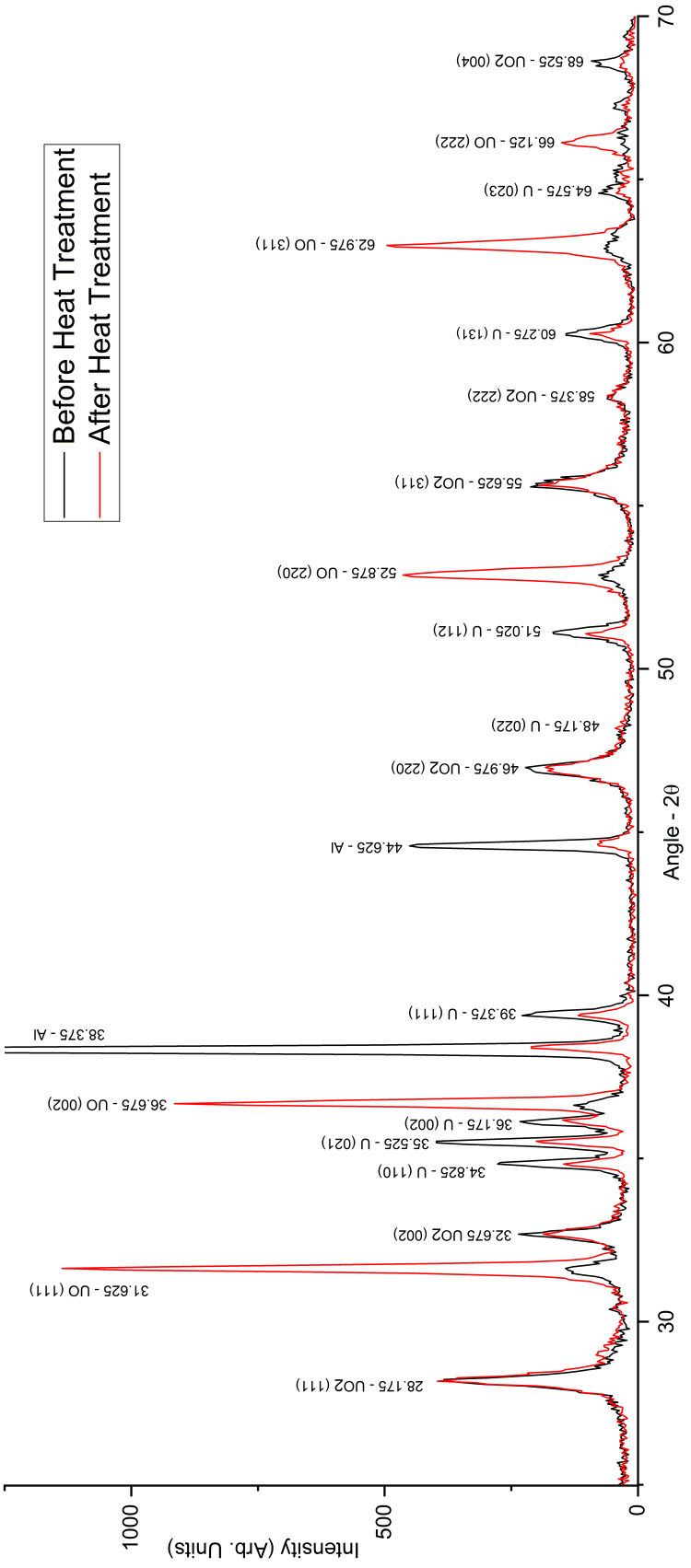

FIGURE 5.14: X-ray diffraction pattern of uranium metal powder before being heat treated at 700 ^{o}C and afterwards. X-ray peaks are labeled with their 2θ angle, their metal/compound and the Miller indices (*hkl*) of the lattice plane that correspond to the peaks.

From the 2θ positions of the XRD peaks, the Miller indices quoted by Rundle et al. and the equations:

$$d = \frac{\lambda}{2sin\theta} \tag{5.3}$$

$$a = d\sqrt{(h^2 + k^2 + l^2)} \tag{5.4}$$

The lattice parameters and lattice plane spacings of the material causing the unidentified peaks were calculated (by approximating λ as the wavelength of the x-rays emitted by the XRD machine in § 4.3.6: λ = 1.54 Å) as:

2θ (°)	hkl	d (Å)	a (Å)
31.625	111	2.827 ± 0.162	4.896 ± 0.281
36.675	002	2.448 ± 0.120	4.897 ± 0.240
52.875	220	1.730 ± 0.056	4.893 ± 0.160
62.975	311	1.475 ± 0.039	4.891 ± 0.130
66.125	222	1.412 ± 0.035	4.891 ± 0.122

TABLE 5.3: The calculations of lattice spacing and cell parameters for the XRD peaks labelled *UO*.

Though all of the calculated values for lattice parameter (a) in table 5.3 are slightly outside of the error margin of the value quoted by Rundle et al., they are considered to be equivalent values due to an overlap in the error margins between the value quoted by Rundle et al. and the calculated values.

To investigate this further an XRD scan (identical to the one above) of the powdered sample containing (what is now being called) UO after it had been exposed to hydrogen gas in the gas rig at 200 °C. The results of the scan are shown in figure 5.15 and, for comparison, the curves of the XRD data for the UO sample and UO + H_2 are plotted together in figure 5.16.

The most noticeable thing when comparing the peaks of the two curves in figure 5.16 is that the hydriding process has caused the peaks that are now being called UO to reduce in intensity.

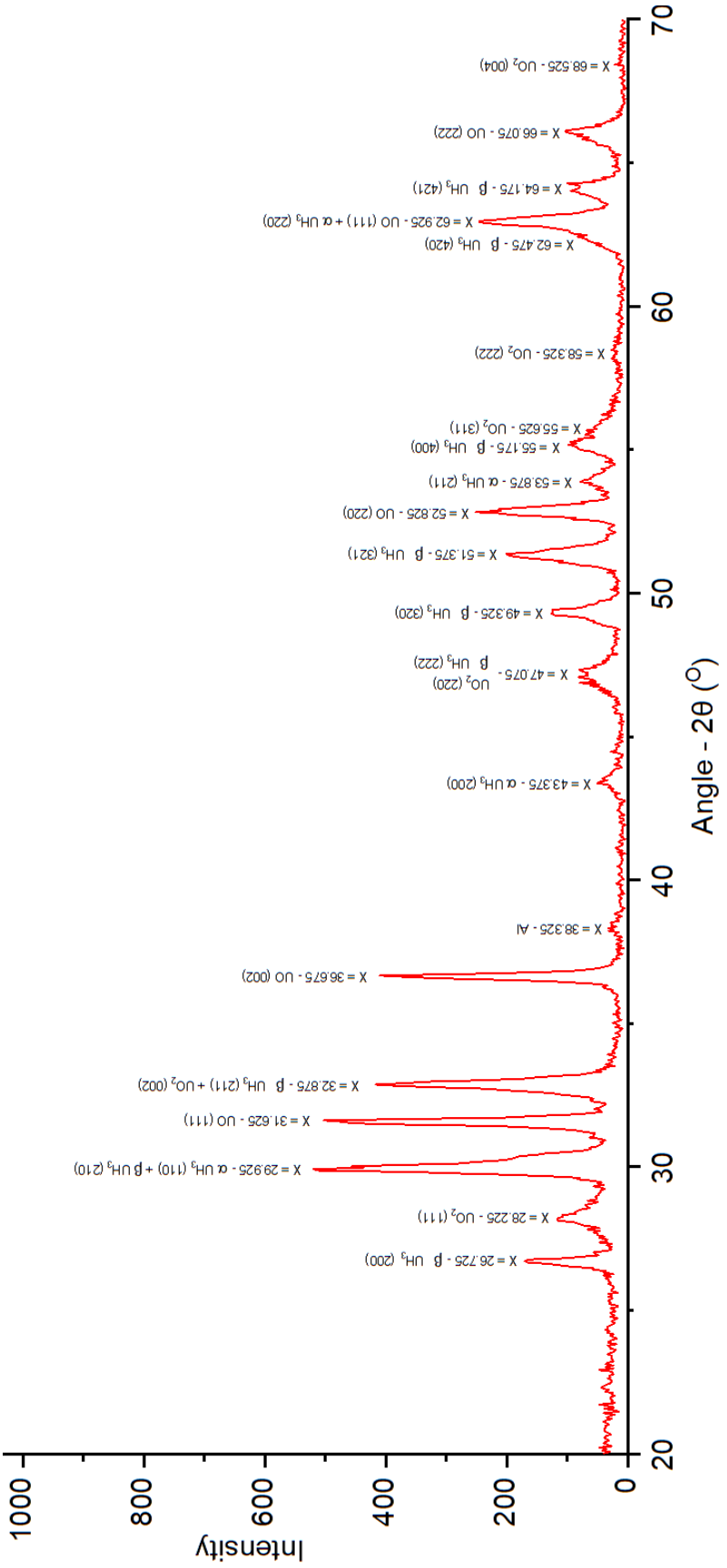

FIGURE 5.15: XRD scan of heat treated metal after reaction with H_2 gas with peak identification labels.

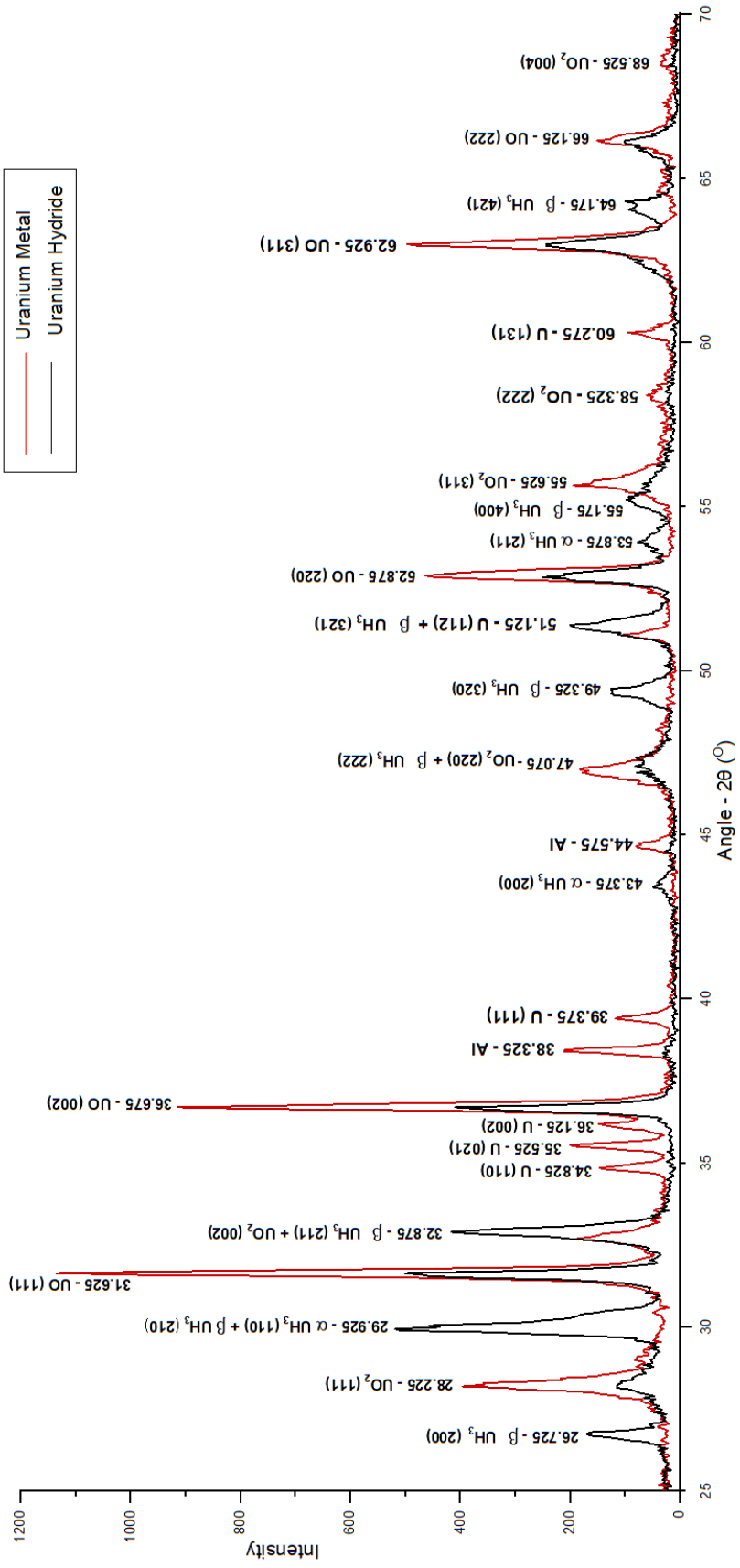

FIGURE 5.16: Comparison of the X-ray diffraction patterns of uranium metal that has been heat treated at 700 ^{o}C (red line) and the X-ray diffraction patterns of the same metal after hydride formation (black line).

This suggests that the compound in question, represented by these peaks, has reacted with the hydrogen and converted into a hydride.

5.2.4 Investigation via Crystallite Size & Microstrain

XRD Peak Fitting

The function that was used for peak fitting of the XRD data of the uranium metal before and after the heat treatment at 700 °C (figures 5.12 and 5.13) was performed using *Origin Lab 9.0*. The peak fitting function called PsdVoigt1 was used (see § 4.3.7). It was decided that, after checking other curve fitting functions, this function gave the best fit on the uranium peaks that were required, and it gave the best calculation of the background signal for the XRD data presented in § 5.

The full range of the data of the two XRD scans were split into two sections. This was done for two reasons, firstly because the background signal appeared to be slightly different in the two sections of the data, and so splitting the data in two gave a better calculation of the background across the entire range of the XRD data. The second reason that the data was split in two was in order to exclude the aluminium peak at $2\theta = 38.375\,^{\circ}$, which was effecting the fitting of the curve across all the other peaks.

After the curve was fitted to the XRD data that had been split in half, with the aluminium peak was excluded, a much better fitting to the background and to all the other peaks across the entire range of the data was achieved.

The settings of the fitting function were set so that the curve fitting was iterated until the value of chi-squared that must be achieved was:

$$\chi^2 = 1 \cdot 10^{-9} \tag{5.5}$$

Before the 700 °C Heat Treatment

The curve fitting to the peaks of the XRD data of the uranium metal before the 700 °C heat treatment is shown in figure 5.17.

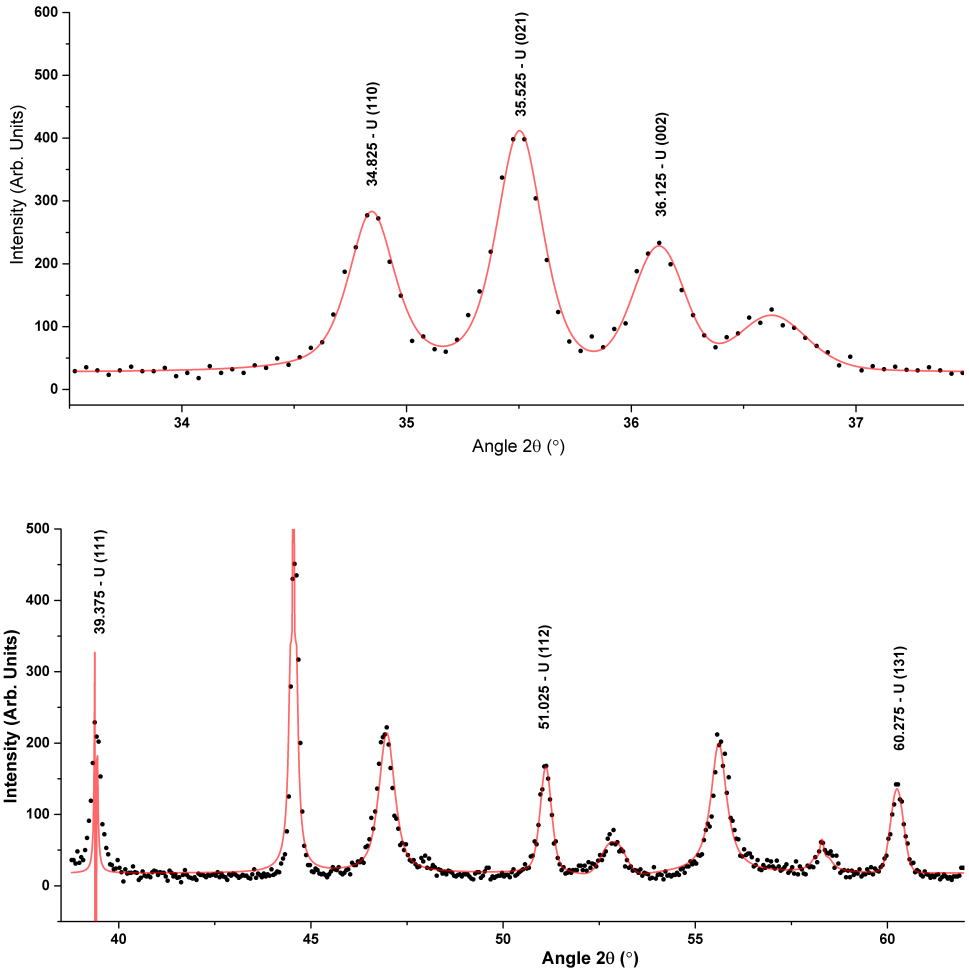

FIGURE 5.17: Fitting curves of the XRD peaks of the uranium metal powder before being heat treated to 700 ^{o}C.
Top: 33.5 ^{o} - 37.5 ^{o}, bottom: 38.5 ^{o} - 62.0 ^{o}

The fitting of the the U (111) peak at $2\theta = 39.375^{\circ}$ appeared to have gone wrong. It looks like *Origin Lab 9.0* has tried to fit two curves to the peak, it could be because the Voigt function is a convolution of a Gaussian and a Lorentzian. It was isolated and fitted individually (in figure 5.18). This was done to try and achieve as accurate a result as possible for the values produced using the William-Hall method.

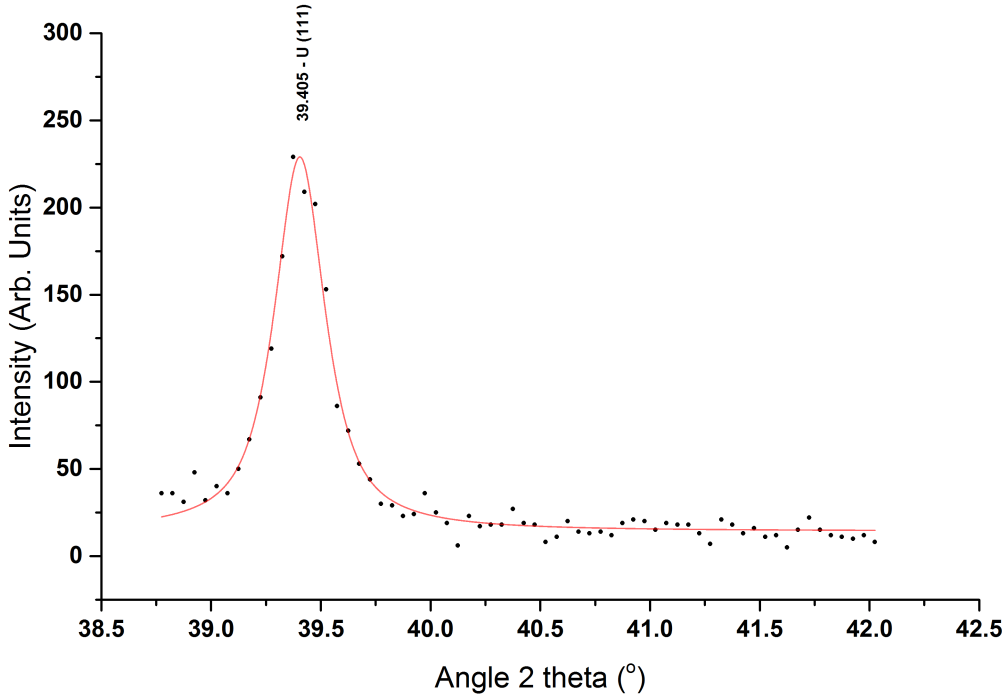

FIGURE 5.18: Refit of the curve to the (111) XRD peak of uranium metal powder before heat treatment to 700 ^{o}C.

After the 700 °C Heat Treatment

The curve fitting to the peaks of the XRD data of the uranium metal after the 700 °C heat treatment is shown in figure 5.19.

The fitting of the peak at the angle $2\theta = 36.175°$, which is the U (002) peak, also appeared to be fitted badly and so it was also excluded from the calculations in the Williamson-Hall method graph in figure 5.21.

The Scherrer Equation

The Scherrer Equation is an equation that characterises a technique for calculating the size of crystallites (grains) in a powder sample from the *Full Width Half Maximum* of x-ray diffraction peaks [110].

A grain is a region in a crystal where the lattice structure is continuous and unbroken; a microscopic monocrystal which has grain boundaries with

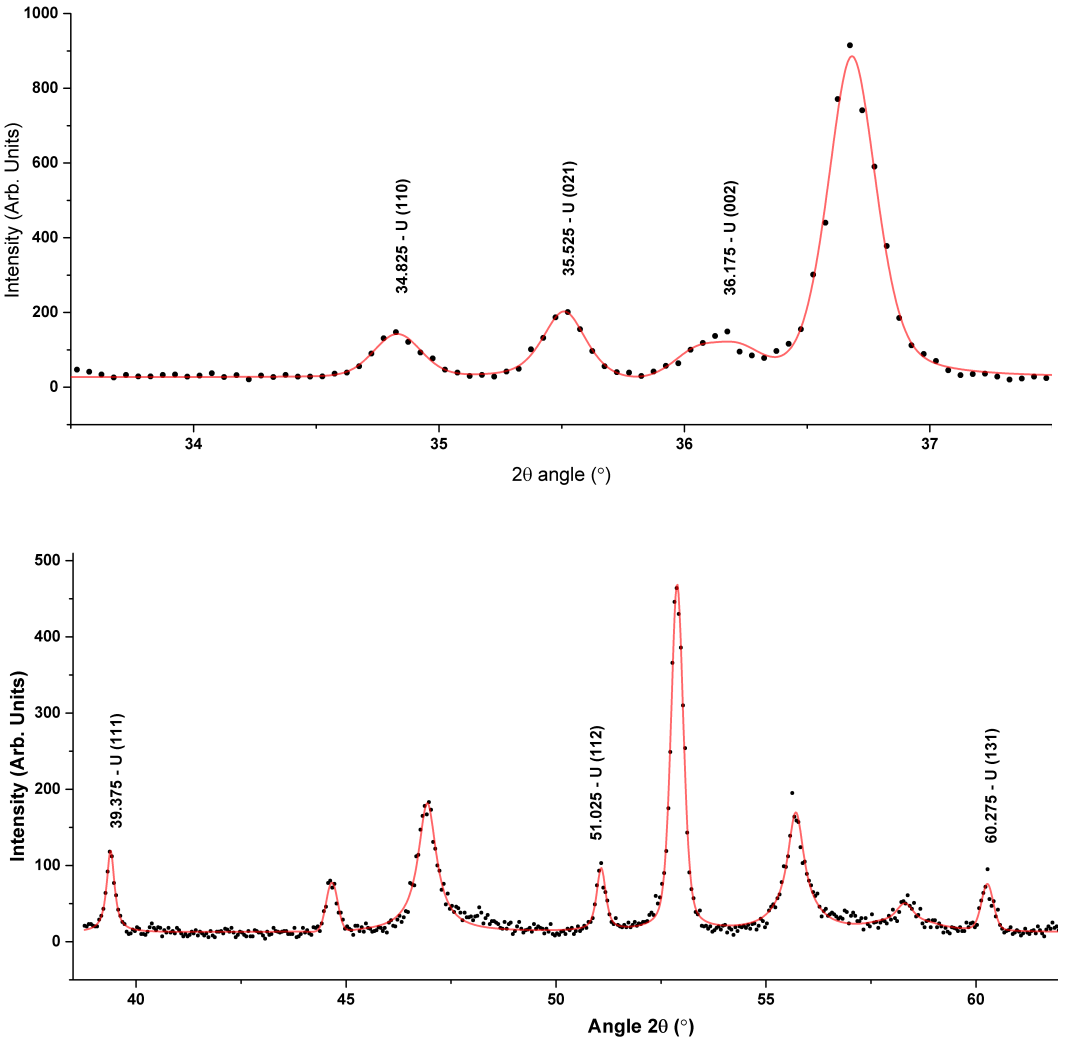

FIGURE 5.19: Fitting curves of the XRD peaks of the uranium metal powder after being heat treated to 700 ^{o}C. Top: 33.5^{o} - 37.5^{o}, bottom: 38.5^{o} - 62.0^{o}

other monocrystals, oriented in different directions.

The Scherrer equation (equation 5.6) can be used to calculate a lower bound on the mean value of the size of the grain.

$$\tau = \frac{K\lambda}{\beta \cos\theta} \tag{5.6}$$

where τ is the mean size of the crystallite, K is a dimensionless shape factor with the value 0.94 (when approximating the grain's shape as spherical [111]), λ is the x-ray wavelength, β is the FWHM and θ is the Bragg angle.

2θ angle (°)	(*hkl*)	size before (Å)	size after (Å)	size change (Å)
35.503	(021)	358 ± 1	415 ± 2	57 ± 2
39.405	(111)	318 ± 2	395 ± 2	77 ± 3
51.113	(112)	262 ± 5	356 ± 2	94 ± 5
60.249	(131)	244 ± 5	288 ± 2	44 ± 5

TABLE 5.4: Table of the change in crystallite size due to heat treatment at 700 ^{o}C, calculated using the Scherrer equation.

The calculations in the size of the crystallites in the UO sample before and after heat treatment at 700 ^{o}C, using the Scherrer equation (equation 5.6), are shown in table 5.4. All of the calculations for the size of the four crystallites chosen show an increase in size after the heat treatment. These results support a proposition that the change in reaction rate is connected to a change in the size of the grains of the metal powder.

It has been shown so far that the heat treatment at 700 °C has either caused or is linked with: an increase in grain size in the metal; a change in the molecular composition of the sample; and an increase in the reaction rate of one of the stages of the hydride reaction.

The Williamson-Hall Method

The Williamson-Hall method is a technique for calculating and separating the factors that contribute to XRD peak broadening. The broadening of an XRD peak (β_{total}) is made up of two main elements. The first is strain broadening (β_{strain}), micro-strain in the crystal lattice caused by e.g. deformations and dislocations. The second is size broadening (β_{size}), from the increase in size of the crystallites and the sub-micron nanoparticles of the metal [112]. This can be described mathematically as:

$$\beta_{total} = \beta_{strain} + \beta_{size} \tag{5.7}$$

Equation 5.6 can be substituted for the size broadening term, switching the symbol τ for L (mean crystallite size), gives:

$$\beta_{size} = \frac{K\lambda}{L\cos\theta} \tag{5.8}$$

The term for strain broadening can be found by differentiating the equation for the Bragg Condition 4.1, substituting gives:

$$\beta_{strain} = 2\,\mathcal{E}\,tan\theta \tag{5.9}$$

Strain is generally defined as the change in an objects length divided by its original length, so here, when considering microstrain, lattice parameter is used in place of length:

$$\mathcal{E} = \frac{\Delta a}{a} \tag{5.10}$$

Substituting equations 5.8 and 5.9 into equation 5.7 gives:

$$\beta_{total} = \beta_{strain} + \beta_{size} = 2\,\mathcal{E}\,tan\theta + \frac{K\lambda}{L\cos\theta} \tag{5.11}$$

Rearranging equation 5.11 to give an equation of the straight-line form gives:

$$\beta\cos\theta = 2\,\mathcal{E}\,sin\theta + \frac{K\lambda}{L} \tag{5.12}$$

Equation 5.12 can then be plotted as the graph: $\beta\cos\theta$ vs. $sin\theta$ which gives a gradient of $2\,\mathcal{E}$ and a y intercept of $\frac{K\lambda}{L}$. The values of β can be calculated using the equation for the Gaussian function. This can be rearranged to give:

$$\beta = \frac{FWHM}{2} \cdot \sqrt{\frac{\pi}{ln(2)}} \tag{5.13}$$

The Williamson-Hall method was used to calculate the grain size and the

micro-strain for XRD peaks of both the powdered uranium metal sample before the heat treatment at 700 °C (in figure 5.12) and the sample after the heat treatment (in figure 5.13). This gave a way of comparing the values for both grain size and lattice strain of the metal before and after heat treatment.

The peak fitting in this subsection was again performed using the Psd-Voigt1 function of *Origin Lab 9.0* in an identical way to § 5.2.4, and as described in § 5.2.4.

This new data was plotted into a graph, shown in the Williamson-Hall plot in figure 5.20 for the metal powder before heat-treatment at 700 °C and figure 5.21 for the metal powder after heat-treatment at 700 °C.

The Williamson-Hall plot in figure 5.20 shows six data points corresponding to six XRD peaks (those that could be fitted with a curve well enough to find their FWHM). All data points lie close enough to the straight trend-line that it is within their error margins. The equation of the trend-line is:

$$y = (11.28 \pm 2.00) \cdot 10^{-3} \cdot x + (0.97 \pm 0.60) \cdot 10^{-3} \tag{5.14}$$

and the 'goodness of fit' parameter (calculated by *Origin*) is: $R^2 = 0.89$.
This gives a value for micro-strain from the gradient as:

$\mathcal{E} = (5.64 \pm 1.00) \cdot 10^{-3} = (0.56 \pm 0.10)\,\%$

and a value for grain size from the y intercept as:

$L = (1492 \pm 923)$ Å

The Williamson-Hall plot in figure 5.21 shows data points corresponding to five of the XRD peaks (the (002) peak wasn't usable after heat treatment due to the height change in a nearby UO_1 peak). These all sit close enough to the trend-line so that it is, again, within their margins of error. The equation of the trend-line is:

$$y = (6.54 \pm 2.00) \cdot 10^{-3} \cdot x + (1.76 \pm 0.60) \cdot 10^{-3} \tag{5.15}$$

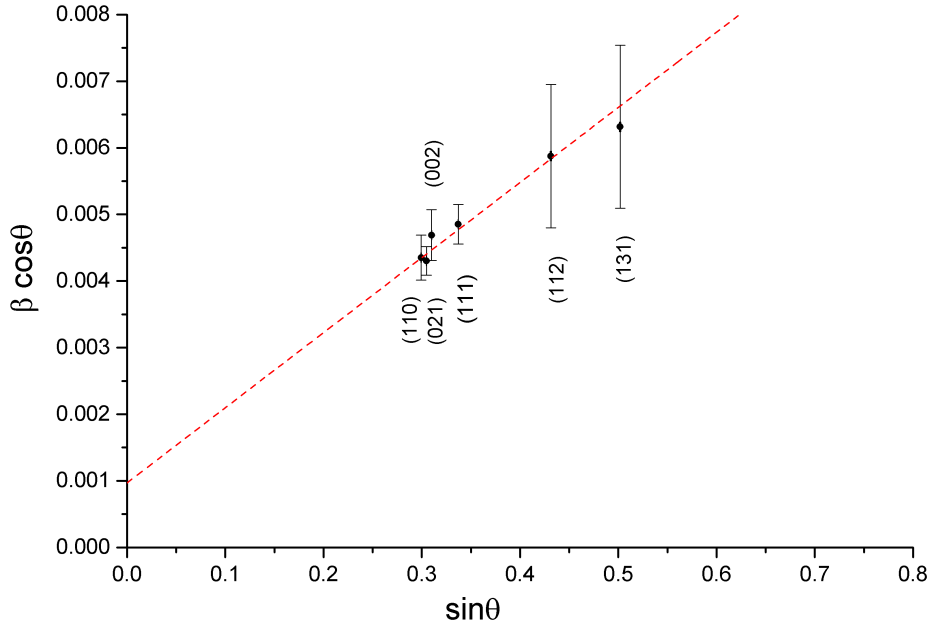

FIGURE 5.20: Graph showing the Williamson-Hall method for the uranium metal sample before heat treatment at 700 °C. Each data point is marked with the Miller indices (*hkl*) of the lattice plane that corresponds to that peak. The equation of the trend-line is $y = (11.28 \pm 2.00) \cdot 10^{-3} \cdot x + (0.97 \pm 0.60) \cdot 10^{-3}$ and the 'goodness of fit' parameter is $R^2 = 0.89$, both of which were calculated by *Origin Lab 9.0*.

and the 'goodness of fit' parameter (calculated by *Origin*) is: $R^2 = 0.84$.

This gives a value for micro-strain from the gradient of the trend-line as:

$$\mathcal{E} = (3.27 \pm 1.00) \cdot 10^{-3} = (0.33 \pm 0.10)\,\%$$

and the value of grain size from the y intercept as:

$$L = (823 \pm 300)\ \text{Å}$$

The values for both grain size and lattice strain show a change after the 700 °C heat treatment, according to these results. After the heat treatment the value for lattice strain had decreased to $\approx 58\%$ of its value before the heat treatment. The change is large enough so that there is no overlap of the error margins of the two values (before and after the heat treatment).

The values for grain size produced using this method did show a decrease after the heat treatment, to $\approx 55\%$ of its value before the heat treatment. The margin of error (calculated using the partial differentiation method) is very large in comparison to the values. The error margin before heat-treating was

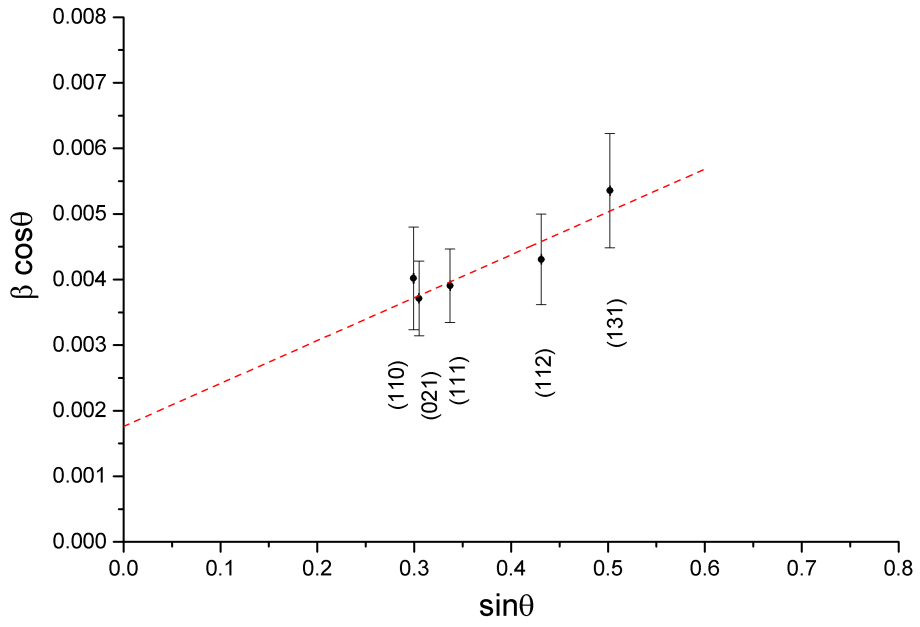

FIGURE 5.21: Graph showing the Williamson-Hall method for the uranium metal sample after heat treatment at 700 °C. Each data point is marked with the Miller indices (*hkl*) of the lattice plane that corresponds to that peak. The equation of the trend-line is $y = (6.54 \pm 2.00) \cdot 10^{-3} \cdot x + (1.76 \pm 0.60) \cdot 10^{-3}$ and the 'goodness of fit' parameter is $R^2 = 0.84$, both of which were calculated by *Origin Lab 9.0*.

$\approx 62\%$ of the grain size value, after the heat treatment it was $\approx 36\%$ of the value. The size of the error margins in these results is concerning. Each value's error margin would have been indirectly determined by the fit of the trend-line to the data points in figures 5.20 and 5.21 and the uncertainty of the FWHM of the XRD peaks. When the grain sizes were calculated by the Scherrer equation in § 5.2.4, using the same XRD data and the same FWHM values from the fitting shown above, all four calculated grain sizes showed an increase in size. The values for grain size that have been produced in this research so far are inconsistent.

It could be that some of the grains are increasing in size during the heat treatment whilst some (that were not observed in this work) are decreasing in size, which is a known phenomenon [113]. This would produce a sample comprised of grains of different sizes, called a *duplex grain structure*. It

has been found that heat-treating uranium metal at temperatures above uranium's $\alpha \rightarrow \beta$ phase change temperature (663 °C) causes the sample to form a duplex grain structure [56]. It is unlikely that this is the reason for the difference in the results here, though, because the results from both methods were calculated using (mostly) the same XRD peaks.

The Williamson-Hall method treats the grains as being all the same shape, an *equiaxed* grain structure, when, in reality, it is more likely that they are very different shapes. The orthorhombic unit cell of α-phase uranium transforms into the tetragonal β-phase when heated to the phase change temperature of 663 °C. This is an anisotropic expansion of the unit cell, there could also be some anisotropic effects on the size or shape of the grains in the metal, just as in the unit cell. This could be one possible explanation for the difference between these results and those in section § 5.2.4.

5.2.5 Hydride Formation Inside the XRD Machine

To build up a better picture of the structural changes that are taking place within the sample at different heat treating temperatures (i.e. at which temperature of heat treatment, exactly, is it that this new compound is forming?) XRD scans would be needed after each heat treatment temperature. To do this the sample would need to be taken off the gas rig after each heat treatment, transferred into the beryllium cell, put into the x-ray diffractometer, scanned, then reinserted into a reaction cell and attached back onto the gas rig. This would involve a much higher risk of oxidisation of the sample. Therefore, a method of forming and decomposing UH_3 inside the x-ray diffractometer would be required.

A new design for a beryllium cell

A new design for a beryllium cell was devised, an update of the design built earlier (described in section 5.2.3) that had the added ability to heat the metal sample, and gas inlet and outlet functions so that hydriding experiments could be conducted whilst the metal sample was inside the XRD machine.

The new beryllium cell was designed to utilise the same pre-made beryllium dome as the earlier design. All changes to the design were made to the base section of the cell. This was intentional because it would be cheaper, easier and more practical to make changes to the aluminium part of the cell rather than to the beryllium section, also the sidewalls and the top of the cell need to be kept clear of obstructions to the x-ray beam. The design for the new beryllium dome with aluminium base cell are shown as a CAD technical diagram in figure 5.22 and diagrams of the cell from various perspectives are shown in figure 5.23.

The new design features of the base section (with reference to figure 5.22) include:

i Two holes (B1, B2) in the base for gas inlet and outlet tubes;

ii Electrical feed-through in the centre (A3);

iii Sample stub in three parts (Parts 4, 5, 6);

The new aluminium base was designed to clamp the lip of the (top hat-shaped) beryllium dome between two aluminium plates with four tiny screws, in the same way as the earlier design. The upper and lower plates that make up the aluminium base are circular, with a diameter of 44mm and a height of 4mm. The lower plate has a steel sample stub with a diameter of 6mm and a height of 20mm (part 6). Above the steel section is a section made of macor, this has a height of 5mm and a diameter of 6mm (part 5). Then, above the macor section, is a copper section with a height of 5mm and a diameter

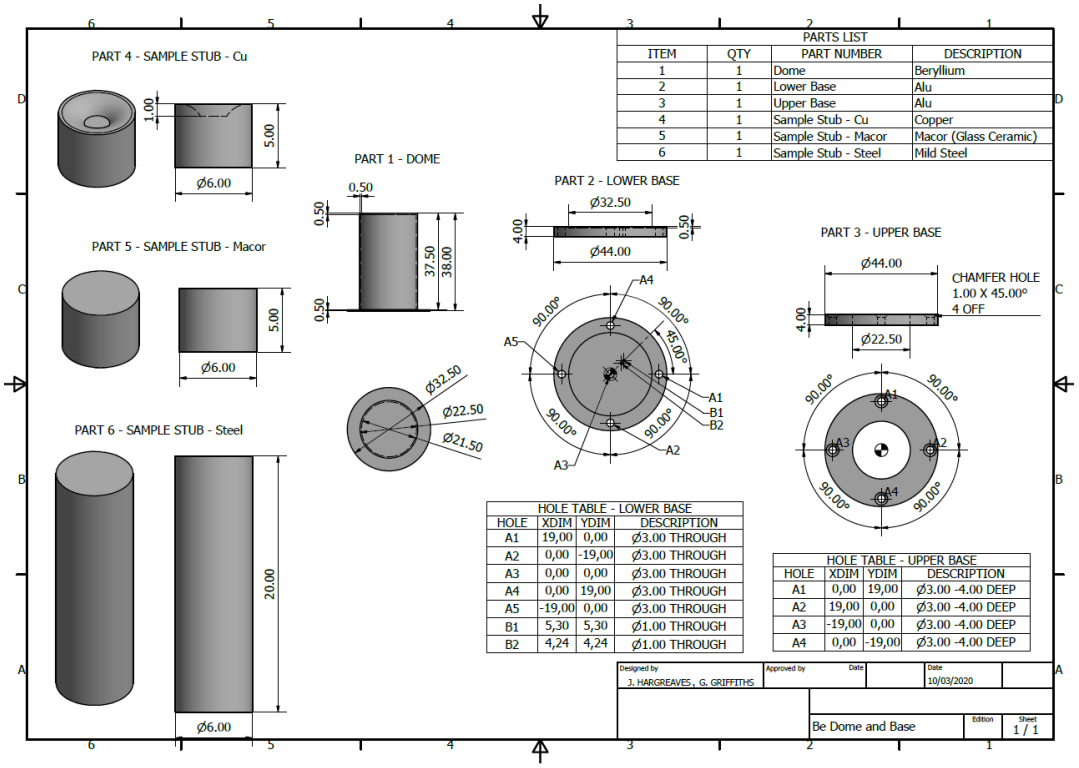

FIGURE 5.22: CAD technical diagram of a new design for a beryllium reaction cell.

of 6mm. The top of the copper section is hollowed out into a bowl with a central depth of 1mm to hold the powdered metal sample.

The lower base plate has three holes in it, one in the centre of the lower base plate for electrical feed through and two, off-centre, for gas inlet and outlet pipes. The inlet pipe (B1) would be connected to a tap which would be, in turn, connected to a supply feed of hydrogen gas to deliver gas into the cell during the hydriding process. The outlet tube (B2) would be connected to a pump in order to evacuate the cell after the UH_3 formation reaction had taken place. The electrical feed-through (A3) would be connected to an external power source and a heating wire would be wrapped around the copper sample holder section of the stub (Part 4) to heat the metal sample. As in the earlier design, a circle of 1mm indium wire is placed underneath the protruding lip of the beryllium dome (in a 0.5mm deep groove inside the lower half of the aluminium base) in order to create an air-tight seal between the

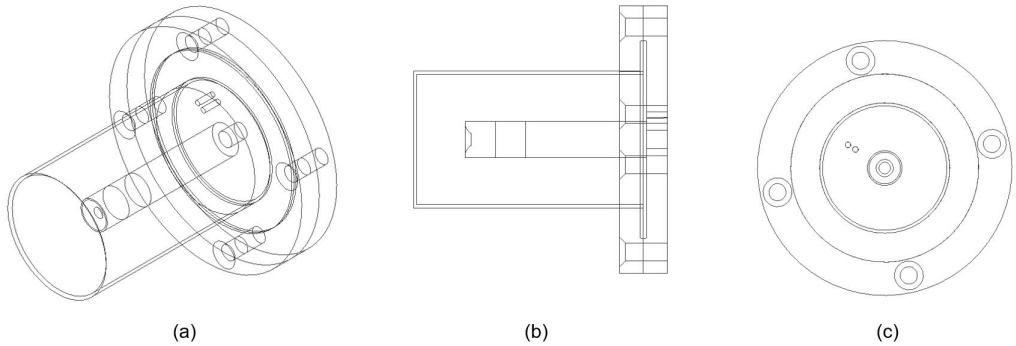

FIGURE 5.23: Various perspectives of a new design for a beryllium reaction cell: (a) angle view; (b) side view; (c) top view.

beryllium and the aluminium base.

The purpose of the section of stub made of macor is to stop thermal conductivity between the copper sample holder and the rest of the cell. For the lower section of the stub (Part 6), steel was chosen because it is less thermally conductive than aluminium. The stub has been increased in height in order to maximise the distance between the indium wire seal (near the bottom of the cell) and the heated copper stub section to avoid melting the indium wire and breaking the airtight seal. The base of the cell would require a circular holder (not included in the design in figure 5.22) with four legs to hold it slightly above the XRD stage, at a height that could be determined by the user, so there would be room underneath the cell for gas and electricity feeds.

The purpose of the new design was to perform an XRD scan of the metal sample before and after each heat-treatment temperature (part of a heat-treatment regime that used incrementally increasing temperatures) to assess any structural changes to the metal sample, and also scans of the hydride (formed in-situ) in between each increase in the heat-treatment temperature.

Unfortunately the design could not plausibly be manufactured in time to perform the experiments (for reasons outlined in the prologue section named ***Covid-19 Statement*** on page ii).

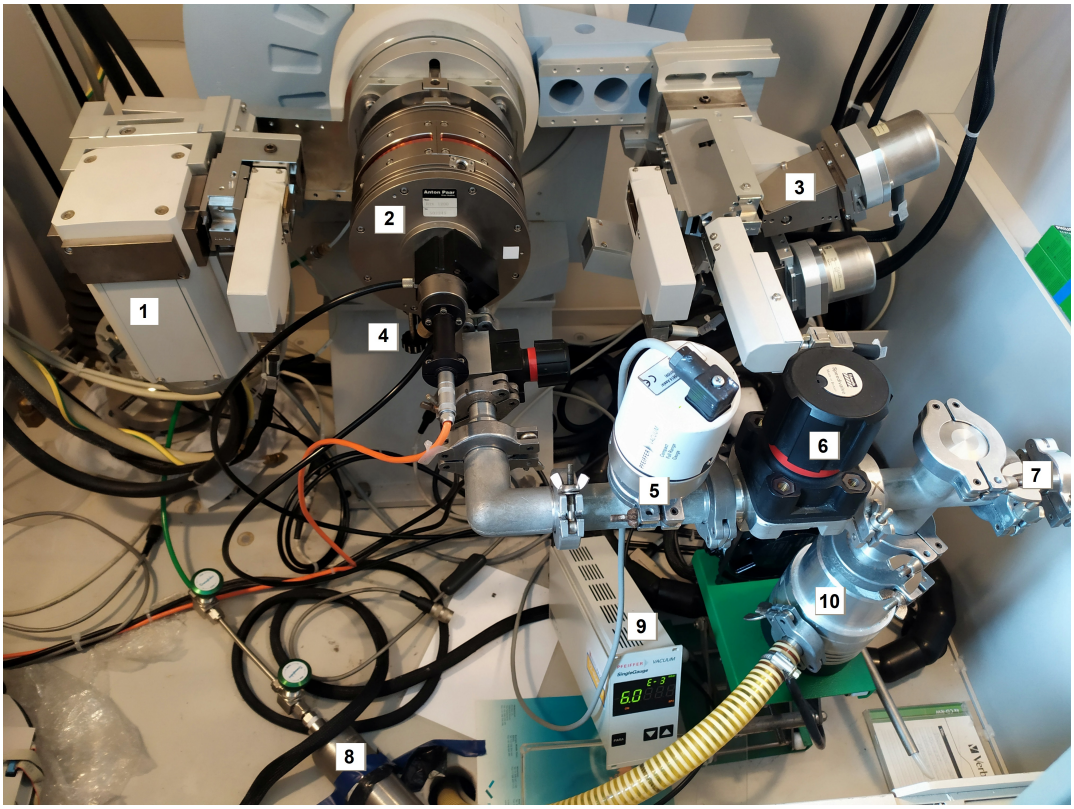

FIGURE 5.24: Experimental set-up developed for in-situ UH_3 reaction hot-stage X-ray diffraction (XRD) analysis.

The XRD Hot Stage

To perform the UH_3 formation/decomposition experiments inside the x-ray diffractometer described above, a HTK 1200 High-Temperature Oven Chamber, developed and produced by Anton Paar (GmbH) for commercial sale, was used.

Figure 5.24 shows the experimental set-up that was developed for the in-situ UH_3 reaction hot-stage X-ray diffraction (XRD) analysis (and for greater simplicity, figure 5.25 shows a P&I diagram of the same set-up). The set-up consisted of:

1. An X-ray tube;
2. A HTK 1200 high temperature oven chamber;
3. An X-ray detector (receiving side);

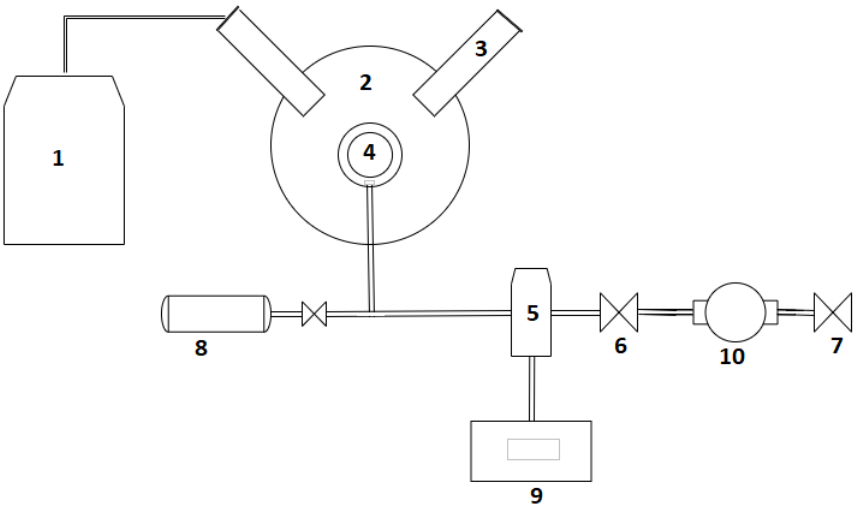

FIGURE 5.25: A simplified piping and instrumentation diagram of in-situ UH_3 reaction hot-stage X-ray diffraction (XRD) analysis.

4. A fitted high-temperature sample stage;
5. A full range pressure gauge;
6. A speed valve;
7. A bleed valve;
8. A 300 ml cylinder (containing pressurised hydrogen gas);
9. A full range gauge controller and digital display;
10. A turbo pump (backed-up by a roughing pump);

The depleted uranium metal sample was installed in the hot stage of the x-ray diffractometer. The reaction chamber was then evacuated using the pumps until the pressure was at $P = 2 \cdot 10^{-3}$ mbar, which was the best vacuum achievable by this equipment. The temperature was raised to $T = 200^{\circ}$ C and the sample was out-gassed under these conditions for 18 hours.

The strategy for performing XRD analysis on the sample during UH_3 formation was to perform many shallow-angled scans focused on a particular range that is known to show a UH_3 peak. This was done so the scans would be as short duration as possible to make it more likely that the resulting data

would show the peak growing over time. The scans were performed over the range $2\theta = 28^\circ - 32^\circ$ and the angular step rate was set to $0.01^\circ s^{-1}$, making each scan 6 minutes 35 seconds in duration.

One (preliminary) scan was performed with the uranium sample under the conditions: $T = 200^\circ$ C and $P_{H2} = 0$ mbar (before hydrogen gas had been inserted into the reaction chamber). Then 20 scans with the sample under the conditions: $T = 200^\circ$ C and $P_{H2} = 1000$ mbar. Then a final scan with the sample under the conditions: $T = 200^\circ$ C and $P_{H2} = 0$ mbar (after the H_2 gas had been pumped out of the reaction chamber).

The data produced by the above procedure is shown if figure 5.26 with the preliminary scan being the bottom curve, the final scan being the top curve, and the 20 scans shown in between in ascending order.

Very little difference can be seen across the different curves. It appears from the graph that UH_3 formation has either not occurred or has not shown in this data over this angular range.

To determine which of these was likely to be the case an XRD scan of a wider angular range was performed to identify any hydride peaks that may have appeared. Figure 5.27 shows the results of the sample inside the XRD hot stage after the attempt to form UH_3 compared to that before. It is clear from the graph that there is no significant change in the XRD data before and after the attempt to form UH_3, because of this is was assumed that no hydride formation had occurred. It was also apparent from the peaks at $2\theta = 28^\circ$, 33°, 47° & 56° that this sample had become contaminated with oxygen. It was decided that this sample should be replaced with a different uranium metal sample that had been polished to remove any surface contamination.

In preparation for a second attempt at the above experiment, a new uranium metal sample was inserted into the hot stage, in the same set-up (figure 5.24). Before attempting the hydride formation experiment again the sample was heated to a range of temperatures and an XRD scan was performed in

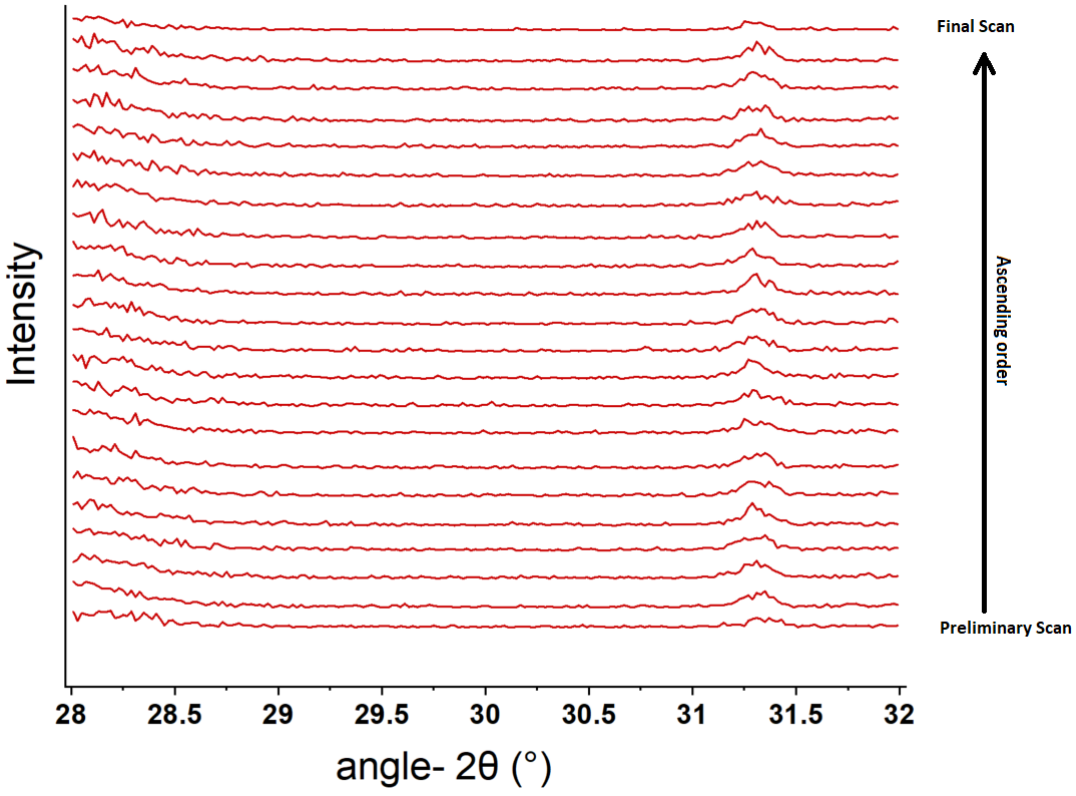

FIGURE 5.26: Graph showing 22 XRD scans during UH_3 formation reaction, one scan before, and one after. The preliminary scan being the bottom curve, the final scan being the top curve, and the 20 scans shown in between in ascending order.

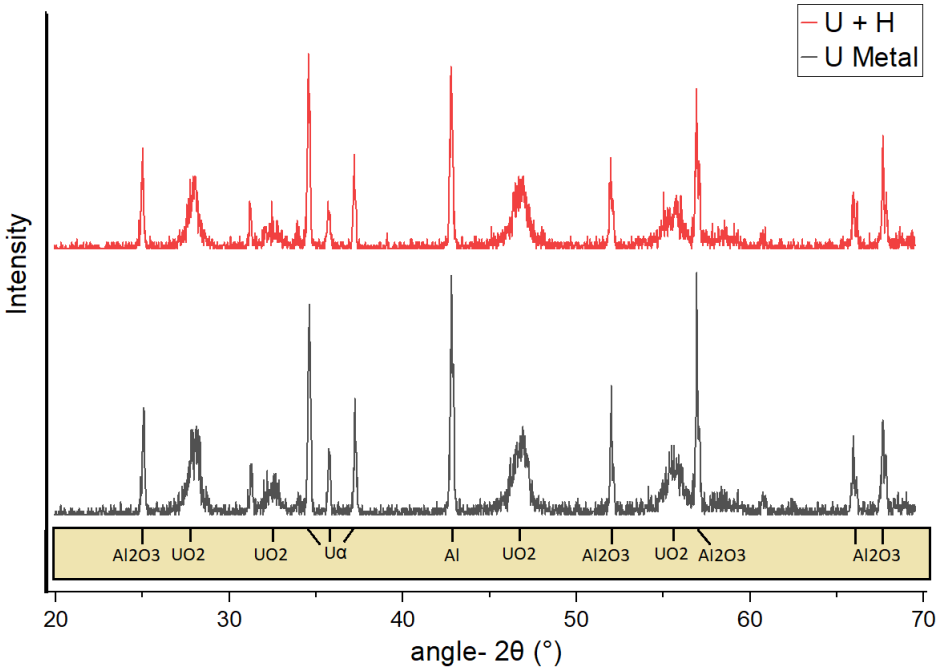

FIGURE 5.27: A graph showing the curves of the data from XRD scans both before (black curve) and after (red curve) the attempted UH_3 formation reaction using the XRD hot stage.

order that any changes in structure (expansion) due to temperature could be accounted for in the final results. The data from the scans at various temperatures are shown in figure 5.28.

The curve for room temperature shows U-α peaks at $2\theta = 34.5°, 35.5°, 36°$ & $38°$ and some quite small UO_2 peaks at $2\theta = 28°, 33°$ & $47°$. As the temperature increases it can be seen that the $U - \alpha$ peaks get progressively smaller and the UO_2 peaks get progressively taller, so much so that only very small $U - \alpha$ peaks can be seen at 200 °C, and at temperatures above 200 °C only UO_2 peaks are present in the data.

It is apparent that this experimental set-up was not appropriate for performing UH_3 formation experiments due to its inability to form a vacuum capable of protecting the metal sample from oxygen contamination at the required temperatures.

The motivation behind the attempt to form and decompose UH_3 inside

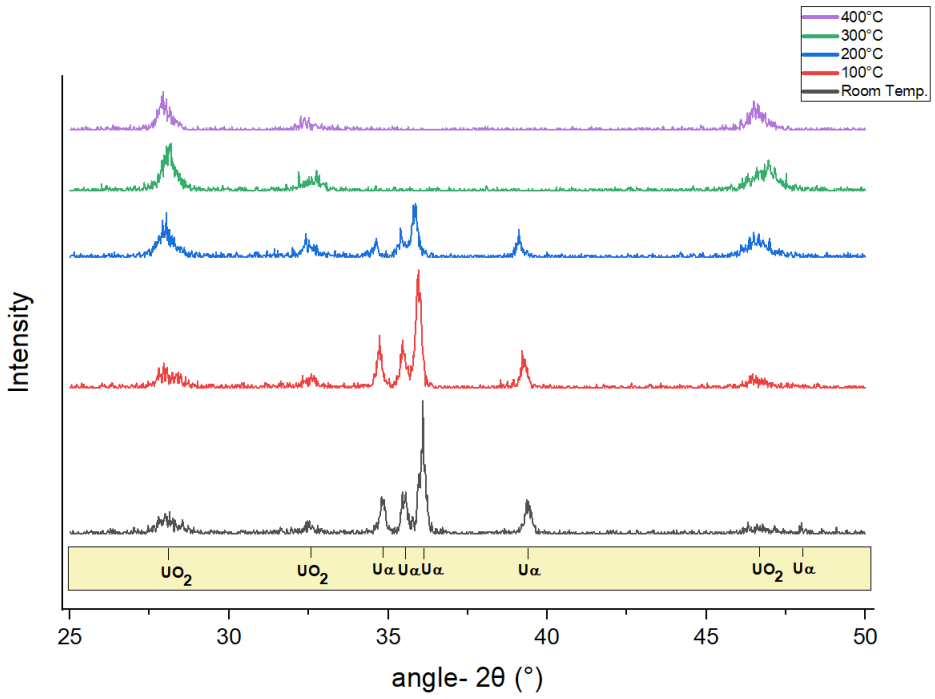

FIGURE 5.28: XRD scans of uranium metal at various temperatures.

the XRD machine was to learn more about when (at which heat treatment temperatures) the new diffraction peaks were becoming visible or increasing in size in the XRD data. The intention was to first scan the sample at all heat treatment temperatures that were to be used, for comparison. Then to subject the metal sample to a series of heat treatments at different temperatures, each heat treatment would involve scanning the sample before the heat treatment, then the heat treatment would be performed and another scan would be performed after the heat treatment. After each heat treatment, the sample could then be exposed to hydrogen gas at 200 °C to form UH_3, a scan of the UH_3 could then be performed before the hydride was decomposed at 500 °C, then a further scan of the sample would be performed. This would provide XRD data of the sample before, during and after each step of the heat treatment and hydride formation/decomposition regime at each of the heat treatment temperatures under investigation.

This could provide further insight into the mechanism that is causing the

new diffraction peaks (and, by association, the increase in the hydrogen uptake rate). It could be the case that the effect was being caused at a particular temperature (though the progressive nature of the curves in figure 5.4 suggests that this isn't the case), in which case the new diffraction peaks would be visible after that heat treatment temperature only. This could also determine if there are any contaminants present at significant amounts that are causing or facilitating the effect, such as carbon (as claimed by Rundle et al., 1948 [108]).

X-Ray Tomography

In order to try to get some direct information about the size of the grains or particles in the sample, and also a comparison before and after heat treatment, x-ray tomography was performed.

A sample holder was designed and made from aluminium that could be airtight sealed and hold some of the powdered uranium sample in the XRT. It was made in this particular way so that it could prevent oxide formation with as little attenuation of the x-rays by the sample holder as possible.

Figure 5.29 shows a selection of XRT scans at amplifications of $4\times$ (with a scale labelled as 2000 μm) and $20\times$ (with a scale labelled as 500 μm).

Some streaking can be seen in the bottom image, this is likely due to the sample moving around inside the sample holder as it was rotated by the XRT machine during the scan.

The size of the grains and particles of the sample both appear to be beyond the resolution of the XRT data so no direct information on their sizes could be gained using this method. The results of this section are, therefore, inconclusive.

Due to a combination of the sample moving inside the sample holder and the resolution of the technique it was decided that a comparison of XRT scans

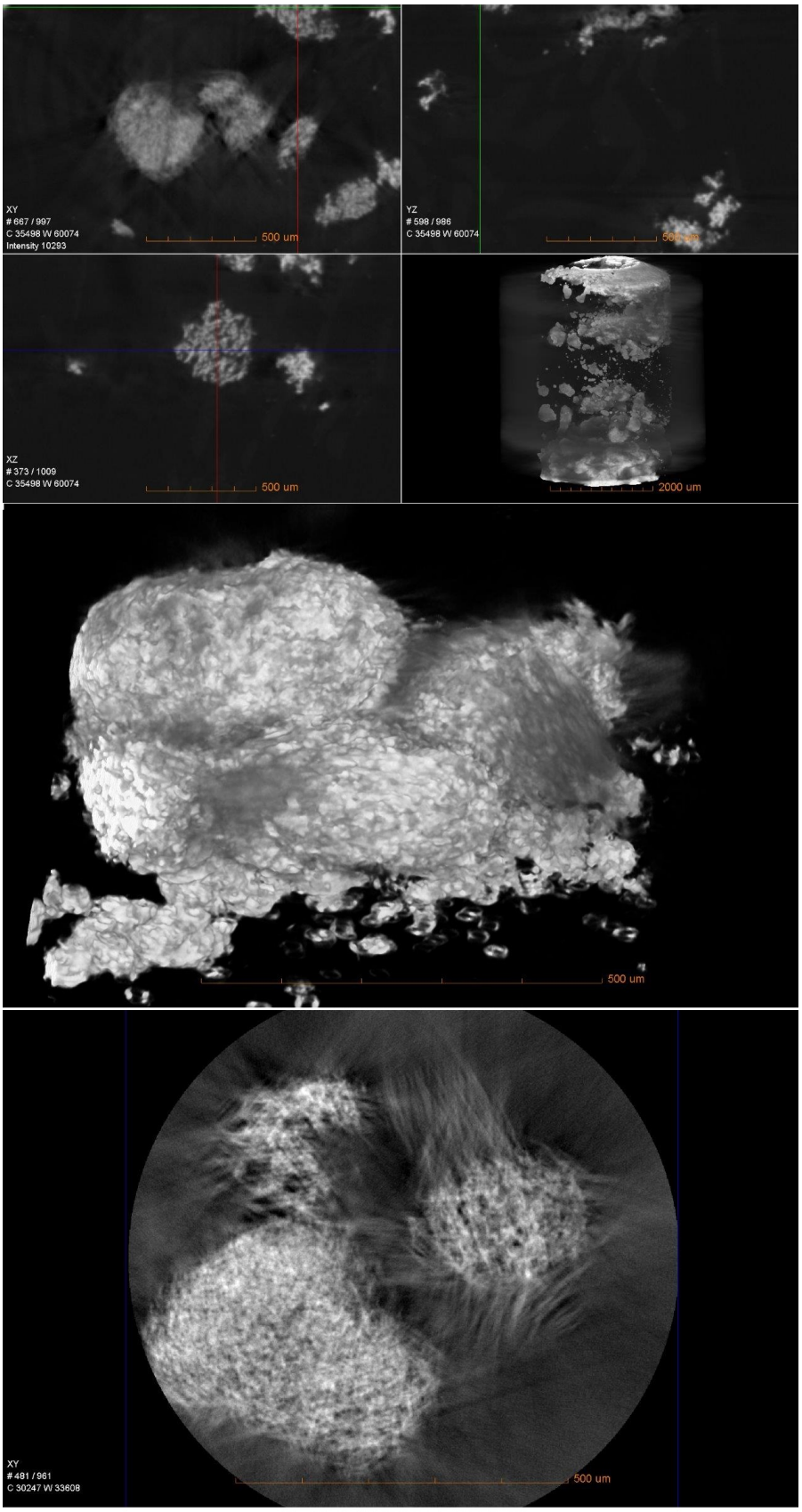

FIGURE 5.29: XRT scan images of uranium powder at amplifications of 4× (with a scale labelled as 2000 μm) and 20× (with a scale labelled as 500 μm).

of the sample before and after heat treatment would not be of value to this investigation.

5.2.6 Discussion

A significant fraction of this work was dedicated to investigating the results of a heat treatment regime performed on uranium metal. It became apparent during the course of this work that both the increase in the rate of uptake of H_2 gas and the new x-ray diffraction peaks were not reproduced when the heat treatment was performed in a crucible made of molybdenum, rather than steel. This was taken as supporting evidence of the claim by Rundle et al. (1947 [64]) that the new peaks were a monoxide phase of uranium and that the presence of carbon is required for the formation of the monoxide. Lattice parameters were calculated from the new XRD peaks (table 5.3), the calculated lattice parameters correspond to the value of the lattice parameter of uranium monoxide quoted by Rundle et al. (1947 [64]), when the error margins of both are taken into consideration. The lattice parameter calculations had to be performed by approximating λ as the wavelength of the x-rays emitted by the XRD machine in § 4.3.6: $\lambda = 1.54$ Å, this is not the true value of λ but had to be substituted in the absence of the true set of values.

Further work should be carried out to determine if the new XRD peaks are a pure monoxide phase of uranium or if they correspond to an oxycarbide compound. It is quite likely that neither imaging characterisation techniques nor crystallographic structure characterisation techniques would have the ability or the resolution to distinguish between the two. The XRD technique that was used in this work would be an insufficient method to distinguish between a monoxide and an oxycarbide of uranium because the diffraction peaks of the two compounds are too close together and would overlap due to diffraction peak broadening (described in § 4.3.5). An appropriate technique

would be Raman spectroscopy, this can determine the bonding energies between atoms in a compound and so would be capable of distinguishing between a monoxide and an oxycarbide.

The shape of the curves for H_2 gas absorption before the heat treatment regime showed a similarity to the shape of a curve of particle surface area vs particle radius, but did not show the same shape after the heat treatment. If we assume that this shape is due to a UH_3 reaction front moving inward into the centre of the bulk metal (the bulk reaction stage), then we must also conclude that the heat treatment is having the effect of speeding up the bulk reaction stage. The (C#) code that was written to generate the graph of surface area vs radius could be expanded to incorporate some kinetic functions of the uranium hydride formation reaction, with the ability to vary the velocity of the reaction front during the bulk reaction stage. This could give some insight into what the curves would look like given a faster bulk reaction, for comparison.

Investigations into grain size and lattice strain before and after the heat treatment were undertaken using the Scherrer equation & the Williamson-Hall Method. The lattice strain in the sample (found by the Williamson-Hall method) showed a decrease of $\approx 58\,\%$ after the heat treatment but the change in grain size (found using both the Scherrer equation & the Williamson-Hall method) were contradictory between the two methods. This leaves the investigations into change in grain size bought about by the heat treatment as being inconclusive. Further investigations were attempted (using XRT) but were ultimately unsuccessful. A direct measurement of grain size before and after heat treatment should be performed using a technique with better resolution than XRT, again, this could be performed using SEM.

Despite the fact that the results for change in grain size showed contradictory results between the two methods, it could be said that they both, nonetheless, showed a change in grain size. The contradictory results lead to

a reluctance to draw that conclusion.

Another piece of follow-up work would be to investigate if the change in hydride reaction rate is associated with the phase changes of the metal. As described in § 2.3, metallic uranium undergoes an $\alpha \rightarrow \beta$ structural phase change at T = 663°C and a $\beta \rightarrow \gamma$ phase change at T = 776°C where the unit cell changes shape, the cell parameters become larger and the metal becomes less dense. As part of this follow-up work, the heat treatment regime should be performed at a temperatures up to and above 776°C to investigate if there is a noticeable change in the hydride reaction reaction rate at the temperature of the $\beta \rightarrow \gamma$ phase change. If it is the case that the increase of hydride reaction rate is associated with the structural phase changes of metallic uranium then some permanent change must be happening at the point of phase change because the phase change is temporary and temperature dependent whilst the change in the reaction rate was observed to be permanent and happened even after the metal was at temperatures far below the phase change temperature. This could give some support to the proposals that the heat treatment is either causing a change in microstrain and grain size, or that the presence of carbon is causing the permanent change by reacting with the metallic uranium at high temperatures.

Chapter 6

Palladium Hydride

6.1 Purity of Palladium Powder

The palladium used in this work was purchased from goodfellow.com, they claim it has a purity of 99.95% and a maximum particle size of 3μm.

Before any palladium hydride experiments were conducted an XRD scan (using the same settings described in §5.2.3) was performed on the palladium powder, in the beryllium dome, to check the composition of the powder (see figure 6.1). The plot of the XRD data shows two aluminium peaks at $2\theta = 38.4°$ and 44.6°, these are due to the base of the beryllium dome. The three palladium peaks can be seen at $2\theta = 40°$, 47° and 68°. The results of this scan suggests that the sample consists of palladium powder only.

6.2 Using TGA to Measure H_2 Gas Absorption

A series of experiments were performed to investigate the effect of gas pressure on the uptake of H_2 gas of powdered palladium metal.

Palladium powder was inserted into the gas rig where palladium hydride was formed (using the same method as described in §4.1) at room temperature and at a range of different H_2 gas pressures. The (palladium hydride)

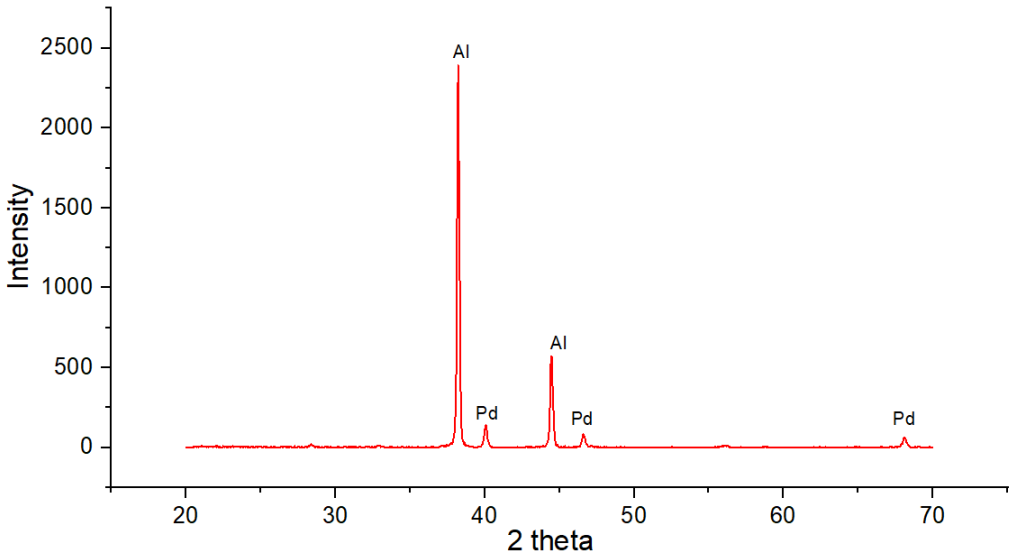

FIGURE 6.1: XRD pattern of palladium sample before hydride experiments.

sample was then inserted into the TGA machine with the intention of measuring the change in mass of the sample with increasing temperature (as the hydride decomposed).

All graphs in this section showing TGA scan data of palladium have all had the 'empty pan' TGA data shown in figure 6.2 subtracted from them before graphing to ensure analysis of data relating to the palladium (hydride) only.

All of the TGA analysis curves traverse a path across the temperature range which was quite unexpected. The PdH_x would be expected to decompose (H_2 gas desorbed from the Pd metal) with increased temperature. In the hydrogen isotope separation technique described in §1.2.1, TCAP, a temperature of ≈150°C is generally used to desorb hydrogen isotopes from palladium. Because of this a reduction in the mass of the sample should be expected, a reduction of 0.03% for α-Pd and 1.32% for β-Pd. Instead all graphs of the TGA data (figure 6.3) show a quite significant increase in mass. In addition to this, all TGA data graphs of $Pd[^1H]_x$ (all curves in figure 6.3 except the yellow one, which refers to $Pd[^2H]_x$) show a curve with a similar

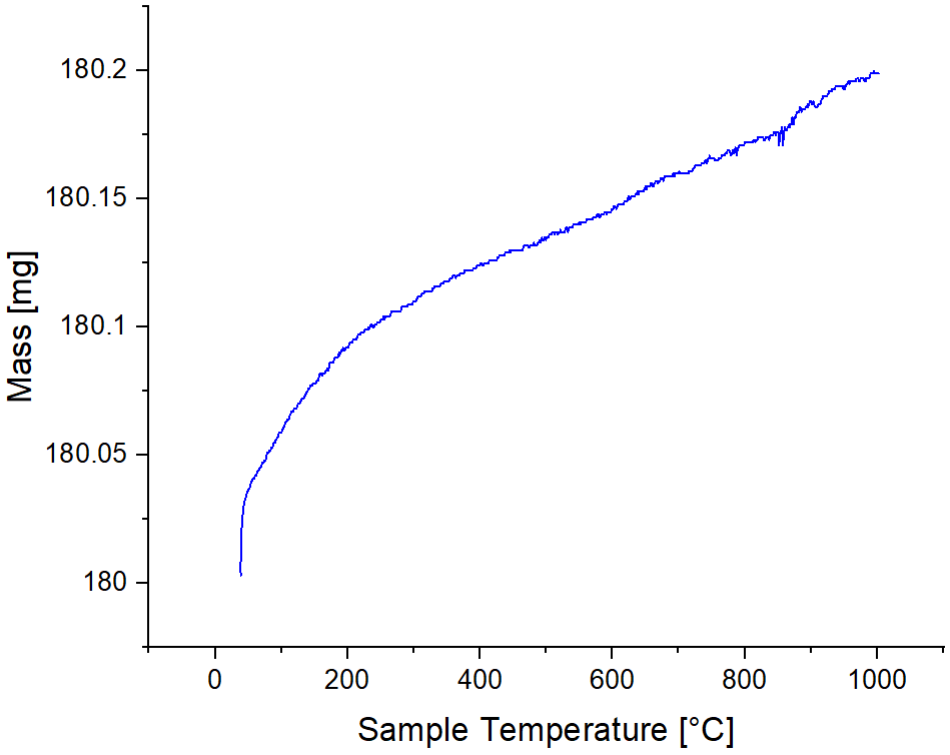

FIGURE 6.2: TGA of the empty pan (between 0 - 1000^{o}C) before palladium analysis

shape and characteristics. In all the graphs there appears to be three distinct regions: first a curve section that shows a (roughly) linear increase in mass with temperature; then (at some point between 200°C and 300°C) the rate of mass increase with temperature accelerates until it reaches a peak (between $\approx$ 600°C and $\approx$ 700°C) and then begins falling until it reaches a second turning point (between $\approx$ 700°C and $\approx$ 800°C); at this point the curves return to a (roughly) linear increase in mass with temperature. The yellow curve in figure 6.3 which refers to Pd[^{2}H]$_x$ shows a similar shape but with a region of mass decrease between room temperature and $\approx$ 200°C and with the peak flattened into a plateau region between $\approx$ 350°C and $\approx$ 500°C.

The shape of the curves look as if there could be a linear increase in mass with temperature with an additional curve of an absorption/desorption process by the Pd metal sample in the central region.

Literature investigation revealed that in a nitrogen environment, such as

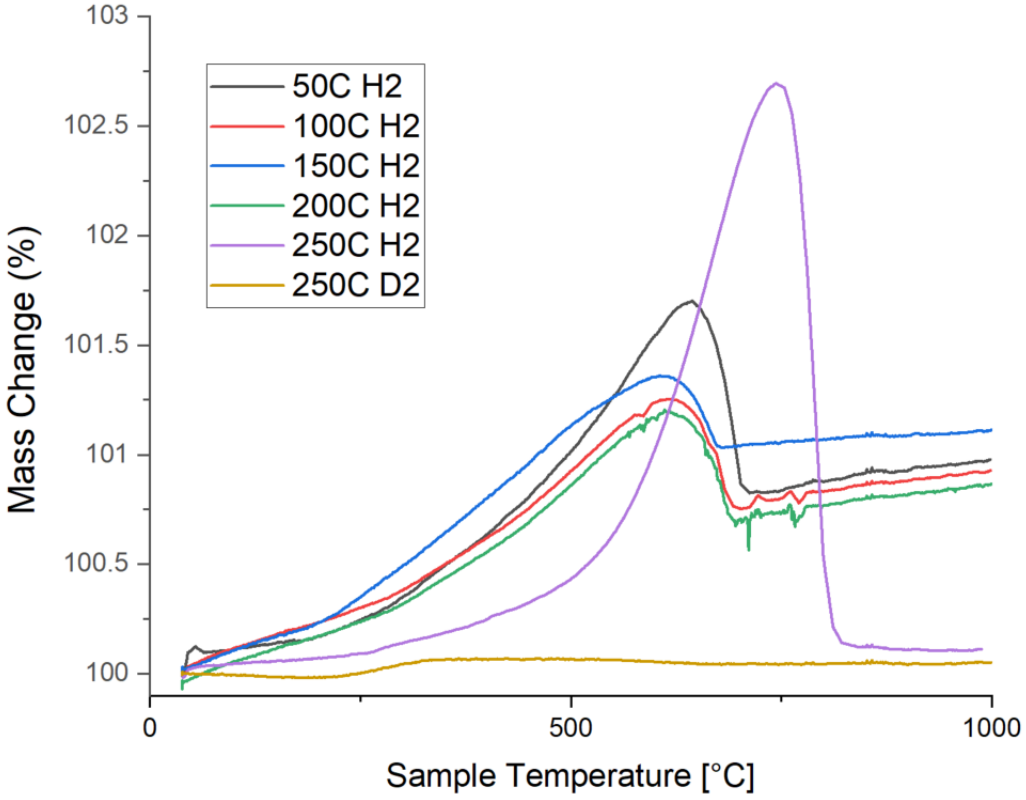

FIGURE 6.3: TGA data curves for palladium hydrides formed at various temperatures. Sample mass: 50^oC = 33.6 mg, 100^oC = 49.4 mg, 150^oC = 44.0 mg, 200^oC = 49.4 mg, 250^oC = 64.0 mg, D2 = 53.8 mg.

the TGA machine, palladium can form a nitride, which is isostructural with pyrite, when heated (reportedly at temperatures "well below 1000 K") [114]. Nitrogen will readily combine with elements with lower electronegativities than itself, resulting in nitride compounds [115]. Nitrogen has an electronegativity = 3.0 [116], whereas palladium has an electronegativity = 2.0 [116].

Experimental studies have shown [114] PdN_2 with a pyrite structure (cubic, a = 4.98 Å) is formed under extreme conditions (1000 K and 58 GPa). The PdN_2 compound produced under high pressure and high temperature becomes unstable under ambient conditions. In theoretical studies ([117, 118]) the potential crystal structures of PdN were also energetically evaluated. Candidates for the most stable structure of PdN are the wurtzite structure (hexagonal, a = 3.37 Å and c = 5.26 Å) [118] and cooperite structure (tetragonal, a = 3.06 Å and c = 5.39 Å) [117]. These formation conditions being taken into account it is assumed that, in this work, it is not possible that PdN_2 would be the compound that was formed and PdN is the compound that will be considered.

6.3 Investigating Palladium Nitride Formation

To investigate if this is the correct explanation, palladium powder was heated in the TGA machine nitrogen environment to 500 °C (shown in figure 6.4). If the TGA process has been creating palladium nitride then this sample should show x-ray diffraction peaks at 2θ = 37.3°, 40.16°, 42.24°, 55.70°, 55.85°, and 66.55° [119].

The x-ray diffraction peaks quoted above could not be seen in the XRD data of the sample (figure 6.5). If PdN or PdN_2 were being formed then a mass increase of 15.2% or 30.4% would be expected, none of the samples in figure 6.3 showed a mass increase greater than 2.7% (the greatest mass

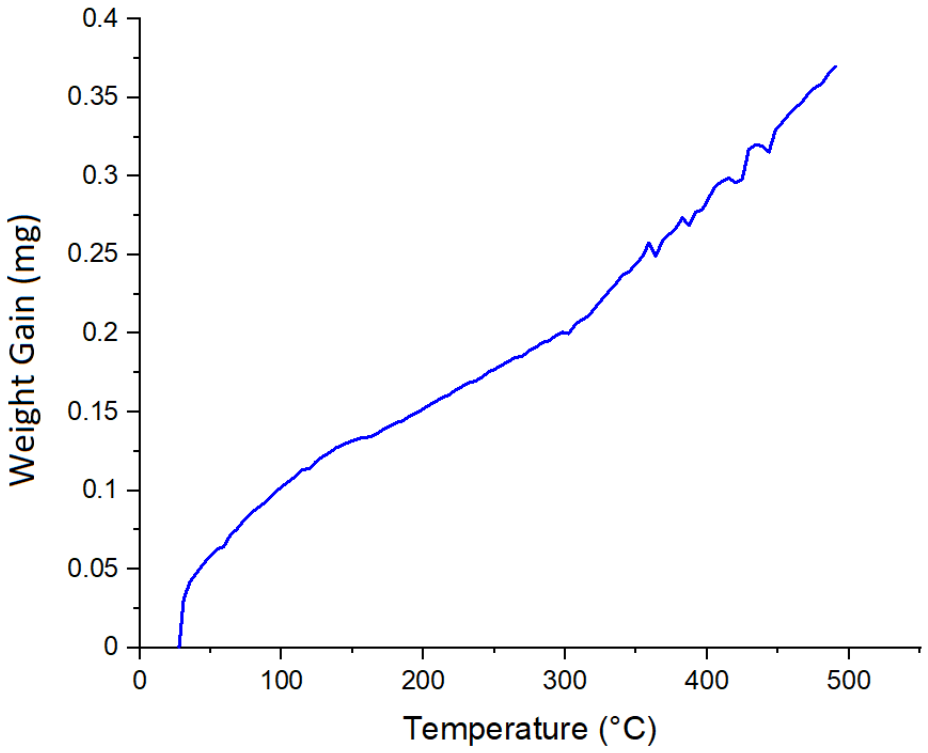

FIGURE 6.4: Palladium nitride formation attempt inside the TGA Machine. Initial sample mass = 52.4 mg.

increase being Pd+H_2 at 250°C at 2.7% increase). These two facts suggest that it is unlikely that the mass increase is due to nitride formation.

Another explanation could be that the controlled environment of the TGA is being contaminated with atmospheric oxygen from a leak in one of the gas pipes outside of the glovebox that it is located in. A study by Pluym et al. (1993 [120]) found that PdO_x could be formed by exposing palladium metal to gaseous oxygen at 500°C and can be decomposed by increasing the temperature to 900°C. Another study by Rey et al. (1978 [121]) found that the presence of hydrogen in the environment during decomposition was found to reduce the temperature required for decomposition to palladium metal.

Unfortunately, at this point, the TGA machine broke down so this technique was no longer available for further research into palladium hydride, nitride or oxide formation.

It was subsequently discovered that one of the pipes transporting gas into

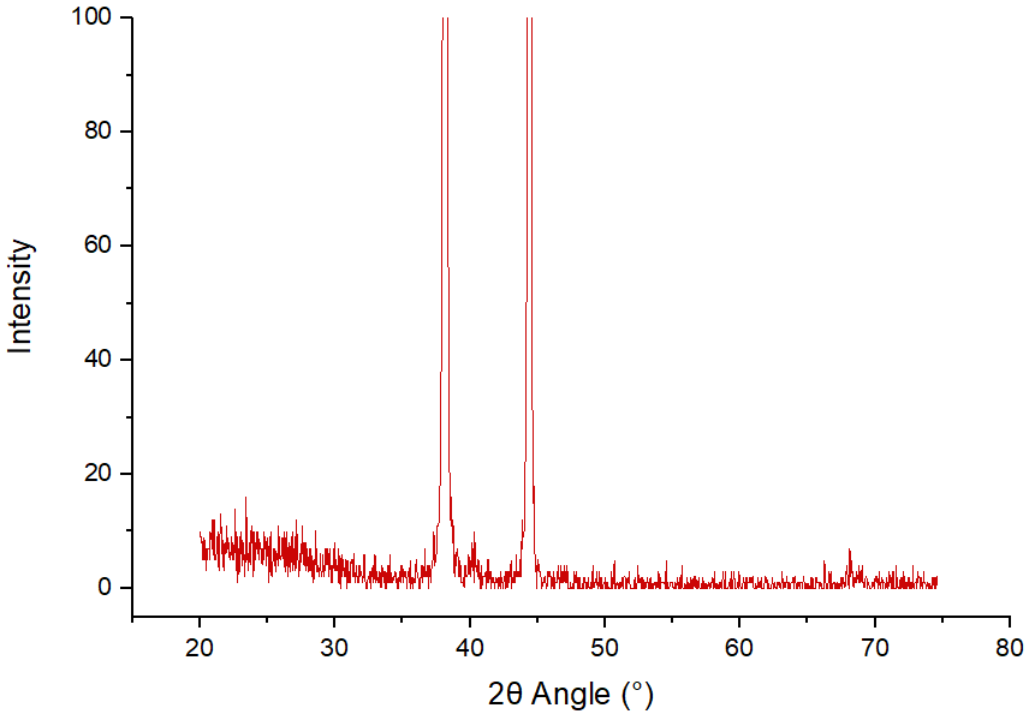

FIGURE 6.5: XRD scan of the palladium nitride formation attempt. The two Al peaks can be seen at 2θ = 38° & 44°, three palladium peaks can be seen (very weakly) at 2θ = 40.4°, 47° and 68.6°. No palladium nitride peaks can be seen.

the system had sprung a very small leak so it seems much more likely that the observed effect during TGA analysis is due to oxide formation, rather than nitride formation.

6.4 Gas Rig PdH_x Formation & Decomposition

A series of palladium hydride formation & decomposition experiments were performed using the same gas rig set-up (shown in figure 4.1) and the same experimental procedure (described in § 4.1).

1g gram of palladium powder was loaded into the molybdenum crucible (shown in figure 5.6) and put into the reaction cell which was then attached to the gas rig. The system was out-gassed for one hour at 200°C before any experiments were performed. A set of hydride formation experiments were conducted at constant temperature (22°C - room temperature) to investigate the effect that varying the H_2 gas pressure has on the uptake rate by the palladium powder. A set of decomposition data was also produced to investigate the effect varying temperature has on the desorption rate.

The percentages of total H_2 gas absorbed in figure 6.6 were found using equation 5.2.

The percentage pressure change over time data for the PdH formation experiments, shown in figure 6.6, shows no relationship between H_2 gas uptake rate and formation pressure. From this set of experiments (1g of palladium powder, at room temperature) the H_2 gas pressure that gives the fastest uptake rate is 1200 mbar and the slowest is 1500 mbar. It seems appropriate to consider this set of experiments to be inconclusive.

The pressure change data of the PdH decomposition experiments, shown in figure 6.7, shows a more progressive ordering than the formation curves. The curve for decomposition at 100°C is clearly the slowest, it also shows a

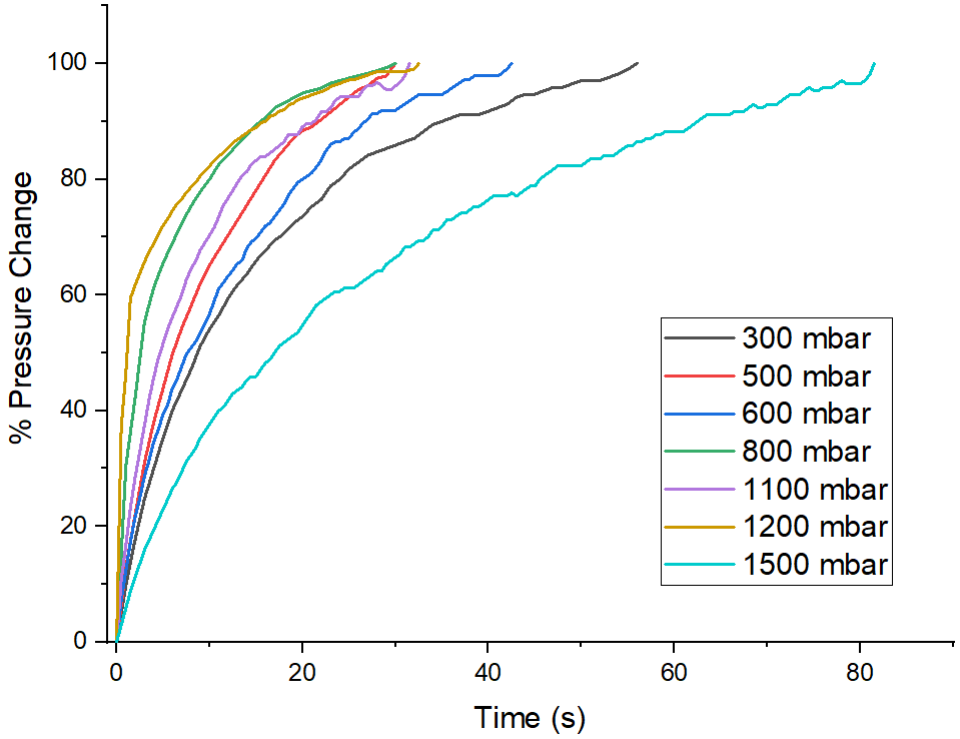

FIGURE 6.6: Percentage gas pressure changes during PdH formation experiments

very different (much flatter) shape than all the other curves, the fastest is the curve for 250°C.

All decomposition curves show a progressively faster desorption rate with increasing temperature except for the curve for decomposition at 200°C. The 200°C curve has a very different shape and height than all the other curves which suggests the possibility that there could have been an issue with the way that particular experiment was conducted or with the way the data was collected.

The decomposition curves are inconsistent in the maximum pressure that is reached through desorbing H_2 gas. This could be because the palladium desorbed H_2 gas at room temperature, which has been reported on in scientific literature [122–124], although not reproduced. The pressure inside the gas rig was observed to be increasing very slowly while the palladium hydride sample was at room temperature so it can be assumed that a small

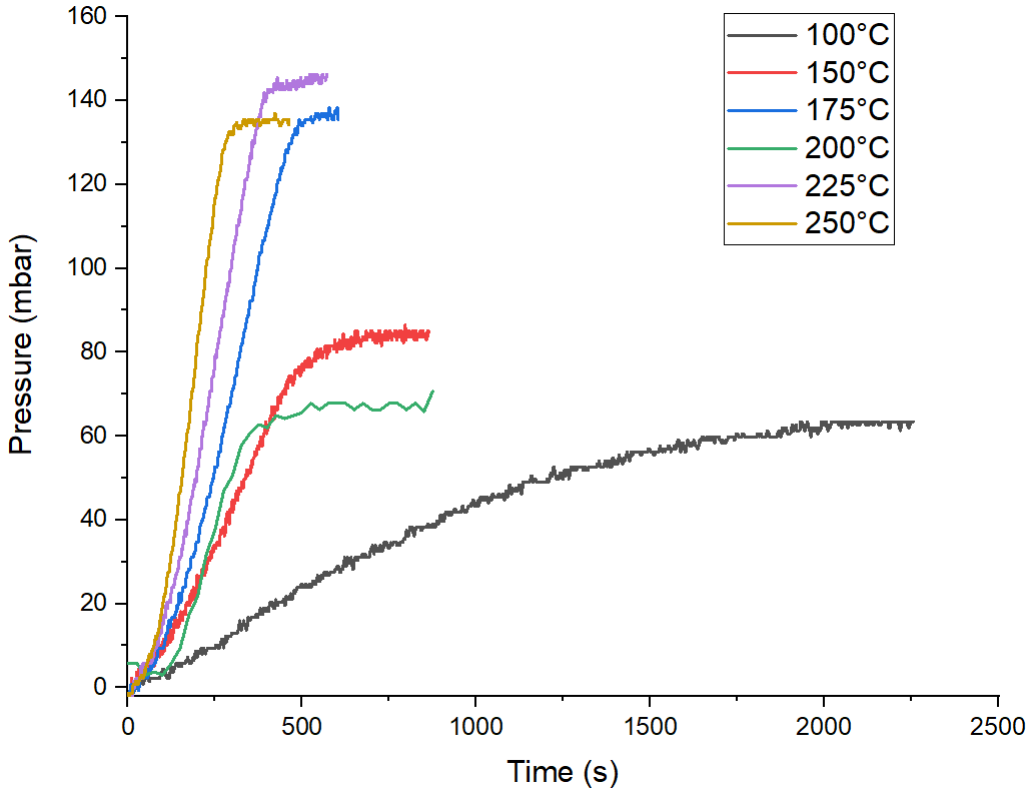

FIGURE 6.7: Pressure change over time due to palladium hydride decomposition at various temperatures.

amount of the H_2 gas was desorbed from the sample before the sample was heated and the pressure data was being logged. This could be the reason for the very different final pressures of the set of curves.

6.5 Discussion

A large amount of time and effort was spent attempting to investigate hydrogen uptake by palladium using TGA. It transpired that the TGA equipment used in the investigation was faulty and the results are unreliable. No reliable conclusions could be drawn from this method due to oxygen contamination.

This method of investigation (using TGA) would be a valid approach for this investigation, and could be attempted in the future, given a TGA machine that is in good working order. The gas used in the controlled environment inside the TGA furnace should be argon not nitrogen to avoid the

possibility of palladium nitride formation.

6.5.1 Optimum Gas Pressure for Hydride Formation

The results of this set of experiments have been considered inconclusive because no relationship at all can be seen between formation pressure and gas uptake rate. This result is in opposition to previous work done on the dependence of hydrogen uptake on gas pressure. Bugaev et al. (2014 [88]) found a very strong dependence of hydrogen concentration in PdH on gas pressure. Figure 6.8 shows the results of their work, hydrogen concentration as a function of (a) pressure and (b) temperature determined by quantitative XANES (X-ray Absorption Near-Edge Structure [125]) fitting with theoretical spectra for models generated using the Monte Carlo approach. Figure 6.8 (a) shows hydrogen concentration plotted against gas pressure (log scale) giving a strong linear relationship (before the intersection point of the curves at $x \approx 0.3$, which corresponds to the transition to β-phase of palladium hydride). They found that the highest hydrogen concentration in PdH obtained for the spectrum, at 50°C and 1000 mbar of hydrogen, was equal to 0.36 ± 0.03. Their results were also given verification by comparing to the work of others. The obtained concentrations and the point of phase transition in their findings are consistent with results obtained by indirect nanoplasmonic sensing [126] and thermogravimetric analysis [127].

This set of experiments requires repeating to investigate if these results will be replicated or if there was just a mistake made while performing the experiments. This investigation would also need to be extended to a range of temperatures, rather than just using room temperature, to give a complete data set.

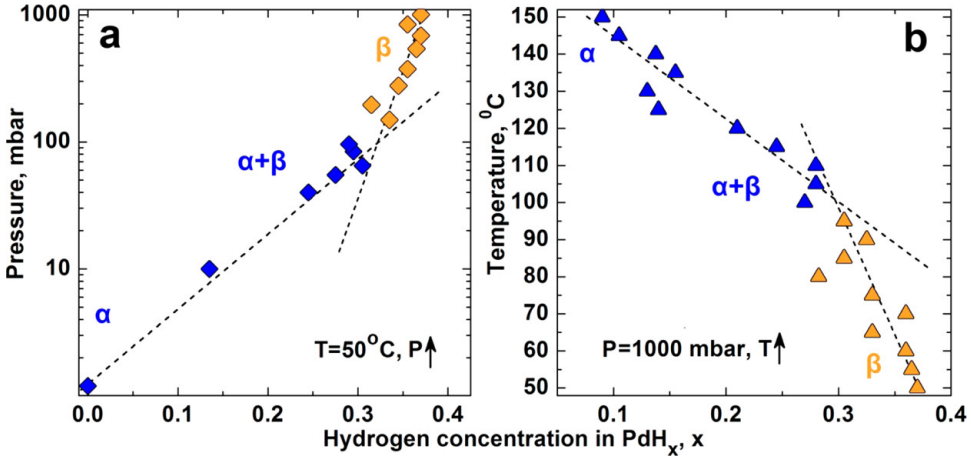

FIGURE 6.8: Hydrogen concentration in PdH as a function of gas pressure (left) & temperature (right). Image taken from [88].

6.5.2 Optimum Temperature for Hydride Decomposition

Out of the range of temperatures used in this work, the temperature that gave the greatest rate of palladium hydride decomposition was 250°C. Though the fastest desorption of hydrogen happened at the highest temperature, and the slowest happened at the lowest, the results did not consistently show a progressively faster desorption rate with increased temperature. All of the results showed a progressing decomposition rate with increased temperature except the curve for 200°C. This could have been because a mistake was made when running that one particular experiment.

The total amount of H_2 gas desorbed by the palladium was recorded as being different every time. This could have been because some of the gas had been desorbed before the sample was bought to temperature and the data was being logged. This phenomenon has been observed in past studies ([122, 123]). This phenomena was also reported by Boudart & Hwang (1975 [124]), they claimed that if PdH was left under dynamic vacuum at room temperature (which the samples during this set of experiments were) then absorbed hydrogen will desorb from the Pd sample but adsorbed hydrogen will not.

Further experiments would need to be performed to determine if it could

be the explanation of the results presented in this work, and if this phenomenon does even exist. If this is the case, then it could be avoided by devising a method of maintaining the palladium hydride at cryogenic temperatures until data logging is started. This could be done by constructing a setup where the reaction cell containing the sample could be easily switched from being in the furnace to being in a vessel that is liquid nitrogen cooled, either by temporarily moving the furnace and switching it for a cooling system or by temporarily moving the cell off the gas rig and into a cooling system until the desorption experiment is ready to be performed.

Chapter 7

Conclusions

The first part of the research undertaken as part of this work found that heat treating uranium in the presence of carbon increases the hydrogen absorption rate of the metal. The effect was observed when the uranium metal was heat treated in a steel crucible but the effect could not be reproduced when the heat treatment was performed using a molybdenum crucible. This effect was observed along with corresponding new XRD peaks and a change in the crystallite size and microstrain of the metal (calculated using the Scherrer equation and the Williamson-Hall method, respectively). Attempts were made to recreate this inside an XRD machine by using an XRD hot stage and by designing an airtight beryllium dome with gas inlet/outlet ability and a heating element, both of which were unsuccessful.

The second part of this work considered the adsorption of hydrogen on palladium at various temperatures. The amount of hydrogen gas uptaken by a palladium sample was initially analysed using a TGA machine but the equipment was found to be faulty. The results produced by this technique were considered to be unreliable and this method was abandoned. The analysis had to be performed using an ultra-high vacuum gas rig (by observing the change in pressure when the gas was desorbed by the metal). This gave a partial data set of the amount of adsorbed gas by a metal sample at various temperatures, the same technique was used for deuterium gas for a single temperature for comparison.

7.1 Tritium Storage

Given the requirements of the fusion industry, recommendations based on the insights gained during this work for optimising the tritium storage system are as follows:

Measures should be taken to minimise the amount of depleted uranium that is being used to store the tritium. Molecular tritium has 6.032 g/mole [128] and depleted uranium has 238.041 g/mole [129], this means that each gram of molecular tritium requires a theoretical minimum of 26.3 grams of depleted uranium to store it as a hydride. For example, the tritium inventory upgrade to 90 grams at CCFE will take, in theory, 2367 grams of depleted uranium to store.

The storage capacity of the uranium in the storage bed could reduce over time due to oxidisation unless an ultra-high vacuum is maintained. The extent of this reduction in capacity will be dependent upon the ability of your tritium storage vacuum system to keep out contaminants. To limit the amount of oxidisation of the uranium in the storage bed it is best that the uranium has as little exposed surface area as possible until it is ready to be used, this would include ensuring the uranium remains in as few pieces as possible.

To prepare the uranium metal it should be polished in an environment where it is protected from oxygen and other contaminants to remove the surface layer, and to cause some deformations on the surface to encourage hydride nucleation sites to form.

The DU metal should be powderised as finely as possible to maximise the reaction kinetics. If possible the powderising of the uranium metal should be done 'in-situ' under a high vacuum, inside the chamber where it will be storing the tritium. It should be done by cycling through a series of hydride formation and decomposition reactions in order to reduce the particle size as

much as possible. During this work it was found that after the fourth cycle the reaction time didn't reduce any further which indicated that the metal powder particles were no longer being reduced in size.

The findings in § 5.2.2 of this work suggests that reaction rates can be improved significantly, and permanently, by heat treating the uranium metal in the presence of carbon. This research found T = 700 °C to be the best temperature, of the temperature range that was investigated.

It should be noted, though, that heat treatment at the temperature that has been recommended will encourage the formation of a monoxide (or possibly an oxycarbide) which could affect the storage capacity of the bed in a way which is not yet fully understood, though this didn't appear to be a noteworthy issue during this work.

7.2 Tritium Separation

Experimental results of the optimum temperatures and pressures, over the ranges that were investigated during this work, have been presented in this thesis. In order to make full recommendations of the best temperatures and pressures to use during the separation of hydrogen isotopes a comprehensive data set would be required. It was not possible, unfortunately, to produce such a data set during the course of this work. Further work needs to be conducted, building on the data presented here, towards a full data set that covers all feasible pressure and temperature ranges.

Because of the low energy nature of the interaction and reactions between palladium and hydrogen the capability for experimenting at cryogenic temperatures would be required to cover the range of temperatures that are of interest.

As with depleted uranium (described above) the particle size of the palladium powder would have a significant effect on the reaction rates and kinetics and should, therefore, be considered as another axis of investigation going forward with this line of research.

Appendix A

C# Code

```
namespace UH3Model
{
    public partial class Form1 : Form
    {
        public Form1()
        {
            InitializeComponent();
        }

        private void Form1_Load(object sender, EventArgs e)
        {
            int i = 0;
            comboBox1.Items.Clear();
            comboBox1.Items.Add("(don't save)");

            foreach( string s in
               Properties.Settings1.Default.files )
            {
                comboBox1.Items.Add( s );
                if ( s ==
                   Properties.Settings1.Default.file )
                {
                    comboBox1.SelectedIndex = i;
                }
                i++;
            }
        }

        private void textBox1_TextChanged(object sender,
           EventArgs e)
        {

        }

        private void button1_Click(object sender,
           EventArgs e)
        {
            try
            {
                double[] dataX = new double[10000];
```

```
double[] dataY = new double[10000];

double start_radius = 0.0;
double steps;
int i = 0;

if (!double.TryParse(textBox1.Text, out
   start_radius))
{
    MessageBox.Show("Invalid radius");
    return;
}

if (!double.TryParse(textBox2.Text, out
   steps))
{
    MessageBox.Show("Invalid radius");
    return;
}

double radius = start_radius;

double step = start_radius / steps;

while (radius >= 0.0)
{
    dataX[i] = radius;

    double result = 4 * Math.PI * radius *
       radius;

    dataY[i] = result;

    radius = radius - step;
    i++;
}


double[] plotx = new double[i];
double[] ploty = new double[i];

for (int ii = 0; ii < i; ii++)
{
    plotx[ii] = dataX[ii];
    ploty[ii] = dataY[ii];
}

formsPlot1.Plot.AddScatter(plotx, ploty);
formsPlot1.Refresh();

string fname = comboBox1.Text;

if ( fname != "(don't save")
{
    StreamWriter s = new
       StreamWriter(fname);
```

```
                    s.WriteLine("Radius, Surface Area");

                    for( int j = 0; j < plotx.Length; j++ )
                    {
                        s.Write(plotx[j]);
                        s.Write(", ");
                        s.WriteLine(ploty[j]);
                    }
                    s.Close();
                }
            }
            catch (Exception ex)
            {

            }
        }

        private void checkBox1_CheckedChanged(object
            sender, EventArgs e)
        {

        }

        SaveFileDialog saveFileDialog = new
            SaveFileDialog();
        bool saveit = false;

        private void button2_Click(object sender,
            EventArgs e)
        {
            SaveFileDialog saveFileDialog = new
                SaveFileDialog();
            saveFileDialog.FileName = "data";
            saveFileDialog.Filter = "CSV files (*.csv)|
                *.csv" ;

            if (saveFileDialog.ShowDialog() ==
                DialogResult.OK )
            {
                saveit = true;
                string fname = saveFileDialog.FileName;
                Properties.Settings1.Default.file = fname;
                Properties.Settings1.Default.files.Add(fname);
                Properties.Settings1.Default.Save();

                Form1_Load(sender, e);
            }
        }
    }
}
```

Bibliography

[1] Jet: the joint european torus - culham centre for fusion energy. https://ccfe.ukaea.uk/programmes/joint-european-torus/. Accessed: 2023-09-12.

[2] PD Brennan. Long term operation of the jet facilities' active gas handling system. *Fusion science and technology*, 41(3P2):578–582, 2002.

[3] UKAEA Scientific Publications. URL https://scientific-publications.ukaea.uk/all-papers/?wpv_aux_current_post_id=14660&wpv_aux_parent_post_id=14660&wpv_view_count=14659&wpv_paged=209. [Online; accessed 2023-06-08].

[4] Joakim Andersson and Stefan Grönkvist. Large-scale storage of hydrogen. *International Journal of Hydrogen Energy*, 44(23):11901–11919, 2019. ISSN 0360-3199. doi: https://doi.org/10.1016/j.ijhydene.2019.03.063.

[5] A Banos, NJ Harker, and TB Scott. A review of uranium corrosion by hydrogen and the formation of uranium hydride. *Corrosion Science*, 136:129–147, 2018.

[6] J Davis. Locations of stable metal tritide use at the savannah river site. *US Dept. of Energy*, 2017.

[7] Saturation properties for hydrogen, NIST chemistry webbook. https://webbook.nist.gov/cgi/fluid.cgi?Action=Load&ID=C1333740&Type=SatT&Digits=5&PLow=.5&PHigh=1.5&PInc=.1&

RefState=DEF&TUnit=K&PUnit=atm&DUnit=kg/m3&HUnit=kJ/mol&WUnit=m/s&VisUnit=uPa*s&STUnit=N/m. Accessed: 2022-01-10.

[8] H. Barthelemy, M. Weber, and F. Barbier. Hydrogen storage: Recent improvements and industrial perspectives. *International Journal of Hydrogen Energy*, 42(11):7254–7262, 2017. ISSN 0360-3199. doi: https://doi.org/10.1016/j.ijhydene.2016.03.178. Special issue on The 6th International Conference on Hydrogen Safety (ICHS 2015), 19-21 October 2015, Yokohama, Japan.

[9] 2020 annual figures for holdings of civil depleted, natural and low enriched uranium (dnleu) in the nuclear fuel cycle - united kingdom. https://www.onr.org.uk/safeguards/civilplut20.htm. Accessed: 2022-01-10.

[10] Future energy scenarios 2020. https://www.nationalgrideso.com/document/173821/download. Accessed: 2022-01-27.

[11] Energy consumption in the UK 2020. https://assets.publishing.service.gov.uk/government/uploads/system/uploads/attachment_data/file/1020153/2020_ECUK_Press_Notice.pdf. Accessed: 2022-01-10.

[12] Anita S Horen and Myung W Lee. Metal hydride based isotope separation–large-scale operations. *Fusion Technology*, 21(2P2):282–286, 1992.

[13] Myung W Lee. Thermal cycling absorption process—a new way to separate hydrogen isotopes. *Westinghouse Savannah River Co. WSRC-MS-2000-00061*, pages 197–200, 2000.

[14] LK Heung, HT Sessions, and X Xiao. TCAP hydrogen isotope separation using palladium and inverse columns. *Fusion Science and Technology*, 60(4):1331–1334, 2011.

[15] Plug flow reactors and comparison to continuously stirred tank reactors. https://chem.libretexts.org/@go/page/46936. Accessed: 2022-01-31.

[16] Xin Xiao, L Kit Heung, and Henry T Sessions. Recent advances in SRS on hydrogen isotope separation using thermal cycling absorption process. *Fusion Science and Technology*, 67(3):643–646, 2015.

[17] JE Klein. Conceptual design for consolidation TCAP. Technical report, Savannah River Site (SRS), Aiken, SC (United States), 1999.

[18] MS Ortman, LK Heung, A Nobile, and RL Rabun III. Tritium processing at the savannah river site: Present and future. *Journal of Vacuum Science & Technology A: Vacuum, Surfaces, and Films*, 8(3):2881–2889, 1990.

[19] C Laquerbe, D Ducret, A Ballanger, T Pelletier, O Baudouin, and P Sere Peyrigain. Optimization of a thermal cycling absorption process design by dynamic simulation. *Fusion science and technology*, 41(3P2): 1121–1125, 2002.

[20] Anita S Poore. Ht-tcap protium-deuterium (hd) test summary, part i. Technical report, WSRC-TR-2004-00274, May, 2004.

[21] Anita S Poore. Material and process characterization testing summary for ht-tcap. Technical report, WSRC-2004-00275, May, 2004.

[22] Steve Xiao, Ben Randall, Bob Rabun, Boone Thompson, and Bruce Tatarchuk. Heat and mass transfer study to understand thermal-cycling absorption process (tcap) scale-up issues. Technical report, Savannah River Site (SRS), Aiken, SC (United States). Savannah River . . . , 2019.

[23] J Calvin Giddings. A practical criterion for minimum coil diameter in gas chromatography. *Analytical chemistry*, 37(12):1580–1581, 1965.

[24] Renju Zacharia and Sami Ullah Rather. Review of solid state hydrogen storage methods adopting different kinds of novel materials. *Journal of Nanomaterials*, 2015:1–18, 2015.

[25] Jose Bellosta Von Colbe, Jose-Ramón Ares, Jussara Barale, Marcello Baricco, Craig Buckley, Giovanni Capurso, Noris Gallandat, David M Grant, Matylda N Guzik, Isaac Jacob, et al. Application of hydrides in hydrogen storage and compression: Achievements, outlook and perspectives. *international journal of hydrogen energy*, 44(15):7780–7808, 2019.

[26] Emil H Jensen, Martin Dornheim, and Sabrina Sartori. Scaling up metal hydrides for real-scale applications: Achievements, challenges and outlook. *Inorganics*, 9(5):37, 2021.

[27] Joakim Andersson and Stefan Grönkvist. Large-scale storage of hydrogen. *International journal of hydrogen energy*, 44(23):11901–11919, 2019.

[28] JD Lawson. Some criteria for a useful thermonuclear reactor. *Atomic Energy Research Establishment*, 1955.

[29] JET Team et al. Fusion energy production from a deuterium-tritium plasma in the jet tokamak. *Nuclear Fusion*, 32(2):187, 1992.

[30] Renato Perillo. *Plasma Chemistry in Divertor Relevant Plasmas*. PhD thesis, 10 2019.

[31] John McPhee. The curve of binding energy: A journey into the awesome and alarming world of theodore b. *Taylor. 8vo, original cloth, dust jacket. NY: Farrar, Straus, Giroux*, 1974.

[32] N Gauthier. Nuclear force strength: a simple estimate. *European Journal of Physics*, 16(1):21, 1995.

[33] SD Drell. Nuclear radius and nuclear forces. *Physical Review*, 100(1):97, 1955.

[34] Peter Schlosser, Martin Stute, Helmut Dörr, Christian Sonntag, and Karl Otto Münnich. Tritium/^{3}He dating of shallow groundwater. *Earth and Planetary Science Letters*, 89(3):353–362, 1988.

[35] DR Hamilton, WP Alford, and L Gross. Limit on neutrino mass from tritium beta spectrum. Technical report, Princeton Univ., 1951.

[36] B Wheatley. Sources of tritium and its behaviour upon release to the environment dg jacobs. usaec critical review series, clearinghouse for federal scientific and technical information, springfield, va. 22151, 1968. 90 pp.(paper). *Journal of Nuclear Energy*, 23:375, 1969.

[37] Richard Wakeford. The Windscale Reactor Accident - 50 Years On. *Journal of Radiological Protection*, 27(3):211, 2007.

[38] Paul W Lisowski. Accelerator production of tritium: A review and look ahead. Technical report, Los Alamos National Laboratory (LANL), 2014.

[39] M. Kovari, M. Coleman, I. Cristescu, and R. Smith. Tritium resources available for fusion reactors. *Nuclear Fusion*, 58(2):026010, dec

2017. doi: 10.1088/1741-4326/aa9d25. URL https://doi.org/10.1088/1741-4326/aa9d25.

[40] MM Popov, Iu V Gagarinskii, MD Senin, IP Mikhalenko, and Iu M Morozov. The average ß-particle energy and decay constant of tritium. *Atomic Energy*, 4(3):393–396, 1958.

[41] B Bornschein, Chr Day, D Demange, and T Pinna. Tritium Management and Safety Issues in ITER and DEMO Breeding Blankets. *Fusion Engineering and Design*, 88(6):466–471, 2013.

[42] Lester R Morss, Norman M Edelstein, Jean Fuger, and Joseph Jacob Katz. *The Chemistry of the Actinide and Transactinide Elements (Volumes 1-5): Vol. 1*, volume 1. Springer Science & Business Media, 2007.

[43] Royal society of chemistry, periodic table - uranium. http://www.rsc.org/periodic-table/element/92/uranium, note = Accessed: 2021-11-24.

[44] CS Barrett, MH Mueller, and RL Hitterman. Crystal structure variations in alpha uranium at low temperatures. *Physical Review*, 129(2):625, 1963.

[45] J Thewlis. An X-ray Powder Study of β-Uranium. *Acta Crystallographica*, 5(6):790–794, 1952.

[46] A. Rough, F. Bauer. Constitution of Uranium and Thorium Alloys. Technical report, Battelle Memorial Inst., Columbus, Ohio, 1958.

[47] NE Holden. Isotopic composition of the elements and their variation in nature: a preliminary report. Technical report, Brookhaven National Lab., Upton, NY (USA), 1977.

[48] Elena S Craft, Aquel W Abu-Qare, Meghan M Flaherty, Melissa C Garofolo, Heather L Rincavage, and Mohamed B Abou-Donia. Depleted

and natural uranium: chemistry and toxicological effects. *Journal of Toxicology and Environmental Health, Part B*, 7(4):297–317, 2004.

[49] Maria Betti, Gabriele Tamborini, and Lothar Koch. Use of secondary ion mass spectrometry in nuclear forensic analysis for the characterization of plutonium and highly enriched uranium particles. *Analytical Chemistry*, 71(14):2616–2622, 1999.

[50] Chiara Cantaluppi and Sandro Degetto. Civilian and military uses of depleted uranium: environmental and health problems. *ANNALI DI CHIMICA-ROMA-*, 90(11/12):665–676, 2000.

[51] DK Craig. Chemical and radiological toxicity of uranium and its compounds. *Westinghouse Savannah River Company: Aiken, SC*, 2001.

[52] World Health Organization et al. Depleted uranium: sources, exposure and health effects. 2001.

[53] Sam Keith, Obaid Faroon, Nickolette Roney, Franco Scinicariello, Sharon Wilbur, Lisa Ingerman, Fernando Llados, Daneil Plewak, David Wohlers, and Gary Diamond. Toxicological profile for uranium. *Agency for Toxic Substances and Disease Registry (ATSDR)(US), Atlanta*, 2013.

[54] RW Leggett and JD Harrison. Fractional absorption of ingested uranium in humans. *Health Physics*, 68(4):484–498, 1995.

[55] WM Albrecht and MW Mallett. Reaction of Hydrogen With Uranium. *Journal of The Electrochemical Society*, 103(7):404–409, 1956.

[56] J. Bloch and M. H. Mintz. Kinetics and Mechanism of the UH Reaction. *Journal of the Less Common Metals*, 81(2):301–320, 1981.

[57] Joseph E Burke and Cyril Stanley Smith. The formation of uranium hydride1. *Journal of the American Chemical Society*, 69(10):2500–2502, 1947.

[58] R. S. Lillard, C. D. Taylor, J. R. Wermer, N. A. Mara, and J. C. Cooley. A Thermal Desorption Study of The Kinetics of Uranium Hydride Decomposition. *Journal of Nuclear Materials*, 444(1):49–55, 2014.

[59] Linus Pauling and Fred J Ewing. The Structure of Uranium Hydride. *Journal of the American Chemical Society*, 70(4):1660–1661, 1948.

[60] AS Kitzes. Uranium Hydride: A Survey. Technical report, Oak Ridge National Lab., Tenn., 1950.

[61] R. Mulford, F. Ellinger, and W. Zachariasen. A New Form of Uranium Hydride1. *Journal of the American Chemical Society*, 76(1):297–298, 1954.

[62] Q. Johnson, T. Biel, and H. Leider. Isotopic Shifts of the Unit Cell Constants of the α and β Tri-hydrides of Uranium: UH3, UD3, UT3. *Journal of Nuclear Materials*, 60(2):231–233, 1976.

[63] Robert D Kolasinski, Andrew D Shugard, Craig R Tewell, and Donald F Cowgill. Uranium for hydrogen storage applications: A materials science perspective. *Sandia National Lab# SAND2010-5195, Albuquerque*, 2010.

[64] R. Rundle. The Structure of Uranium Hydride and Deuteride1. *Journal of the American Chemical Society*, 69(7):1719–1723, 1947.

[65] A. Lawson, A. Severing, J. Ward, C. Olsen, J. Goldstone, et al. Vibrational and Magnetic Properties of β-UD 3. *Journal of the Less Common Metals*, 158(2):267–274, 1990.

[66] BM Abraham and HE Flotow. The heats of formation of uranium hydride, uranium deuteride and uranium tritide at 25 degrees 1. *Journal of the American Chemical Society*, 77(6):1446–1448, 1955.

[67] G. L. Powell, W. L. Harper, and J. R. Kirkpatrick. The Kinetics of the Hydriding of Uranium Metal. *Journal of the Less Common Metals*, 172: 116–123, 1991.

[68] H. Flotow, Harold R. Lohr, B. Abraham, and D. Osborne. The Heat Capacity and Thermodynamic Functions of β-Uranium Hydride from 5 to 350°c k. 1, 2. *Journal of the American Chemical Society*, 81(14):3529–3533, 1959.

[69] W. Bartscher, A. Boeuf, R. Caciuffo, J. Fournier, W. Kuhs, J. Rebizant, and F. Rustichelli. Neutron Diffraction Study of β-UD 3 and β-UH 3. *Solid state communications*, 53(4):423–426, 1985.

[70] K. J. Laidler. The Development of The Arrhenius Equation. *Journal of Chemical Education*, 61(6):494, 1984.

[71] A Banos, CP Jones, and TB Scott. The effect of work-hardening and thermal annealing on the early stages of the uranium-hydrogen corrosion reaction. *Corrosion Science*, 131:147–155, 2018.

[72] J. Bloch and M. H. Mintz. Kinetics and Mechanisms of Metal Hydrides Formation: A review. *Journal of Alloys and Compounds*, 253:529–541, 1997.

[73] Robert M Harker. The influence of oxide thickness on the early stages of the massive uranium–hydrogen reaction. *Journal of alloys and compounds*, 426(1-2):106–117, 2006.

[74] J Bloch, D Brami, A Kremner, and MH Mintz. Effects of gas phase impurities on the topochemical-kinetic behaviour of uranium hydride development. *Journal of the Less Common Metals*, 139(2):371–383, 1988.

[75] CT Rettner, DJ Auerbach, JC Tully, and AW Kleyn. Chemical dynamics at the gas- surface interface. *The Journal of Physical Chemistry*, 100(31): 13021–13033, 1996.

[76] Christopher P Jones, Thomas B Scott, James R Petherbridge, and Joseph Glascott. A surface science study of the initial stages of hydrogen corrosion on uranium metal and the role played by grain microstructure. *Solid State Ionics*, 231:81–86, 2013.

[77] JF Bingert, RJ Hanrahan Jr, RD Field, and PO Dickerson. Microtextural investigation of hydrided α-uranium. *Journal of alloys and compounds*, 365(1-2):138–148, 2004.

[78] Geoff W Brown. The influence of surface morphology and oxide microstructure on the nucleation and growth of uranium hydride on alpha uranium.

[79] A Banos, CA Stitt, and TB Scott. The effect of sample preparation on uranium hydriding. *Corrosion Science*, 113:91–103, 2016.

[80] R Arkush, A Venkert, M Aizenshtein, S Zalkind, D Moreno, M Brill, MH Mintz, and N Shamir. Site related nucleation and growth of hydrides on uranium surfaces. *Journal of alloys and compounds*, 244(1-2): 197–205, 1996.

[81] LW Owen and RA Scudamore. A microscope study of the initiation of the hydrogen-uranium reaction. *Corrosion Science*, 6(11-12):461–468, 1966.

[82] J Bloch, F Simca, M Kroup, A Stern, D Shmariahu, MH Mintz, and Z Hadari. The initial kinetics of uranium hydride formation studied by a hot-stage microscope technique. *Journal of the Less Common Metals*, 103(1):163–171, 1984.

[83] Moshe H Mintz and J Bloch. Evaluation of the kinetics and mechanisms of hybriding reactions. *Progress in solid state chemistry*, 16(3):163–194, 1985.

[84] D. P. Broom. *Hydrogen Storage Materials: The Characterisation of Their Storage Properties*. Springer Science & Business Media, 2011.

[85] Michael C. Weinberg, Dunbar P. Birnie, and Vitaly A. Shneidman. Crystallization kinetics and the jmak equation. *Journal of Non-Crystalline Solids*, 219:89–99, 1997. ISSN 0022-3093. doi: https://doi.org/10.1016/S0022-3093(97)00261-5. URL https://www.sciencedirect.com/science/article/pii/S0022309397002615. Glass Crystallization.

[86] Joseph Bloch. The kinetics of a moving metal hydride layer. *Journal of alloys and compounds*, 312(1-2):135–153, 2000.

[87] Ilya A Chernov, Joseph Bloch, and Igor E Gabis. Mathematical modelling of uh3 formation. *international journal of hydrogen energy*, 33(20): 5589–5595, 2008.

[88] Aram L Bugaev, Alexander A Guda, Kirill A Lomachenko, Vasiliy V Srabionyan, Lusegen A Bugaev, Alexander V Soldatov, Carlo Lamberti, Vladimir P Dmitriev, and Jeroen A van Bokhoven. Temperature- and pressure-dependent hydrogen concentration in supported pdh x nanoparticles by pd k-edge x-ray absorption spectroscopy. *The Journal of Physical Chemistry C*, 118(19):10416–10423, 2014.

[89] Bruce D Kay, Charles HF Peden, and D Wayne Goodman. Kinetics of hydrogen absorption by pd (110). *Physical Review B*, 34(2):817, 1986.

[90] SH Goods and SE Guthrie. Mechanical properties of palladium and palladium hydride. *Scripta Metallurgica;(United States)*, 26(4), 1992.

[91] John O Abe, API Popoola, Emmanueal Ajenifuja, and OM Popoola. Hydrogen energy, economy and storage: review and recommendation. *International journal of hydrogen energy*, 44(29):15072–15086, 2019.

[92] Ted B Flanagan and WA Oates. The palladium-hydrogen system. *Annual Review of Materials Science*, 21(1):269–304, 1991.

[93] Paolo Tripodi, Nicolas Armanet, Vincenzo Asarisi, Alessandro Avveduto, Alessandro Marmigi, Jean-Paul Biberian, and Jenny Darja Vinko. The effect of hydrogen stoichiometry on palladium strain and resistivity. *Physics Letters A*, 373(47):4301–4306, 2009.

[94] Toshiro Kuji, Yoshihito Matsumura, Hirohisa Uchida, and Tatsuhiko Aizawa. Hydrogen absorption of nanocrystalline palladium. *Journal of Alloys and Compounds*, 330:718–722, 2002.

[95] John R Lacher. A theoretical formula for the solubility of hydrogen in palladium. *Proceedings of the Royal Society of London. Series A-Mathematical and Physical Sciences*, 161(907):525–545, 1937.

[96] LK Heung, HT Sessions, X Xiao, and HL Mentzer. Demonstration of the next-generation TCAP hydrogen isotope separation process. *Fusion science and technology*, 56(4):1471–1475, 2009.

[97] R Lässer. Solubility of protium, deuterium, and tritium in the α phase of palladium. *Physical Review B*, 29(8):4765, 1984.

[98] S.S. Setayandeh, C.J. Webb, and E. MacA. Gray. Electron and phonon band structures of palladium and palladium hydride: A review. *Progress in Solid State Chemistry*, 60:100285, 2020. ISSN 0079-6786. doi: https://doi.org/10.1016/j.progsolidstchem.2020.100285. URL https://www.sciencedirect.com/science/article/pii/S0079678620300182.

[99] JE Klein and JR Wermer. Isotopic exchange for metal hydride bed disposal. *Fusion science and technology*, 41(3P2):776–781, 2002.

[100] Macarena Leal Olloqui. *A study of alteration processes in bentonite*. PhD thesis, University of Bristol, 2020.

[101] Crystal Lattices and Unit Cells, University of Arkansas at Little Rock, 3rd September 2021. URL https://chem.libretexts.org/Courses/University_of_Arkansas_Little_Rock/Chem_1403%3A_General_Chemistry_2/Text/12%3A_Solids/12.01%3A_Crystal_Lattices_and_Unit_Cells. [Online; accessed 2022-03-30].

[102] E Estevez-Rams, A Penton, J Martinez-Garcia, and H Fuess. The use of analytical peak profile functions to fit diffraction data of planar faulted layer crystals. *Crystal Research and Technology: Journal of Experimental and Industrial Crystallography*, 40(1-2):166–176, 2005.

[103] U. Hampel. 6 - x-ray computed tomography. In Mi Wang, editor, *Industrial Tomography*, Woodhead Publishing Series in Electronic and Optical Materials, pages 175–196. Woodhead Publishing, 2015. ISBN 978-1-78242-118-4. doi: https://doi.org/10.1016/B978-1-78242-118-4.00006-X.

[104] Zeiss. *ZEISS Xradia 520 Versa Submicron X-ray Imaging: Extending the Limits of Your Exploration*. Carl Zeiss Microscopy GmbH.

[105] Antonios Konstantinos Banos. *Investigation of uranium corrosion in mixed water-hydrogen environments*. PhD thesis, University of Bristol, 2017.

[106] Joseph Bloch. The hydriding kinetics of activated uranium powder under low (near equilibrium) hydrogen pressure. *Journal of Alloys and Compounds*, 361(1):130–137, 2003. ISSN 0925-8388. doi:

https://doi.org/10.1016/S0925-8388(03)00416-X. URL https://www.sciencedirect.com/science/article/pii/S092583880300416X.

[107] Francoise Caralp-Amilhat and Michel Destriau. Changes in the surface of uranium and its hydrides during successive hydrogenations and dehydrogenations at various temperatures. *Compt. Rend., Ser. C*, 271(21): 1265–1268, 1970.

[108] R. Rundle, N. Baenziger, A. Wilson, and R. McDonald. The Structures of the Carbides, Nitrides and Oxides of Uranium1. *Journal of the American Chemical Society*, 70(1):99–105, 1948.

[109] BR Butcher and AH Rowe. Phase transformation in uranium. *Nature*, 172(4383):817–817, 1953.

[110] A. Patterson. The Scherrer Formula for X-Ray Particle Size Determination. *Physical Review*, 56:978–982, November 1939. doi: 10.1103/PhysRev.56.978.

[111] Ahmad Monshi, Mohammad Reza Foroughi, and Mohammad Reza Monshi. Modified scherrer equation to estimate more accurately nano-crystallite size using xrd. *World J Nano Sci Eng, 2012, 2: 154*, 160, 2012.

[112] G. Williamson and W. Hall. X-ray Line Broadening from Filed Aluminium and Wolfram. *Acta metallurgica*, 1(1):22–31, 1953.

[113] Toshiaki Horiuchi and Naohiro Satoh. Relationship between duplex grain structure and grain boundary precipitates in n2m-stabilized alloy. *EJ. Adv. Maint*, 5:165–174, 2013.

[114] Jonathan C. Crowhurst, Alexander F. Goncharov, B. Sadigh, J.M. Zaug, D. Aberg, Yue Meng, and Vitali B. Prakapenka. Synthesis and characterization of nitrides of iridium and palladium. *Journal of Materials Research*, 23(1):1–5, 2008. doi: 10.1557/JMR.2008.0027.

[115] Franck Tessier and Roger Marchand. Ternary and higher order rare-earth nitride materials: synthesis and characterization of ionic-covalent oxynitride powders. *Journal of Solid State Chemistry*, 171(1-2):143–151, 2003.

[116] Walter Gordy and WJ Orville Thomas. Electronegativities of the elements. *The Journal of Chemical Physics*, 24(2):439–444, 1956.

[117] Mohammed SH Suleiman and Daniel P Joubert. Computational study of the structural, electronic and optical properties of bulk palladium nitrides. *arXiv preprint arXiv:1310.2751*, 2013.

[118] E Deligoz, K Colakoglu, and YO Ciftci. Electronic and mechanical properties of the pdn: A first-principles study. *physica status solidi (b)*, 247(9):2155–2160, 2010.

[119] Timothy J Prior and Peter D Battle. Facile synthesis of interstitial metal nitrides with the filled β-manganese structure. *Journal of Solid State Chemistry*, 172(1):138–147, 2003.

[120] T.C. Pluym, S.W. Lyons, Q.H. Powell, A.S. Gurav, T.T. Kodas, L.M. Wang, and H.D. Glicksman. Palladium metal and palladium oxide particle production by spray pyrolysis. *Materials Research Bulletin*, 28 (4):369–376, 1993. ISSN 0025-5408. doi: https://doi.org/10.1016/0025-5408(93)90070-T.

[121] E Rey, MR Kamal, RB Miles, and BSH Royce. The semiconductivity and stability of palladium oxide. *Journal of Materials Science*, 13(4):812–816, 1978.

[122] G Chaudron, A Portevin, and L Moreau. Cr hebd. séances acad. *Sci*, 207:235, 1938.

[123] FA Lewis. The hydrides of palladium and palladium alloys. *Platinum Metals Review*, 5(1):21–25, 1961.

[124] M Boudart and HS Hwang. Solubility of hydrogen in small particles of palladium. *Journal of catalysis*, 39(1):44–52, 1975.

[125] Grant S Henderson, Frank MF De Groot, and Benjamin JA Moulton. X-ray absorption near-edge structure (xanes) spectroscopy. *Reviews in Mineralogy and Geochemistry*, 78(1):75–138, 2014.

[126] Christoph Langhammer, Elin M Larsson, Bengt Kasemo, and Igor Zoric. Indirect nanoplasmonic sensing: ultrasensitive experimental platform for nanomaterials science and optical nanocalorimetry. *Nano letters*, 10(9):3529–3538, 2010.

[127] S Kishore, JA Nelson, JH Adair, and PC Eklund. Hydrogen storage in spherical and platelet palladium nanoparticles. *Journal of Alloys and Compounds*, 389(1-2):234–242, 2005.

[128] J. Klein. A Summary of Tritium in-bed Accountability for 1500 liter $LaNi_4$. 25al0. 75 storage beds. *Fusion science and technology*, 41(3P2): 542–550, 2002.

[129] M Bickel. The Davies-Gray Titration for the Assay of Uranium in Nuclear Materials: A Performance Study. *Journal of nuclear materials*, 246 (1):30–36, 1997.